

INFLUENCE OF THE SURFACE FILM STABILITY ON THE
CORROSION RESISTANCE OF Mg IN AQUEOUS SOLUTIONS

By

MEHDI TAHERI, B.Sc. M.Sc.

A Thesis

Submitted to the School of Graduate Studies

In Partial Fulfillment of the Requirements

For the Degree

Doctor of Philosophy

McMaster University

©Copyright by Mehdi Taheri, May 2013

MASTER OF APPLIED SCIENCE (2013)

McMaster University

Materials Science and Engineering

Hamilton, Ontario

TITLE: Influence of the Surface Film Stability on the Corrosion Resistance of Mg in Aqueous Solutions

AUTHOR: Mehdi Taheri B.Sc. (Isfahan University of Technology)

M.Sc. (Sharif University of Technology)

SUPERVISOR: Professor Joseph R. Kish

NUMBER OF PAGES: xiv, 152

ABSTRACT

This thesis presents an investigation into the structure and composition of the surface film formed on Mg in aqueous solutions and describes the influence of film stability on corrosion resistance. The composition and structure of the surface film formed on pure Mg in pure H₂O exposed at E_{corr} for 48 h was investigated using plan-view SEM-EDS imaging and STEM-EDS analysis of a FIB cross-section. The film formed was duplex in nature, consisting of a thinner, more-porous, nano-crystalline MgO-rich inner layer (50-100 nm), and a thicker, less-porous, Mg(OH)₂-rich outer platelet layer (700 nm). The results were consistent with the theory that a chemical breakdown (hydration) of the bulk inner MgO layer (native oxide) is a necessary precursor step to the corrosion process resulting in a significant thickening of the partially protective outer Mg(OH)₂ layer.

The surface film formed on pure Mg exposed in 0.01 M NaCl for 24 h at E_{corr} was found to be a diffuse bilayer structure similar to pure H₂O, including a thin and porous nano-crystalline MgO-rich inner layer (50-100 nm), and a thicker, more porous Mg(OH)₂-rich outer layer (300-600 nm). The un-pitted film region formed in 0.01 M NaCl solution at +0.1 V above E_b for 0.5 h after 24 h aging at E_{corr} exhibited a similar duplex structure. However, the thickness of both Mg(OH)₂-rich (~450 nm) and MgO-rich layers (~30-60 nm) appeared to be decreased. Furthermore, the pitted region film formed on an anodically polarized Mg sample exhibited thinner MgO-rich layer (~20-30 nm), decorated with macro-pores (~50 nm), and Mg(OH)₂ rich middle layer (~200-300 nm) buried under a thick, more porous needle-like Mg(OH)₂-rich top layer (~0.2-1 μm). EDS analysis confirmed the presence of Cl within the films formed in 0.01 M NaCl, and Fe containing particles within the pitted region anodic film. These results were consistent with an accelerated hydration of MgO to Mg(OH)₂ at lower pH and in presence of Cl⁻, formation of more soluble Mg-hydroxy-chlorides, enhanced Mg dissolution due to Cl⁻ ingress via increased film porosity, and influence of more noble impurities on the pit initiation and growth.

The ~50-150 nm film formed spontaneously on Mg exposed to 1 M NaOH was found to consist mainly of a crystalline MgO layer that has been hydrated to Mg(OH)₂ to a variable degree. Although the film exhibited excellent corrosion resistance, it was not stable. The film tended to experience an irregular breakdown/repair process, which was characterized by large irregular potential drops (about 1 V) under E_{corr} conditions. The breakdown/repair process is believed to involve the hydration-induced stress-rupture of the MgO film at discrete sites and the subsequent formation of a Mg(OH)₂ self-healing corrosion product nodule (~ 500 nm).

To understand the corrosion mechanisms and propose surface film evolution models, EIS behavior of Mg in all environments was investigated. The EIS spectra were compared with the proposed Nyquist behavior based on the film structure results. It was confirmed that the diffuse bilayer films formed in pure H₂O and 0.01 M NaCl possessed porosity, in which the electrolyte ingressed, forming the double layer and facilitating Mg faradic dissolution reaction across the Mg/film interface. Decreased porosity and R_{ct} along with the absence of a C_{film}/R_{por} loop, were respectively consistent with lower corrosion resistance of Mg in 0.01 M NaCl and a severely damaged pitted region film. Furthermore, the film compactness and increased R_{ct} in 1 M NaOH were consistent with a more stable film with excellent corrosion resistance in alkaline environments. In this film, liberated Mg²⁺ ions at the Mg/film interface have to diffuse through the film to facilitate the Mg(OH)₂ precipitation, thus a thicker Mg(OH)₂ film forms.

ACKNOWLEDGEMENTS

This thesis would not have been completed without substantial support from many individuals at McMaster University. First, I would like to sincerely thank my supervisor, Professor Joey Kish for giving me the opportunity to join his group and for providing me with the flexibility to pursue my own research goals. He has provided me with excellent guidance and educated me greatly to direct me in the right direction. I am grateful for the many opportunities he provided me with to present my work at international conferences and meet other researchers from all around the world. I would also like to thank my thesis committee members, Professor Joseph McDermid and Professor Gianluigi Botton, for their great comments and input about my research.

I would also like to express my gratitude to those that assisted me with many difficult experiments and analysis throughout my thesis. Julia Huang, Fred Pearson, Andreas Korinek, Dr. Glynis de Silveira, Chris Butcher, Steve Koprach, and Dr. Mohsen Danaie from the Canadian Centre for Electron Microscopy. In addition, Doug Culley, John Rodda, and Xiaogang Li generously offered their support to facilitate my work in the MSE Labs. I would also like to thank NSERC for their financial support and CANMET-MTL for providing the sample materials.

The Walter W. Smeltzer corrosion group and the Centre for Automotive Materials and Corrosion members also provided me with a lot of constructive criticism and helped me to improve my presentation skill. A special note of thanks is extended to my friends, specifically Stephen Jones and Ryan Phillips who helped me to shape this study with fruitful discussions, and Dr. Beth McNally for taking the time to read and edit the grammar of this thesis.

Finally, I would like to thank my family for their support throughout my life. Their encouragement was, in the end, what made this dissertation possible. Faezeh, Elham and my dear mother Azam receive my deepest gratitude for their understanding and love that made this whole endeavor much easier.

TABLE OF CONTENTS

Abstract	iii
Acknowledgements	v
Table of Contents	vi
List of Figures	viii
List of Tables	xiv
1. Introduction	1
1.1. Motivation.....	1
1.2. Statement of Problem and Thesis Contribution.....	1
1.3. Organization of Thesis.....	4
2. Literature review	5
2.1. Naturally Formed Magnesium Oxide Film.....	5
2.2. Magnesium Corrosion in Aqueous Environments.....	10
2.2.1. Passivation Stability	10
2.2.2. Surface Film Characterization.....	15
2.2.3. Film Breakdown	20
2.2.4. EIS Measurements.....	23
3. Research Objectives	27
4. Experimental Methods	29
4.1. Materials	29
4.2. Electrochemical Measurements	32
4.2.1. Cell Apparatus	32
4.2.2. Test Solutions	34
4.2.3. DC Measurements	35
4.2.4. AC Measurements	36
4.3. Magnesium Surface Film Analysis.....	37
4.3.1. SEM-EDS Analysis.....	38
4.3.2. FIB Sample Preparation	39
4.3.3. STEM-EDS Analysis	40
5. Film Structure Results.....	44
5.1. Mechanically Polished Mg	44
5.2. Pure H ₂ O.....	46

5.2.	0.01 M NaCl	55
5.2.1.	Film Formed at E_{corr}	58
5.2.2.	Anodic Film.....	68
5.3.	1 M NaOH	88
6.	Film Structure Models	100
6.1.	Pure H ₂ O.....	100
6.2.	Influence of Cl ⁻ and η_{anodic}	104
6.3.	Influence of pH.....	111
7.	Film Structure Validation by EIS	116
7.1.	Pure H ₂ O.....	116
7.2.	0.01 M NaCl vs. H ₂ O.....	120
7.3.	1 M NaOH vs. H ₂ O.....	128
8.	Conclusions.....	135
8.1.	Future Research Opportunities	137
8.	References.....	140

LIST OF FIGURES

Figure 2.1: TEM image, showing in cross-section, Mg surface film formed by exposure to an ambient atmosphere at 30 °C with 65 %RH after 96 h [24].	8
Figure 2.2: (a) Pourbaix diagram for the Mg in H ₂ O at 25°C with [Mg ²⁺] = 10 ⁻⁶ [30]; (b) Perrault diagram for stability of Mg in H ₂ O with hydrogen overpotential of 1 V [64].	12
Figure 2.3: Surface alkalization of Mg electrodes in 0.017 M NaCl electrolyte. The pH of fresh solution was 5.4-5.8 [70].	13
Figure 2.4: Proposed models to describe Mg NDE behaviour: (a) partially protective film [14], (b) Mg ⁺ formation-oxidation [71], [72], (c) MgH ₂ formation-decomposition [66], [71], (d) particle undermining [73], (e) Song et al.'s combined (a) and (b) theory [14], and (f) Bender et al.'s chemical equilibrium theory [74].	14
Figure 2.5: (a) TEM cross-section view of platelet-like structure formed on Mg in distilled water after 48h [24], (b) Direct carbon replica of the top surface of a film formed in pure water after 100 min and (c) 294 min on Mg in 10 ⁻⁴ M MgSO ₄ + KOH solution, pH 10.1. 9,000X [33].	17
Figure 2.6: Polarization curve of pure magnesium in 0.1 M NaCl. [91].	21
Figure 2.7: (a) Schematic representation of interface and equivalent circuit model based on Baril et al. [43], (b) Pebere et al. [45], (c) Song et al. [47] partial protective film, (d) Song et al. [48] recent porous film with different density, and (e) partial protective film EIS models for Mg corrosion in aqueous solutions [48].	24
Figure 4.1 Light optical microscopy image of Mg sheet microstructures (a) as-received (b) annealed L: longitudinal direction (rolling direction), T: transverse direction, S: short transverse direction).	31
Figure 4.2: Photograph of an as-prepared Mg working electrode used for the electrochemical measurements.	33
Figure 4.3: Photograph showing the experimental setup for electrochemical measurements.	34
Figure 4.4: Stages in STEM thin-foil preparation using FIB (a) milling trenches on both sides of the sample, (b) milled sample perimeter and welding of the probe to the specimen, (c) sample welding to a Cu grid and probe removal, and (d) two electron transparent windows milled on the sample.	40
Figure 4.5 STEM DF-image of the film/substrate interface after 48h in 1 M NaOH showing the O/Mg depth profile calculation procedure.	43
Figure 5.1: (a) SE-SEM and (b) BSE-SEM images of an embedded particle within the mechanically polished polycrystalline microstructure; (c) and (d) EDS spectra from the impurity particle and Mg matrix, respectively.	44

Figure 5.2: (a), (c), and (e) BSE-SEM image of some embedded impurity particle within the mechanically polished polycrystalline microstructure; (b), (d), and (f) EDS spectra from the impurity particle of (a), (c), and (e) images, respectively.	45
Figure 5.3: E_{corr} transient of 4N Mg exposed to pure H_2O for 48 h.....	47
Figure 5.4: (a) and (b) SE-SEM images of Mg sample surface aged 48 h in H_2O at different magnification showing platelets and cracking within the film.	48
Figure 5.5: TEM BF image showing, in cross-section, the surface film on the Mg sample formed by exposure to pure H_2O at E_{corr} for 48 h.	48
Figure 5.6: TEM BF image of the Mg/film interface, as formed after aging at E_{corr} in pure H_2O at room temperature for 48 h.	50
Figure 5.7: Diffraction pattern obtained from the Mg/film interface.	51
Figure 5.8: TEM dark-field image of the Mg/film interface region showing the extent of nano-crystalline region, as defined by the $\{200\}$ spacing in MgO.....	52
Figure 5.9: (a) STEM DF-image of the Mg/film interface, formed after aging at E_{corr} in pure H_2O at room temperature for 48 h, utilized to capture (b) a C EDS map, (c) a Mg EDS map and (d) an O EDS map.....	53
Figure 5.10: EDS sum spectrum of the SmartMap TM characteristic section analyzed in Figure 5.9.	54
Figure 5.11: Plot of the calculated atomic O/Mg ratio as a function of position across the interface between the surface film and the Mg substrate.....	54
Figure 5.12: E_{corr} transient of 4N Mg exposed to 0.01 M NaCl for 24 h.....	55
Figure 5.13: Potentiodynamic polarization curves of 4N Mg, after aging at E_{corr} for 24 h in 0.01 M NaCl solution.....	56
Figure 5.14: Potentiostatic diagram of Mg held 0.5 h at +0.1 V vs. E_b (1 V_{SCE}) after 24 h aging in 0.01 M NaCl.....	57
Figure 5.15: Characteristic surface appearance of 24 h aged Mg sample after 0.5 h potentiostatic exposure (a) in 0.01 M NaCl 0.1 V above E_b (b) Dried sample after the test.	58
Figure 5.16: SEM images of the film, in plan view, formed on Mg after exposure to 0.01 M NaCl for 24 h at E_{corr} , (a) low magnification, (b) and high magnification.....	58
Figure 5.17: (a) and (b) SEM images, and (c) and (d) EDS spectra of Mg surface aged for 24 h in 0.01 M NaCl showing the cracked platelet film.	59
Figure 5.18: (a) and (b) SEM images, and (c) and (d) EDS spectra of Mg surface aged for 24 h in 0.01 M NaCl showing a nodule residing on film.....	60
Figure 5.19: (a) and (b) SEM images, (c) and (d) EDS spectra of Mg surface aged for 24 h in 0.01 M NaCl showing Si containing embedded particles within the film.....	61

Figure 5.20: (a) and (b) SEM images, and (c) EDS spectrum from area selected for FIB milling of 24 h aged Mg sample in 0.01 M NaCl.	62
Figure 5.21: TEM BF-image showing, in cross-section, the film on the Mg sample formed by exposure to 0.01 M NaCl at E_{corr} for 24 h.	63
Figure 5.22: (a) and (b) STEM DF-images of Mg surface film formed after exposure to 0.01 M NaCl at E_{corr} for 24 h, (c) HR-TEM image of the film adjacent to the Mg/film interface.	64
Figure 5.23: (a) SAD pattern acquired from the film/substrate interface after exposure to 0.01 M NaCl at E_{corr} for 24 h; DF- TEM image of the film/substrate, as defined by the {200} and {220} reflections of the cubic MgO structure.	65
Figure 5.24: (a) STEM DF-image of the film formed on Mg exposed to 0.01 M NaCl after 24 h aging at E_{corr} , utilized to capture an (b) O EDS map, (c) Mg EDS map, (d) Cl EDS map and (e) W EDS map.	66
Figure 5.25: Sum spectrum of the SmartMap TM characteristic section analyzed in Figure 5.24.	67
Figure 5.26: O/Mg atomic ratio depth profile through the Mg/film interface, and the Mg substrate on Mg exposed to 0.01 M NaCl after 24 h aging at E_{corr}	68
Figure 5.27: SEM images of Mg sample surface aged 24 h in 0.01 M NaCl and potentiostatically polarized at +0.1 V vs. E_b for 0.5 h prior to FIB milling at different magnification (a) a pit (b), (c), and (d) higher magnification of the pit surface showing a film with more porosity.	69
Figure 5.28: (a) SE-SEM images (b), (c), and (d) EDS spectra of Mg sample surface aged 24 h in 0.01 M NaCl and potentiostatically polarized at +0.1 V vs. E_b for 0.5 h showing the presence of Cl and Fe adjacent to cracks inside the pit surface.	70
Figure 5.29: (a) SE, (b) BSE-SEM images and (c), (d), and (e) EDS spectra from adjacent to a local cracking inside a pit formed on the Mg sample surface aged 24 h in 0.01 M NaCl and potentiostatically polarized at +0.1 V vs. E_b for 0.5 h; white circles in (a) shows the particles containing Fe.	71
Figure 5.30: SE-SEM image of the selected area from Mg sample surface aged 24 h in 0.01 M NaCl and potentiostatically polarized 0.5 h at +0.1 V vs. E_b for FIB milling.	72
Figure 5.31: TEM bright-field image showing, in cross-section, the non-pitted region film formed on Mg exposed to 0.01 M NaCl at +0.1 V vs. E_b for 0.5 h after 24 h aging at E_{corr}	72
Figure 5.32: (a), (b) STEM DF-images of the non-pitted region formed on Mg exposed to 0.01 M NaCl at +0.1 V vs. E_b for 0.5 h after 24 h aging at E_{corr} , (c) HR-TEM image of Mg/film interface.	73
Figure 5.33: (a) SAD pattern acquired from the film/substrate interface formed on Mg exposed to 0.01 M NaCl at +0.1 V vs. E_b for 0.5 h after 24 h aging at E_{corr} ; DF-TEM	

image of the Mg/film, as defined by the {200} and {220} reflections of the cubic MgO structure.....	74
Figure 5.34: TEM BF-image showing, in cross-section, the pitted region formed on the Mg sample exposed to 0.01 M NaCl at +0.1 V vs. E_b for 0.5 h after 24 h aging at E_{corr} ...	75
Figure 5.35: (a), (b) STEM DF-images of the pitted region film formed on the Mg sample exposed to 0.01 M NaCl at +0.1 V vs. E_b for 0.5 h after 24 h aging at E_{corr} . (c) HR TEM image of the Mg/film interface, (d) HR TEM image of the middle-layer film. Circle in (b) shows a macro-pore.	76
Figure 5.36: (a) SAD pattern acquired from the Mg/film interface of pitted region film formed on Mg exposed to 0.01 M NaCl at +0.1 V vs. E_b for 0.5 h after 24 h aging at E_{corr} ; DF-TEM image of the Mg/film interface, as defined by the {200} and {220} reflections of the cubic MgO structure; (c) DF-TEM image of the top layer as defined by the {111} reflection of the hexagonal Mg(OH) ₂ structure acquired in the SAD pattern; (d) HR TEM image acquired from of a Mg(OH) ₂ needle in top layer.	77
Figure 5.37: (a) DF-STEM image of the non-pitted region film formed on Mg exposed 0.5 h to 0.01 M NaCl at +0.1 V vs. E_b after 24 h aging at E_{corr} , utilized to capture an (b) O EDS map, (c) Mg EDS map, (d) Cl EDS map and (e) W EDS map.	79
Figure 5.38: EDS sum spectrum of the SmartMap TM characteristic section analyzed in Figure 5.37.	80
Figure 5.39: O/Mg atomic ratio depth profile through the Mg/non-pitted region film interface formed on Mg after 0.5 h exposure in 0.01 M NaCl at +0.1 V vs. E_b	81
Figure 5.40: (a) DF-STEM image of the pitted region film formed on Mg after 0.5 h exposure in 0.01 M NaCl at +0.1 V vs. E_b , after 24 h aging at E_{corr} , utilized to capture (b) EDS spectra from the Fe containing particle found in Figure 5.30.	82
Figure 5.41: (a) STEM DF-image of the pitted region film containing Fe, formed on Mg exposed 0.5 h to 0.01 M NaCl at +0.1 V vs. E_b after 24 h aging at E_{corr} , utilized to capture an (b) O EDS map, (c) Mg EDS map, (d) Cl EDS map, (e) W EDS map and (e) Fe EDS map.....	84
Figure 5.42: EDS sum spectrum of the SmartMap TM characteristic section analyzed in Figure 5.41.	85
Figure 5.43: O/Mg atomic ratio depth profile through the Mg/pitted region film interface formed on Mg after 0.5 h exposure in 0.01 M NaCl at +0.1 V vs. E_b	86
Figure 5.44: Cl at. % depth profile through the interface region between the Mg/pitted region film interface formed on Mg after 0.5 h exposure in 0.01 M NaCl at +0.1 V vs. E_b	87
Figure 5.45: E_{corr} transients of 4N Mg exposed to 1 M NaOH for 48 h.	88
Figure 5.46: E_{corr} transients of 4N Mg, exposed to 0.1 M Na ₂ SO ₄ and 0.1 M Na ₂ SO ₄ + 1 M NaOH solution for 24 h.	89

Figure 5.47: Potentiodynamic polarization curve of 4N Mg, after aging 48 h at E_{corr} in 1 M NaOH.....	90
Figure 5.48: Potentiodynamic polarization curves of 4N Mg, after aging 24 h at E_{corr} in 1 M Na ₂ SO ₄ and 1 M Na ₂ SO ₄ + 1 M NaOH solution.	91
Figure 5.49: SEM images of the film, in plan view, formed on Mg after exposure to 1 M NaOH for 48 h, (a) low magnification (b) and high magnification.	92
Figure 5.50: BF-TEM image showing, in cross-section, the film on the Mg sample formed by exposure to 1 M NaOH at E_{corr} for 48 h.....	93
Figure 5.51: BF-TEM image of film/substrate interface (a) without nodule, and (b) with nodule present, and STEM DF-image of (c) the interface without nodule and (d) with nodule present on the film formed after exposure in 1 M NaOH for 48 h.....	94
Figure 5.52: SAD pattern acquired from the film/substrate interface directly underneath a nodule.....	95
Figure 5.53: DF-TEM image of the film/substrate interface underneath a nodule showing the extent of crystallinity, as defined by the {200} reflection of the cubic MgO structure.	96
Figure 5.54: (a) DF-STEM image of the Mg/film interface without nodule and the Mg substrate, formed after aging at E_{corr} in 1 M NaOH for 48 h, utilized to capture an (b) C EDS map, (c) O EDS map and (d) Mg EDS map.	97
Figure 5.55: (a) DF-STEM image of the Mg/film interface directly underneath a nodule and the Mg substrate, formed after aging at E_{corr} in 1 M NaOH for 48 h, utilized to capture an (b) C EDS map, (c) O EDS map and (d) Mg EDS map.	98
Figure 5.56: O/Mg atomic ratio depth profile through the Mg/film interface, with and without nodule formed after exposure to the 1 M NaOH solution for 48 h.....	99
Figure 6.1: Schematic of the diffuse bi-layer structure of the film formed on Mg after aging at E_{corr} in pure H ₂ O at room temperature for 48 h.....	100
Figure 6.2: Schematic of the film formed inside a pit after anodic polarization at +0.1 V vs. E_b for 0.5 h after aging at E_{corr} in 0.01 M NaCl for 24 h.	106
Figure 6.3: Schematic diagram showing the nature of the film on Mg formed after exposure in 1 M NaOH composed of a crystalline MgO-rich film and amorphous Mg(OH) ₂ -rich nodules on top of porous crystalline MgO film sections.	112
Figure 7.1: (a) Experimental Nyquist spectrum measured for Mg after 48 h aging in H ₂ O (b) Comparison of Kramer-Kronig transform with real and imaginary results.	117
Figure 7.2: Experimental Nyquist spectra for Mg (a) after 24 h aging in 0.01 M NaCl and, and (b) comparison of Kramer-Kronig transform with real and imaginary results.	121

Figure 7.3: Experimental Nyquist spectra for Mg (a) after 24 h aging in 0.01 M NaCl and 0.5 h potentiostatic exposure at +0.1 vs E_b , and (b) comparison of Kramer-Kronig transform with real and imaginary results. 122

Figure 7.4: Comparison of Nyquist spectra recorded in 0.01 M NaCl at E_{corr} after 24 h and 0.5 h at +0.1 vs E_b after 24 h aging versus pure H_2O 124

Figure 7.5: (a) Experimental Nyquist spectrum measured for Mg after 48 h aging in 1 M NaOH (b) Comparison of Kramer-Kronig transform with real and imaginary results.... 129

Figure 7.6: Comparison of Nyquist spectra recorded in 1 M NaOH versus pure H_2O after aging for 48 h at E_{corr} 130

Figure 7.7: Phase angle – frequency Bode diagram recorded for Mg after 48 h aging in 1 M NaOH. 131

LIST OF TABLES

Table 2.1: Summary of reported air-formed Mg surface film structure and composition reported in the literature.....	10
Table 2.2: Proposed physical equivalents for time constants observed in Mg EIS models.	25
Table 4.1: Chemical composition of wrought pure Mg sheet used to prepare test samples.	29
Table 4.2: Measured initial conductivity of test solutions.	35
Table 4.3: Sample preparation conditions for all surface films formed for surface analysis.	38
Table 5.1: Diffraction analysis data obtained from the Mg/film interface, as shown in Figure 5.7.	51
Table 5.2: Electrochemical kinetic parameters extracted from potentiodynamic polarization curves recorded for Mg in 0.01 M NaCl.....	56
Table 5.3: EDS elemental quantification of spectra recorded in Figure 5.40.	82
Table 5.4: Electrochemical kinetic parameters extracted from potentiodynamic polarization curves recorded for Mg in 1 M NaOH and 0.01 M Na ₂ SO ₄ solutions after 24 h aging.....	91
Table 6.1: Summary of Mg film composition and structure formed in 0.01 M NaCl.	105

1. INTRODUCTION

1.1. Motivation

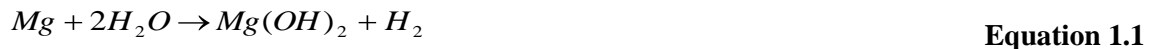
Reducing the vehicle weight is a practical approach to improve the fuel efficiency of automobiles. To accomplish this, Al alloys and polymers are being used, as well as advanced high strength steels, but Mg and its alloys can provide substantial additional reductions. Mg, with a specific weight of 1.7 g/cm^3 , is the lightest structural engineering material; 30% lighter than Al and 80% lighter than Fe. Mg and Mg alloys are currently used in some interior car parts such as instrument panels, beams, and brackets. The capability of being cast into thinner dimensions and more sophisticated shapes is another advantage of Mg over some Al and steel alloys for automotive applications. A major drawback limiting its wide usage in the automotive industry is the poor corrosion performance of Mg alloy components in aqueous environments, which is governed by the alloy composition, microstructure and the formation of a partially protective surface film corrosion product [1], [2], [3], [4]. Any attempt to improve the level of self-protection of Mg alloys requires knowledge of the composition, structure and protection properties of the surface film formed on unalloyed (commercially pure) Mg, and the manner in which the structure–property relations are modified through alloying [5], [6], [7], [8], [9], [10].

1.2. Statement of Problem and Thesis Contribution

According to the standard half-cell reduction potential table, Mg is the most active engineering metal ($E_{\text{Mg}/\text{Mg}^{2+}} = -2.37 \text{ V}_{\text{NHE}}$) [11], [12], [13], [14]. Nonetheless, Mg and Mg alloys have relatively good atmospheric corrosion resistance in dry environments [3], [15]. However, this atmospheric corrosion resistance deteriorates in increased humidity

and temperature, and in marine environments [10], [16], [17]. The protective behavior of Mg in the atmosphere correlates to the air-formed surface film, which is ascribed in the literature to either a single layer, comprised of a MgO/Mg(OH)₂ mixture [9], [10], [18], [19] or a MgO_x(OH)_y.nH₂O compound [20], or a bi-layer, comprised of an outer Mg(OH)₂-rich layer on top of an inner MgO-rich layer [21], [22], [23], [24]. This air-formed film is also reported to be covered with monolayers of MgCO₃ after exposure to ambient atmospheric conditions [9], [10], [21], [22], [23], [25].

Unfortunately, Mg exhibits poor corrosion resistance to exposure in aqueous solutions, particularly those containing aggressive anions such as Cl⁻ [2], [3], [4], [14], [15]. Mg dissolution in aqueous solutions generally proceeds by an overall electrochemical reaction, as shown by Equation 1.1, which precipitates Mg(OH)₂ on the surface with the simultaneous release of H₂ [2], [3], [4], [14], [15], [26], [27], [28], [29]. The outer Mg(OH)₂ corrosion product layer can form by either a dissolution-precipitation reaction (neutral solutions with pH < 11.4), or a solid state (direct) anodic reaction (alkaline solutions with pH > 11.4) according to the generalized Equation 1.2 + Equation 1.3 and Equation 1.4 respectively. At a pH greater than 11.4, Mg(OH)₂ is thermodynamically predicted to form a protective film; however, at a lower pH, this surface film is much less protective [2], [14], [30].



The stability of the surface film formed on Mg after exposure to H₂O [21], [23], [24], [31], [32], alkaline environments [33], [34], [35], [36], [37], and Cl⁻ containing solutions [21], [38], [39], [40], [41], [42] has received some attention. However, discrepancies regarding the number of layers present, role of carbonate, degree of crystallinity, and thickness have hindered the development of a more consistent surface film model in different aqueous environments. Furthermore, the Mg corrosion mechanism has been studied using EIS in SO₄²⁻ [43], [44], [45], [46] and Cl⁻ [46], [47], [48], [49], [50] containing solutions. Nevertheless, discrepancies exist in the equivalent circuit models used to verify the experimental results and the EIS analyses are not supported with the physical properties of Mg surface film. Therefore, the proposed mechanisms for corrosion processes of Mg in aqueous solutions are still lacking a detailed kinetic description, particularly concerning the breakdown and dissolution of the Mg surface film [43], [44], [45], [46], [47], [48], [51].

Consequently, this study was conducted to investigate the composition and structure of the surface film on Mg formed by exposure in near neutral, alkaline, and Cl⁻ containing aqueous solutions, using FIB/SEM and STEM-EDS methods. In addition, the kinetics of the corrosion processes were studied in the aforementioned environments using DC and AC electrochemical techniques. Eventually, using AC results combined with direct electron microscopy findings, Mg surface film formation and breakdown mechanisms in each environment are proposed.

1.3. Organization of Thesis

This thesis is composed of eight chapters. Chapter 1 summarizes the application of Mg and Mg alloys in automotive environments, as well as major obstacles for their wide usage from corrosion perspective. A brief review along with the overarching objective of this thesis, examining Mg corrosion in aqueous solutions, is also presented.

The literature concerning the known information regarding the surface film structure, composition and stability in atmospheric environments as well as aqueous solutions is described in Chapter 2. The surface film dependence on pH and aggressive ions of the substrate is briefly discussed in this chapter. Subsequently, questions arising from the literature questions and research objectives are presented in Chapter 3.

Detailed experimental methods and apparatus employed in this study are described in Chapter 4. Surface film structure and composition results obtained using FIB/SEM and STEM-EDS techniques as well as the electrochemical measurements are presented in Chapter 5. Afterwards, the structure and composition of Mg surface films formed in different solutions are discussed in Chapter 6. The mechanistic of corrosion processes were then evaluated and eventually the surface film formation and breakdown mechanism models are proposed. Chapter 7 summarizes the critical conclusions of the thesis and the future research opportunities are also described.

2. LITERATURE REVIEW

2.1. Naturally Formed Magnesium Oxide Film

Polycrystalline Mg is reported to obey a logarithmic oxidation growth mechanism at relatively low temperature (25 to $\sim 150^{\circ}\text{C}$) and O_2 partial pressures [52], [53], [54]. The oxide is proposed to nucleate at certain discrete surface sites, which subsequently create numerous oxide islands. The coalescence of these islands eventually produces a thin oxide layer 1.5-1.7 nm thick [52], [53]. This model is found to be consistent with the Mott-Cabrera mechanism such that the oxide growth at the Mg/film interface continues along with oxygen reduction on the film/atmosphere interface via electron tunneling [55], [56]. Overall, Mg oxidation is agreed to advance in three steps: (1) O_2 chemisorption and incorporation beneath outermost Mg layer and formation of islands; (2) lateral growth of islands and formation of monolayer of an oxide layer; (3) thickening of oxide.

XPS studies consistently show that the film formed on the surface of Mg after ambient atmospheric exposure is relatively thin and comprised of both MgO and $\text{Mg}(\text{OH})_2$ [6], [9], [10], [19], [20], [21], [22], [23], [24], [25], [31]. Fournier et al. [25] performed an XPS study on oxidation layers formed on polycrystalline Mg in pure O_2 atmosphere and Mg during wet H_2O grinding. It was deduced that the thin oxide layer formed by exposure to an O_2 atmosphere was primarily composed of MgO. Moreover, monolayers of MgCO_3 and $\text{Mg}(\text{OH})_2$ were detected on top of the MgO thin film. In addition, no metallic Mg BE-peak was acquired from the surface mechanically polished using H_2O . Therefore, a thicker oxide film including $\text{Mg}(\text{OH})_2$, MgO and MgCO_3 was reported to be produced.

Asami et al. [20] conducted an XPS study on Mg oxidation by exposing Mg scratched surfaces to an ambient atmosphere and identified the formation of an oxy-hydroxy Mg, $\text{MgO}_x(\text{OH})_y \cdot n\text{H}_2\text{O}$. The thickness of this oxy-hydroxy film and the intensity of hydroxide signal were reported to increase by increasing exposure time. In contrast, Splinter et al. [19] proposed a three step logarithmic oxidation mechanism for a clean Mg surface exposed to D_2O vapour, similar to that of O_2 atmosphere [52], [53], [54], based on XPS and AES measurements. It was also reported that the Mg surface film is primarily a defective thin film of crystalline MgO (c-MgO) formed by the interaction of dissociated H_2O molecules with Mg atoms. This MgO film was found to have short-range order due to the presence of trapped hydroxyl ions within the oxide crystals. Fuggle et al. [18] proposed similar mechanism for Mg surface film evolution in ambient atmospheres; however, the surface film was reported to be a mixture of $\text{MgO} + \text{Mg}(\text{OH})_2$. In another study, Feliu et al. reported a thin (< 3 nm) $\text{MgO} + \text{Mg}(\text{OH})_2$ film formed on the surface of as-received [9] and wet ground [10] Mg samples.

Liu et al. [23] carried out another XPS study on dry-ground Mg. A qualitative calculation of the XPS spectra on the unexposed sample suggested a 6 nm oxide film formed with a stoichiometry of $\text{Mg}_1\text{O}_{0.3}(\text{OH})_1$. This was hypothesized to be a bilayer structure of MgO and $\text{Mg}(\text{OH})_2$, in which $\text{Mg}(\text{OH})_2$ was grown on a MgO inner layer due oxide hydration with H_2O vapour. Also using XPS, Fotea et al. [22] investigated Mg surface film variation with exposure time to ambient atmosphere. It was reported that Mg surface film was a dual layer structure composed of an amorphous $\text{MgO} + \text{Mg}(\text{OH})_2$ inner

layer and a crystalline $Mg(OH)_2$ outer layer. The total thickness of the surface film was found to increase from 4 nm to 10 nm in 29 days.

These findings indicate that $Mg(OH)_2$ is the main component of the Mg air-formed surface film. This $Mg(OH)_2$ is expected to be formed by either a direct reaction of Mg with water vapor present in the atmosphere (Equation 2.1 and Equation 2.2) [6], [19] or chemical hydration of MgO (Equation 2.3) [57], [58], [59]. The direct reaction of Mg and H_2O (Equation 2.2) is likely to occur after partial dissociation of adsorbed H_2O molecules on the surface (Equation 2.1) [6], [19], [56], [60], [61]. In contrast, MgO hydration is proposed to proceed via a chemical reaction between the oxide and adsorbed H_2O [57], [58]. The degree of this hydration is reported to vary as a function of MgO roughness, density, crystallographic orientation, grain size, and number of bulk imperfections [57], [58], [60]. Hydration by adsorbed H_2O molecules is believed to account for the observed, albeit slow, thickening of the film through hydroxide formation with time [18], [21], [22].



Nordlien et al [24] conducted a TEM study on Mg cross-sectioned samples to evaluate the composition and structure of air-formed surface film. It was reported that Mg surface film formed by exposure to ambient atmosphere (at 30°C with 65 %RH for 96 h) exhibited a bi-layer structure of about 100-150 nm. The dual layer structure was composed of a hydrated oxide inner layer and a dense amorphous $MgO + Mg(OH)_2$ outer

layer (Figure 2.1). It was suggested that the dense, outer layer formed during initial oxidation by the Mott-Cabrera field-assisted cation transport mechanism [55] and was approximately 20-50 nm thick. The innermost layer was identified as a hydrated oxide, however, the oxide's sensitivity to the electron beam hindered an analysis of the composition and structure of this layer.

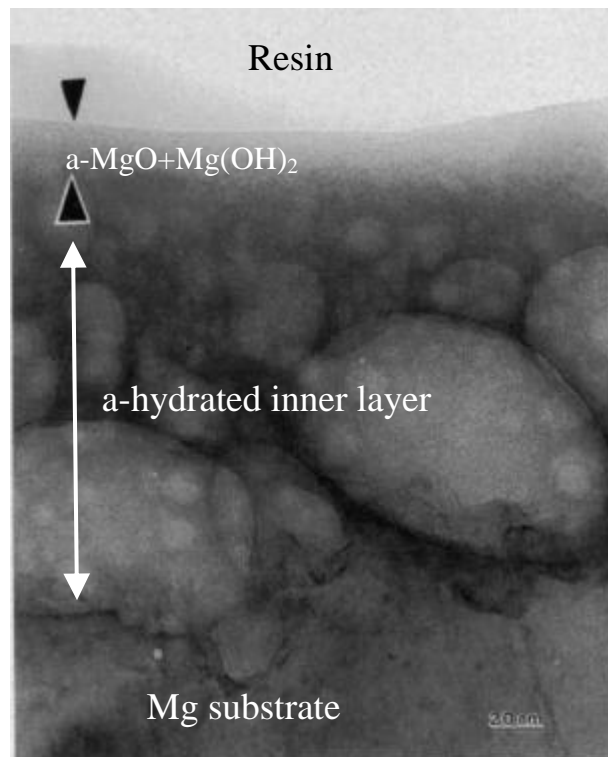


Figure 2.1: TEM image, showing in cross-section, Mg surface film formed by exposure to an ambient atmosphere at 30 °C with 65 %RH after 96 h [24].

Occasionally a carbonate (MgCO_3) peak also has been detected in the outer part of the surface film formed after ambient atmospheric exposure [9], [10], [21], [22], [23], [25]. It has been estimated to be only a monolayer thick when formed under such exposure [25]. This carbonate was attributed to incorporation of CO_2 , as CO_3^{2-} anions, within the corrosion film of Mg. Many carbonate products were identified in the Mg

surface film such as $3\text{MgCO}_3\cdot\text{Mg}(\text{OH})_2\cdot 3\text{H}_2\text{O}$, $5\text{MgCO}_3\cdot\text{Mg}(\text{OH})_2\cdot 9\text{H}_2\text{O}$, $\text{MgCO}_3\cdot 3\text{H}_2\text{O}$, and $\text{MgCO}_3\cdot 5\text{H}_2\text{O}$ [16], [17], [62]. Lindström et al. [56] investigated the atmospheric corrosion of Mg exposed to a relative humidity (RH) of 95%, at 22°C and as a function of CO_2 (0 or 350 ppm). Mg was reported to exhibit lower corrosion rates of nearly 4 times less in the absence of CO_2 , and the surface film exhibited a darker appearance along with a more porous structure with preferentially pitting attack. By contrast, a bright and shiny surface formed in the presence of CO_2 , which resulted into uniform corrosion. It was reported that Mg corrosion film primarily consisted of $\text{Mg}(\text{OH})_2$ in the absence of CO_2 , whereas a uniform layer of $\text{Mg}_5(\text{CO}_3)_4(\text{OH})_2\cdot 5\text{H}_2\text{O}$ was detected to have covered the Mg surface in the presence of CO_2 .

Overall, the structure of the air-formed Mg surface film has been discussed as a single layer, comprised of either a $\text{MgO}/\text{Mg}(\text{OH})_2$ mixture [9], [10], [18], [19] or a $\text{MgO}_x(\text{OH})_y\cdot n\text{H}_2\text{O}$ compound [20], or a bi-layer, comprised of an outer $\text{Mg}(\text{OH})_2$ -rich layer on top of an inner MgO-rich layer [21], [22], [23], [24]. Table 2.1 presents a summary of air-formed Mg surface film structures and compositions reported in the literature. Aside from discrepancies regarding the structure, composition, and crystallinity of the air-formed Mg surface film upon exposure in ambient atmosphere, there is also an apparent uncertainty concerning the film thickness between direct observation techniques and indirect surface analysis results. XPS studies consistently estimate the surface film to be less than 5 nm thick [6], [9], [10], [18], [19], [20], [21], [22], [23], [31], whereas the TEM study reported by Nordlien et al. showed the thickness of the surface film to be in the order of 25–50 nm [24].

Table 2.1: Summary of reported air-formed Mg surface film structure and composition reported in the literature.

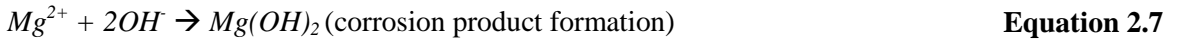
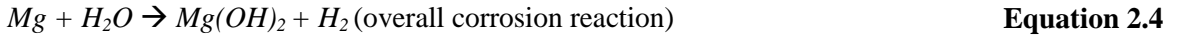
Layered Structure	Researcher	Surface Film and Preparation	Examination Technique Used	Reported Structure/Composition
Single-layer	Fuggle et al. (1975)	Mg thin-film aged in O ₂ and H ₂ O vapour	XPS	< 3 nm thick MgO/Mg(OH) ₂ mixture
	Splinter et al. (1993)	Ar ⁺ sputtered ground Mg; aged in D ₂ O vapour	XPS/AES	
	Feliu et al. (2009)	Wrought as-received Mg	XPS	
	Asami et al. (2000)	Clean Mg scratched; aged up to 1 month in lab air	XPS	4-10 nm thick MgO _x (OH) _y .nH ₂ O compound
Bi-layer	Yao et al. (2000)	As-received melt-spun Mg ribbons	XPS	2-5 nm thick outer Mg(OH) ₂ <hr/> < 3 nm thick inner MgO
	Fotea et al. (2006)	Air-aged evaporated Mg thin film	XPS	
	Santamaria et al. (2007)	Dry mechanically polished	XPS/PCS	
	Liu et al. (2009)	Wet ground Mg	XPS	
	Nordlien et al. (1997)	Ultramicrotomed Mg aged 96 h in 65%RH at 30°C	TEM/XPS	a-Mg(OH) ₂ +MgO <hr/> a-hydrated inner layer; nano-grains of c-MgO after e-irradiation

2.2. Magnesium Corrosion in Aqueous Environments

2.2.1. Passivation Stability

Figure 2.2a presents the Mg-H₂O potential-pH diagram established by Pourbaix [30]. This graph predicts that Mg passivity in aqueous solutions results from the formation of a Mg(OH)₂ surface film, which becomes stable in alkaline solutions (pH >

11.4) for an Mg^{2+} activity of 1×10^{-6} . The general corrosion reactions occurring in aqueous environments are reported to be as follow [2], [3], [4], [28], [63]:



The overall reaction (Equation 2.4) is found to be insensitive to oxygen concentration [3], [4], [14], [44].

Considering MgH_2 as a stable species, Perrault reconstructed the E-pH diagram of Mg for Mg- H_2O system (Figure 2.2) [64], [65]. Perrault concluded that in solutions with H^+ ions, H_2 molecules and a pH of greater than 5, MgH_2 exists in equilibrium with Mg^{2+} and $Mg(OH)_2$ only if H_2 evolution acquires overpotentials of about 1 V. Whereas for a pH lower than 5, neither the hydride nor hydroxide are stable and MgH_2 only interacts as an intermediate species between oxidation of Mg to Mg^{2+} (Equation 2.8-Equation 2.9).



Using ToF-SIMS depth profiles, Seyeux et al. [detected](#) small amount of MgH_2 in Mg surfaces film, formed during dry-polishing, and after aging in H_2O at E_{corr} for 120 s [32]. Depending on the location of MgH_2 within the surface film, the hydride forms on Mg via either a metallic cathodic reaction (Equation 2.8) at the substrate surface or a chemical reaction involving Mg^+ away from the substrate interface. MgH_2 is also reported presence on the Mg surface exposed in aqueous solutions in some other studies [66], [67].

Gulbrandson found MgH_2 on two sets of Mg electrodes one aged at E_{corr} and the other polarized at potentials below $-2.5 \text{ V}_{\text{SCE}}$ in $0.5 \text{ M NaHCO}_3 + 0.5 \text{ M Na}_2\text{CO}_3$, by means of X-ray diffraction [64]. In another study, Chen et al. reported MgH_2 formation within the surface film and Mg substrate after prolonged exposure in $0.1 \text{ M Na}_2\text{SO}_4$ at E_{corr} and after cathodic charging, by means of SIMS [68].

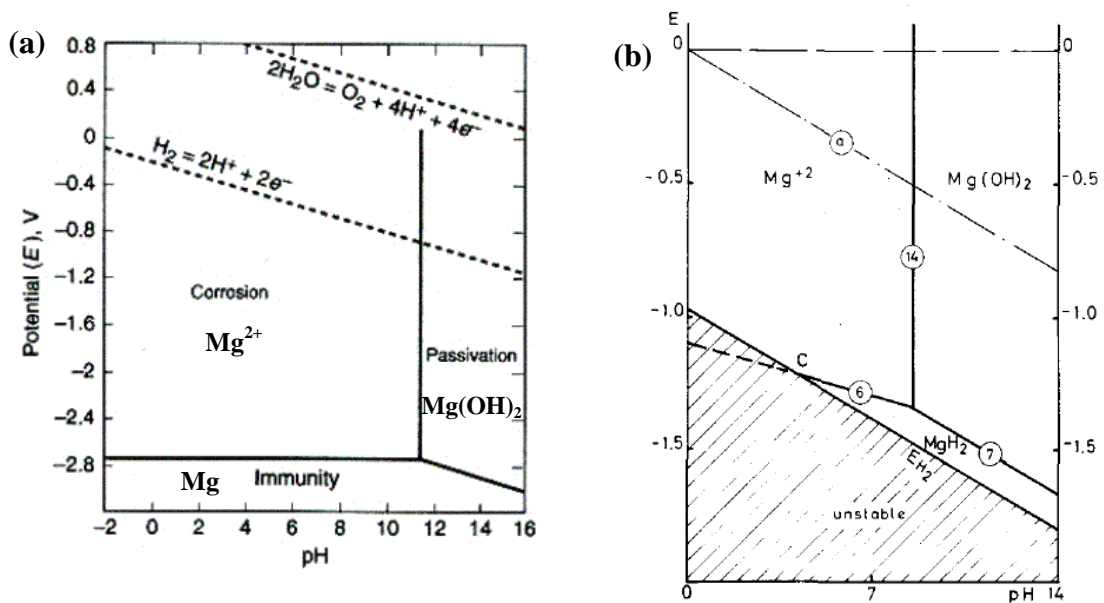


Figure 2.2: (a) Pourbaix diagram for the Mg in H_2O at 25°C with $[\text{Mg}^{2+}] = 10^{-6}$ [30]; (b) Perrault diagram for stability of Mg in H_2O with hydrogen overpotential of 1 V [64].

The given E-pH diagrams for Mg in H_2O , implies that the formation of a stabilizing outer $\text{Mg}(\text{OH})_2$ corrosion product layer can be achieved by either a dissolution-precipitation reaction in neutral solutions, or a solid state (direct) anodic reaction in alkaline solutions according to the generalized Equation 2.5 plus Equation 2.7 and Equation 2.10 respectively. Studies have confirmed this increased protective ability of the surface film formed on Mg in alkaline solutions [33], [34], [36], [66]. Mild anodic polarization of less than 2 V from E_{corr} in strong alkaline solutions ($\text{pH} \geq 12$) exhibits typical passive behavior, in which a low passive current density ($\sim 10^{-6} \text{ A/cm}^2$) is readily

established without an active-passive transition and independent of applied potential [34], [36], [37].

Mg is reported to undergo surface alkalization in near-neutral and low pH unbuffered aqueous solutions, as shown in Figure 2.3 [14], [43], [46], [69]. This is attributed to the increasing pH caused by OH^- via the H_2O reduction reaction (Equation 2.6). Inoue et al. [70] reported that this surface alkalization decreased the Mg corrosion rate after 4 h during long-term immersion in 0.017 M NaCl. However, in buffered solutions at pH 6.5 and 9 the Mg corrosion rate remained constant up to 100 h.

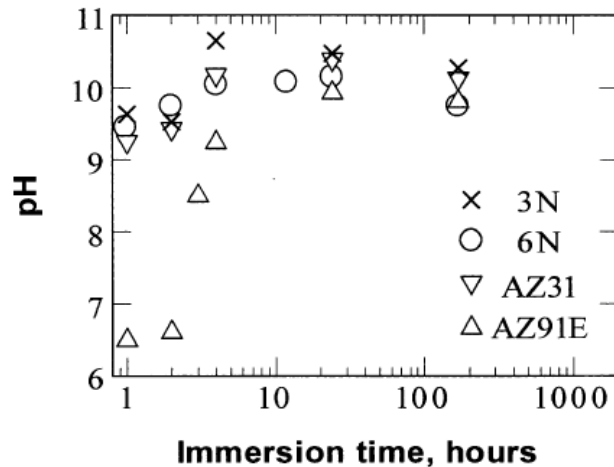


Figure 2.3: Surface alkalization of Mg electrodes in 0.017 M NaCl electrolyte. The pH of fresh solution was 5.4-5.8 [70].

The negative difference effect (NDE) is another unique Mg corrosion characteristic, which is ascribed to an enhanced H_2 evolution reaction with increasing anodic overpotentials [2], [3], [4], [14]. Several models such as a partially protective surface film [3], [14], Mg monovalent formation and oxidation [71], [72], undermining of impurity particles [72], and MgH_2 formation-decomposition [66], [71] have been

proposed to elucidate NDE. Figure 2.4a-d display the schematics of these four models respectively.

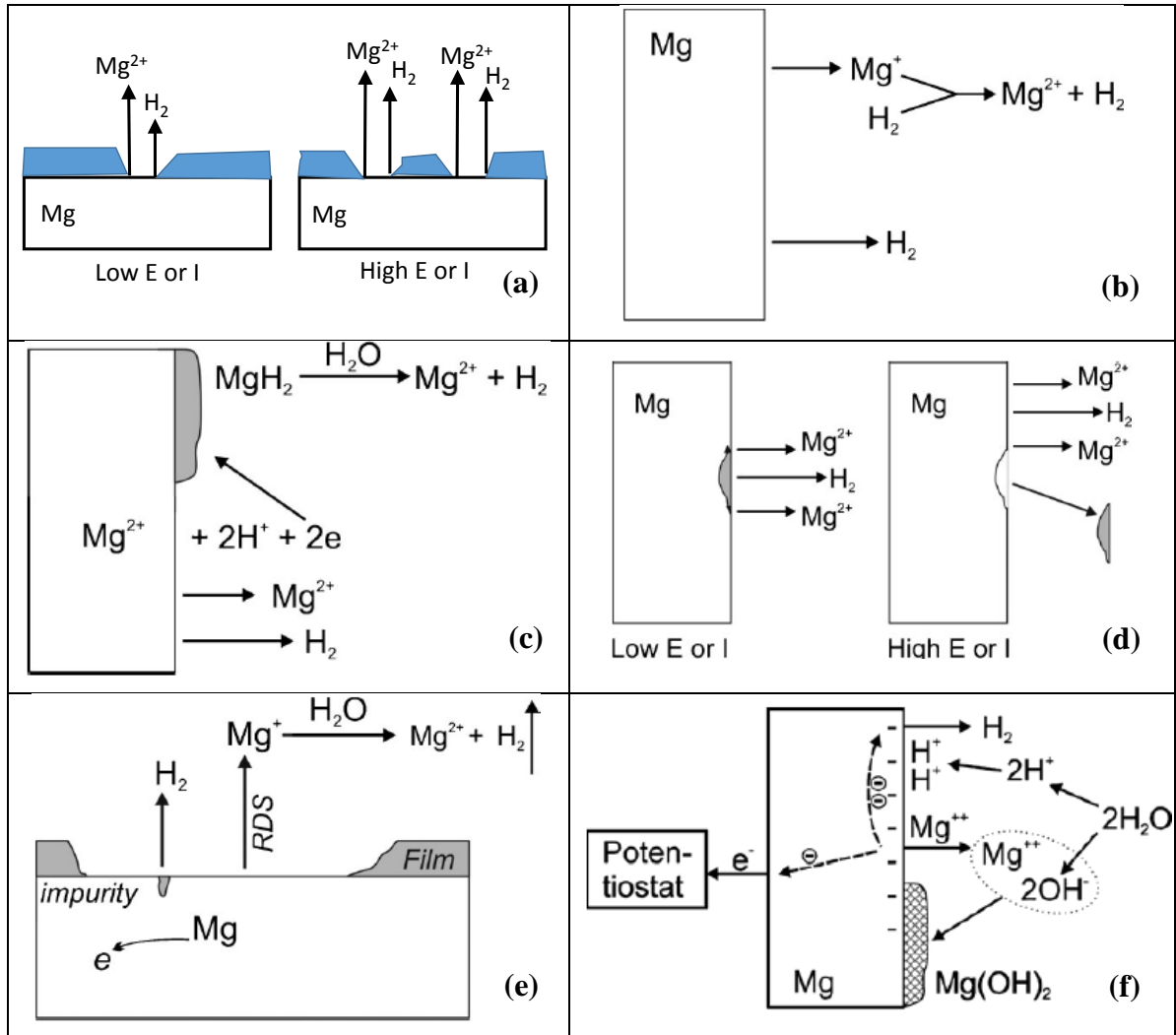


Figure 2.4: Proposed models to describe Mg NDE behaviour: (a) partially protective film [14], (b) Mg^+ formation-oxidation [71], [72], (c) MgH_2 formation-decomposition [66], [71], (d) particle undermining [73], (e) Song et al.'s combined (a) and (b) theory [14], and (f) Bender et al.'s chemical equilibrium theory [74].

Song et al. indicated that none of the above models can describe all aspects of NDE and introduced a new theory by combining partially protective film and Mg monovalent ion formation-oxidation models to rationalize all NDE characteristics, as shown in Figure 2.4e [14]. In this model, Mg anodic dissolution occurs via two

consecutive steps including with Mg^+ formation-oxidation (Equation 2.11 and Equation 2.12). This intermediate Mg^+ species undergoes another chemical reaction with H_2O that generates H_2 , as shown in Equation 2.13. At higher anodic overpotentials more Mg^+ is generated and hence Equation 2.13 intensifies in the forward direction. Song et al.'s NDE model was shown later to be consistent with Mg EIS analyses [43], [44], [48]; however, the hypothetical Mg monovalent ion has never been detected using analytical techniques [42], [75].



Consequently, Bender et al. [74], as shown in Figure 2.4f, proposed a new theory based on a chemical equilibrium of dissociated H_2O components across the electrode. According to Bender et al., the electrode surface undergoes hydroxyl depletion due to interaction of OH^- with generated Mg^{2+} to form corrosion products, as shown in Equation 2.7. Therefore, H_2 reduction accelerates in forward direction at film free areas, to compensate OH^- depletion. This increases the H_2 evolution rate and results in the NDE effect.

2.2.2. Surface Film Characterization

The stability of the surface film formed on Mg after exposure to H_2O for short times has received some attention. Yao et al. [21] found that the surface film on Mg, after aging in H_2O at E_{corr} for 60 s, remained mainly a mixture of $Mg(OH)_2$ and MgO , but was significantly thicker than that formed in laboratory air. Depth profiling revealed that the $Mg(OH)_2$ was predominant at the top layer and decreased gradually with depth, as the

MgO concentration increased. In contrast, Santamaria et al. [31] reported that the surface films formed during dry-polishing and after aging in H₂O at E_{corr} for 0–300 s maintained the original bi-layer structure, consisting of an ultra-thin MgO inner layer and a Mg(OH)₂ outer layer. A similar bi-layer structure was used to model the data collected from dry mechanically-polished Mg after aging in H₂O at E_{corr} for 0–420 s by Lui et al. [23]. In both of these studies, the Mg(OH)₂ outer layer was found to be the dominant component for exposure times greater than 30 s, and the composition and thickness of the inner MgO layer was found to remain unchanged. Using ToF-SIMS depth profiles, Seyeux et al. [32] reported that the surface films, formed during dry-polishing, and after aging in H₂O at E_{corr} for 120 s was a mixture comprised of Mg(OH)₂, predominantly in the outer layer, MgO, predominantly in the inner layer, and small amount of MgH₂ near the top surface. Again, a carbonate (MgCO₃) peak was also detected on occasion in the outer part of the surface film formed [23], [25], [31], [32].

In all of these studies, the structure of the surface film has been discussed in the absence of direct imaging of the surface film in cross-section. Nordlien et al. used TEM–EDS of ultramicrotomed cross sections, and XPS of limited plan view sections, to investigate the morphology, composition, and structure of the surface films formed on Mg by exposure to pure H₂O [24]. The surface film formed in H₂O at E_{corr} after 48 h was found to contain an additional top layer of crystalline MgO embedded in an amorphous Mg(OH)₂ matrix with an overall plate-like morphology, as shown in Figure 2.5a. The outer platelet-like layer had a thickness of 0.4–0.6 μm, consisted of a porous structure, and was reported to be aligned perpendicular to the surface. The perpendicular orientation

of the outer layer was used as evidence to support a dissolution-precipitation mechanism of $\text{Mg}(\text{OH})_2$. The observation of a surface film with a platelet-like morphology is consistent with that reported for Mg exposed in H_2O for 1.67 h by Vermilyea et al. [33] using plan view sections and electron microscopy (Figure 2.5b). However, Vermilyea and Kirk concluded that the platelets were crystalline $\text{Mg}(\text{OH})_2$ based on infrared spectroscopy experiments.

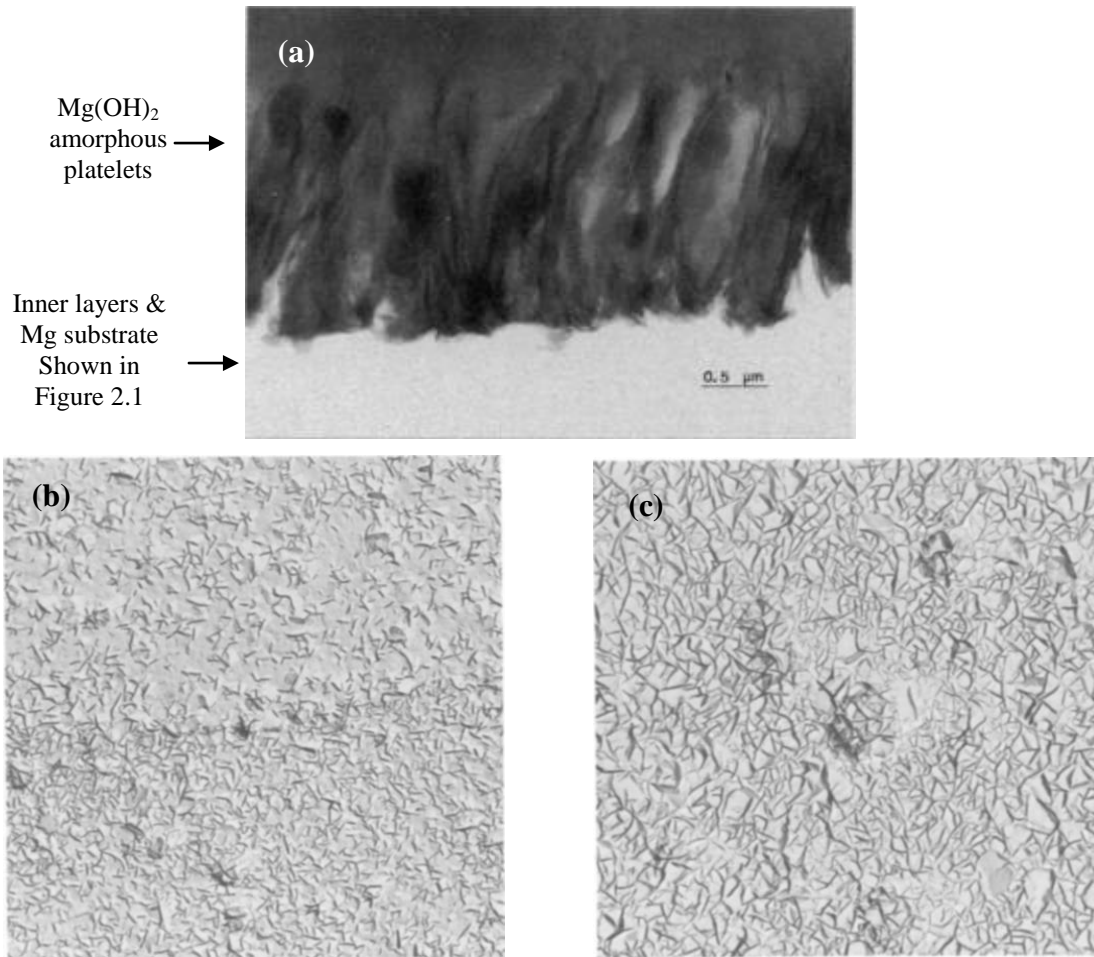


Figure 2.5: (a) TEM cross-section view of platelet-like structure formed on Mg in distilled water after 48h [24], (b) Direct carbon replica of the top surface of a film formed in pure water after 100 min and (c) 294 min on Mg in 10^{-4} M MgSO_4 + KOH solution, pH 10.1. 9,000X [33].

The nature of the surface film on Mg formed at E_{corr} in alkaline solutions has not been previously studied in much detail. Techniques utilized to characterize the nature of the surface films include electron microscopy coupled with infrared spectroscopy [33], electron microscopy coupled with X-ray diffraction [34], and ion beam analysis [35]. In each case, the surface film was characterized in plan view, rather than in cross-section. A comparison of the results show a general agreement on the chemical nature of the surface film that forms: namely the formation of $\text{Mg}(\text{OH})_2$. However, disagreement exists on the physical nature or structure of the film. Descriptions proposed include the formation of crystalline $\text{Mg}(\text{OH})_2$ platelets (Figure 2.5c) [33], a thick porous gel-like structure consisting of randomly stacked $\text{Mg}(\text{OH})_2$ platelets [34], and a permeable $\text{Mg}(\text{OH})_2$ layer [76]. Interestingly, the results of the surface analyses conducted did not verify whether the $\text{Mg}(\text{OH})_2$ film consists of an unspecified inner barrier layer, which the kinetic data implied should have been present [34], [76].

Comparison of the surface films formed in neutral and alkaline solutions at E_{corr} reveals that the film in both situations likely consists of a bi-layer structure, composed of a thick, less-protective $\text{Mg}(\text{OH})_2$ layer on top of a thin, more protective MgO layer. Therefore, the observed improved corrosion resistance of Mg in alkaline solutions may be attributed either to slower MgO hydration kinetics or a less permeable bi-layer surface film structure. The tendency for MgO powders [77], [78], [79] and MgO thin films [58], [80], [81] to undergo hydration reactions with liquid H_2O to form $\text{Mg}(\text{OH})_2$ has been studied in some detail. These studies consistently show that hydration is a surface reaction that involves the dissociation of absorbed H_2O molecules (Equation 2.1), followed by

MgO dissolution, then $\text{Mg}(\text{OH})_2$ precipitation (Equation 2.3). In alkaline solutions, Fruwirth et al. proposed that the dissolution of MgO occurs via OH^- attack at a MgOH^+ surface, which leads to the desorption of Mg^{2+} and OH^- ions into solution (Equation 2.14) [78].

Equation 2.14

Exceeding the solubility limit of Mg^{2+} in H_2O initiates the precipitation of a porous $\text{Mg}(\text{OH})_2$ surface layer (Equation 2.14). Kinetics show that the hydration is significantly slower in alkaline solutions [77], [78].

Equation 2.15

Also as mentioned earlier, the outer $\text{Mg}(\text{OH})_2$ corrosion product layer can form by either a dissolution-precipitation reaction in neutral solutions (Equation 2.5 + Equation 2.7), or a solid state, direct, anodic reaction in alkaline solutions (Equation 2.10). Recent studies on the precipitation of thin crystalline $\text{Mg}(\text{OH})_2$ films formed during potentiostatic cathodic polarization in aqueous $\text{Mg}(\text{NO}_3)_2$ solutions show that the $\text{Mg}(\text{OH})_2$ film structure depends on the applied potential, which affects the local pH of the solution adjacent to electrode [82], [83]. At low applied potentials, which cause mild local alkalization of the solution adjacent to the electrode, the precipitated film tends to exhibit a lamellar (platelet-shaped) porous structure. In contrast, at high applied potentials, with resulting strong local alkalization of the solution adjacent to the electrode, the precipitated film is likely to exhibit a dense, fine, flat particle structure. XRD and SEM studies show that the composition and structure of the anodic film formed during

the primary passive region at mild anodic polarization consists predominantly of dense crystalline $\text{Mg}(\text{OH})_2$ [84], [85].

2.2.3. Film Breakdown

Aggressive anions such as Cl^- , Br^- , SO_4^{2-} , and ClO_4^- are found to significantly increase Mg corrosion in aqueous solutions [4], [72]. This deleterious effect has been attributed to formation of soluble Mg salts within the corrosion film. These anions are reported to be transported to anodic sites on the Mg surface and form soluble Mg salts along with $\text{Mg}(\text{OH})_2$. Feitknecht et al. [86], [87] reported that Cl^- deforms the crystalline structure of $\text{Mg}(\text{OH})_2$, accordingly increases its solubility in aqueous environments. This Cl^- incorporation in $\text{Mg}(\text{OH})_2$ has been attributed to various Mg-Cl-OH complexes such as $\text{MgCl}_2 \cdot 6\text{H}_2\text{O}$ and $\text{Mg}_3(\text{OH})_5\text{Cl} \cdot 4\text{H}_2\text{O}$ [88], $5(\text{Mg}(\text{OH})_2) \cdot \text{MgCl}_2$ [41], and $\text{Mg}_6(\text{OH})_{10}\text{Cl}_2 \cdot \text{H}_2\text{O}$ [39], [40] using XRD, IR spectroscopy, and Auger electron spectroscopy (AES) respectively. Using electron probe microanalysis (EPMA) element mapping, Song et al. [48] also reported that Cl^- exhibited isolated concentration spots at the periphery of pitting areas on a Mg specimen immersed for 180 min in a 0.01 M NaCl solution. It was proposed that interior positions of the pit had lost Cl^- due to higher solubility of Mg chloride salts within the hydroxy-chloride product complexes and only less soluble $\text{Mg}(\text{OH})_2$ had remained. Moreover, Yao et al. [21] proposed that Cl^- increases the MgO hydration rate to $\text{Mg}(\text{OH})_2$.

The formation of these salts within the Mg surface film is reported to increase the acidity at the metal interface [39], [40], [41], [88]. It is agreed that this enhances the solubility of the Mg hydroxide film [51], makes the Mg surface film more active, and

increases the film free area [14], [39], [47]. Accordingly, the increased Mg film free surface area accelerates Mg dissolution when exposed to electrolyte [21], [39], [41], [46], [49], [63], [89], [90]. Interestingly, all halides except F^- are reported to deteriorate Mg corrosion resistance [2], [14], [89]. The distinct behaviour of F^- is ascribed to formation of less soluble MgF_2 salts within the Mg corrosion film, which enhances Mg corrosion resistance in aqueous and concentrated HF solutions [14].

Aggressive anions are also reported to encourage localized and pitting corrosion on Mg electrodes exposed to aqueous saline solutions [2], [3], [4], [14], [15]. The breakdown potential (E_b) is generally used to interpret pitting characteristics of Mg in saline solutions. Theoretically, E_b is a measure of surface film resistance to pit initiation and growth. The more noble the E_b , the more Mg would resist pitting corrosion [4]. E_b normally appears at tens of mV anodic overpotentials in Mg potentiodynamic polarization curves, when the current density abruptly increases, as shown in Figure 2.6. However, pitting corrosion rapidly turns into uniform corrosion when large concentrations of destructive ions exist in the environment [39], [42], [47], [51]

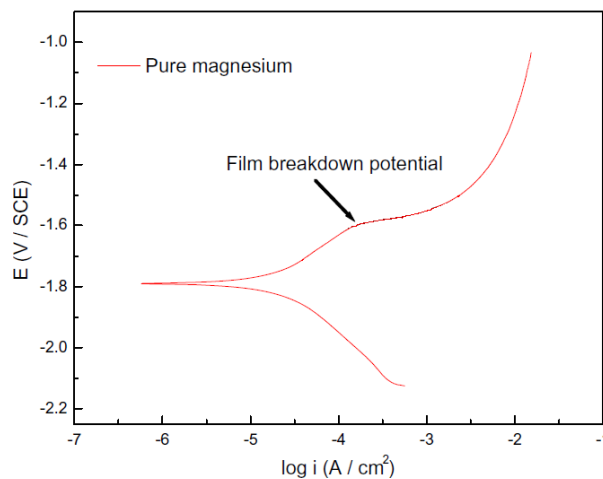


Figure 2.6: Polarization curve of pure magnesium in 0.1 M NaCl. [91].

However, it has been reported that Mg and many Mg alloys exhibit E_b lower than E_{corr} , which makes it difficult to measure the value of the breakdown potential [15]. Song et al. identified this E_b below E_{corr} behaviour for Mg specimens during cathodic polarization in 1 N NaCl and 1 N Na₂SO₄ at pH of 11 and 13 [46]. E_b is also reported to decrease by the addition of more aggressive ions, which implies less resistance of Mg to pitting corrosion [15], [89].

The proposed pit initiation and growth mechanisms for Mg are different than the classic autocatalytic pitting of stainless steels [14]. Mg pits are reported to initiate as dark points on the surface film, accompanied with H₂ evolution from the broken down areas; these pits are then reported to grow radially [51], [63], [92]. Williams et al. [51] investigated Mg pitting in 5 wt% NaCl solution using the scanning vibrating electrode technique (SVET) and observed cathodic current densities within the pit, whereas only anodic current densities were reported to exist at periphery of the pit. They attributed the cathodic behaviour of the interior blackened area of the pit to enrichment by nobler impurities such as Fe, also to an accelerated H₂ evolution reaction caused by roughened Mg surface, which liberates more OH⁻ into the solution and increases the pH locally. This increase along with presence of nobler enriched impurities was hypothesized to prevent vertical growth of pits and instead provokes radial progress.

Formation of localized pitting on Mg due to presence of nobler imperfections such as Fe and Si in matrix and particularly at grain boundaries is also reported by Lindström et al. [56], albeit in a CO₂-free NaCl-containing humid atmosphere. Fe and Si containing inclusions identified by SEM-EDS were hypothesized to induce the cathodic reaction

(Equation 2.6) and increase the pH locally at the areas adjacent to the impurities. This was postulated to encourage preferential Mg dissolution at areas away from the inclusions, particularly at grain boundaries. However, in the presence of carbon dioxide, absorbed CO₂ within the condensed electrolyte on the surface was proposed to interact with Mg anions and hydroxyl ions to form a dense hydroxy-carbonate product. This compact product is then hypothesized to reduce the rate of the cathodic and anodic processes due to lower conductivity and coverage of substrate, respectively [56].

2.2.4. EIS Measurements

EIS techniques not only provide the capability of running accurate measurements in low conductivity environments compared to DC methods, but also deliver mechanistic information regarding the corrosion kinetics of a system [12], [13], [93], [94]. However, interpretation of results is relatively more sophisticated, particularly when more than one time constant is recorded in the impedance diagram [95]. Study of Mg corrosion behaviour in aqueous solutions using EIS has received considerable attention. Schematics of the four main Mg corrosion EIS models proposed by Baril et al. [43], Pebere et al. [45], Song et al. (1997) [47], and Song et al. (2012) [48] are shown in Figure 2.7a-e. The EIS equivalent circuit elements along with their corresponding physical structure for each model are summarized in Table 2.2.

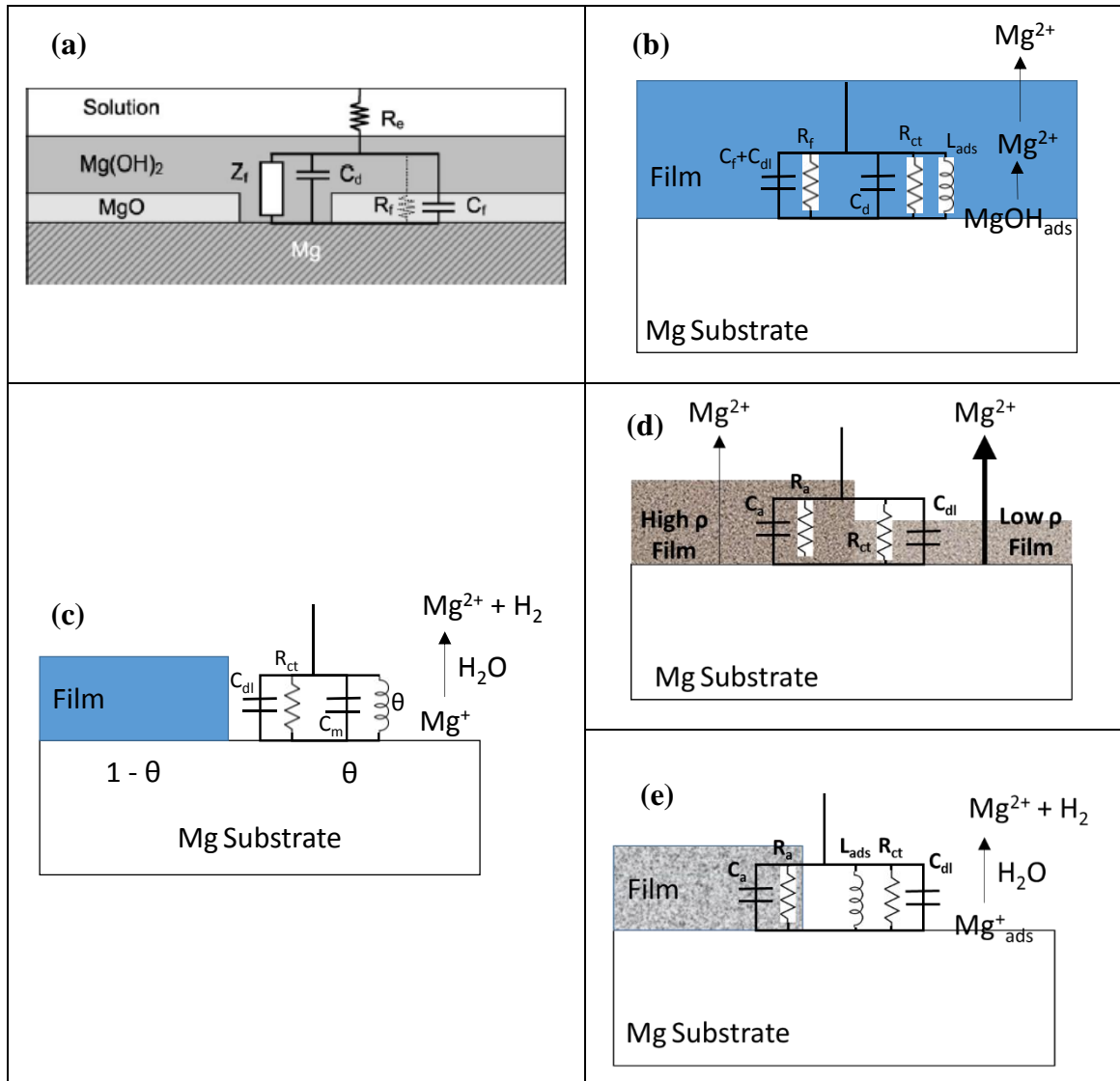


Figure 2.7: (a) Schematic representation of interface and equivalent circuit model based on Baril et al. [43], (b) Pebere et al. [45], (c) Song et al. [47] partial protective film, (d) Song et al. [48] recent porous film with different density, and (e) partial protective film EIS models for Mg corrosion in aqueous solutions [48].

Using EIS and scanning electrochemical microscopy (SECM) results obtained on Mg exposed at E_{corr} in dilute Na_2SO_4 solutions at pH 5.6, Baril et al. [43] proposed a model to describe Mg corrosion mechanisms in saline solutions, as shown in Figure 2.7a. They reported that Mg EIS behaviour (normalized to the maximum value of real

impedance) varies with the change in the MgO film-free surface area. The Mg surface film is hypothesized to be bilayer, composed of a thin, dense MgO barrier layer and a thick, relatively porous Mg(OH)₂ outer layer. Therefore, the high and medium capacitive loops observed in Nyquist diagrams are attributed to MgO layer capacitance-resistance ($C_f || R_f$) and double layer capacitance-faradic impedance ($C_{dl} || Z_f$), respectively (Table 2.2). The low frequency inductive loop (Z_f) is also ascribed to relaxation process of absorbed Mg⁺ intermediate species (Equation 2.11-Equation 2.13). In contrast, Pebere et al. [45] correlates both the single layer film and faradic impedance behaviour to high frequency capacitive arc, whereas the second loop is attributed to relaxation of mass transport within the single layer film (C_d). The inductive loop is also ascribed to the relaxation of an adsorbed intermediate species (L_{ads}), likely MgOH_{ads} (Figure 2.7b).

Table 2.2: Proposed physical equivalents for time constants observed in Mg EIS models.

	High frequency capacitive loop	Medium frequency capacitive loop	Low frequency inductive loop
Baril et al. [43]	$C_f R_f$	$C_{dl} R_{ct}$	$L_{Mg^{+ads}}$
Pebere et al. [45]	$C_f + C_{dl} R_f$	Relaxation of mass transport through film	$L_{MgOHads}$
Song et al. (1997) [47]	$C_{dl} R_{ct}$	Relaxation of C_m	Relaxation of θ
Song et al. (2010) [48]	$C_{dl} R_{ct}$	$C_a R_a$ (film formation & dissolution)	$L_{Mg^{+ads}}$

Song et al. [47] developed an EIS model based on their Mg⁺ and partially protective surface film NDE theory (Figure 2.4e). The hypothesis of a Mg partially protective surface film is consistent with the Mg/MgO Pilling-Bedworth ratio. The Pilling-Bedworth ratio of Mg/MgO is nearly 0.81, which suggests a broken oxide without protective ability [11], [13], [96]. However, Mg/Mg(OH)₂ has a Pilling-Bedworth ratio of

1.77 that ascribes to a resistant surface film [4]. Assuming that the ratio of film free area (θ) and Mg^+ concentration (C_m) are the main faradic AC current variables, Song et al. developed their EIS model for Mg corrosion in 1 N NaCl using Cao et al.'s [97], [98] steady-state admittance equations for irreversible electrode. They attributed the high frequency capacitive loop to the double layer capacitance-charge transfer resistance ($C_{dl}||R_{ct}$), the medium frequency capacitive loop to C_m within the film free areas, and correlated the low frequency inductive loop to θ variable, as shown in Figure 2.7c [47].

More recently, Song et al. [48] modified Baril et al.'s [43] EIS model by considering variations in film porosity and corrosion rate of different areas on Mg, as shown in Figure 2.7d and Figure 2.7e. It was proposed that a slight deviation from uniform corrosion is likely to result in different corrosion rates in adjacent areas (Figure 2.7d), in which the more corrosion resistant zone exhibits a denser and more protective film. They attributed the high frequency loop to $C_{dl}||R_{ct}$ at the Mg/film interface. The pseudo capacitance, C_a , and pseudo resistance, R_a , were also ascribed to the lower frequency loop. No physical meaning was reported for C_a and R_a elements, and the frequency loop was only correlated to the film formation and breakdown (Table 2.2). In the case of a substantial deviation from the uniform corrosion, the film on less corrosion resistant was reported to be removed. Therefore, dissolution of Mg was proposed to accelerate inside the pit (Figure 2.7e). Song et al. [48] reported that an inductive loop replaces the second capacitive loop after the film had broken down. The inductance was ascribed to Mg^+ intermediate species as described by Baril et al [43].

3. RESEARCH OBJECTIVES

In order to achieve the goal of Mg automotive components, its poor corrosion resistance in aqueous solutions must be adequately addressed. This requires a comprehensive knowledge of Mg surface film structure and composition, and how this controls the corrosion kinetics. Accordingly, characterizing the corrosion resistance of Mg is an essential first step to better understanding the corrosion resistance of Mg alloys.

It is clear from the literature review that the structure and composition of Mg surface film is not yet well-understood. Furthermore, the mechanism by which the film controls corrosion is also not well understood. Consequently, this study was undertaken to help to characterize the surface film and formulate a mechanism that describes how the film controls corrosion. Thus, the proposed research has the following objectives:

- Investigate the structure and composition of the surface film formed on mechanically polished pure Mg aged in H₂O at E_{corr} for 48 h by direct imaging of FIB-prepared cross-sections using STEM and EDS.
- Study the nature of the surface film formed on mechanically polished pure Mg aged in 0.01 M NaCl at E_{corr} for 24 h by direct imaging of FIB-prepared cross-sections using STEM and EDS. The NaCl solution was used to discover the deleterious effect of Cl⁻ on the corrosion rate of Mg.
- Investigate the structure and composition of the surface film formed on mechanically polished pure Mg aged in 0.01 M NaCl at E_{corr} for 24 h, followed by a potentiostatic exposure 100 mV above E_b for 0.5 h, using

scanning TEM (STEM) and EDS. Potentiostatic anodic exposure was conducted to elucidate the nature of the broken down film.

- Examine the structure and composition of the surface film formed on mechanically polished pure Mg aged in 1 M NaOH at E_{corr} for 48 h by imaging of FIB-prepared cross-sections using STEM and EDS. The alkaline solution is selected to relate the structural features of the grown layers in 1 M NaOH (pH 14) to the greatly enhanced corrosion resistance of Mg compared to near-neutral environments.
- Investigate the AC electrochemical behavior of Mg corrosion in all the above environments, along with E_{corr} transients and DC potentiodynamic polarization measurements, to understand the corrosion mechanisms.
- Compare the EIS results with the direct imaging findings to propose Mg corrosion mechanisms and surface film evolution models in all the aforementioned environments.

4. EXPERIMENTAL METHODS

4.1. Materials

All test samples used in this study were prepared from 2 mm thick cold drawn polycrystalline Mg sheet of 99.99 wt% nominal purity provided by Natural Resources Canada (CanmetMATERIALS). The impurity level and tolerance limit for each element is shown in Table 4.1. The measured concentrations of Fe, Ni, and Cu, as critical impurities, were below the tolerance limit.

Table 4.1: Chemical composition of wrought pure Mg sheet used to prepare test samples.

Element	Al	Ca	Ce	Cu	Fe	Mn	Ni	Si	Zn	Zr	Mg
Concentration, ppm	9	29	37	32	50	22	9	2	636	31	balance
Tolerance Limit, ppm [14]	2e6	3e5	N/A	1000	150	N/A	10	N/A	2e6	N/A	N/A

Rectangular samples (10 mm × 10 mm) were cut from the 2 mm thick Mg sheet using a band saw. In order to homogenize the grain structure and minimize the effect of mechanical surface twinning, samples were annealed for 0.5 h at 350°C in an ambient atmosphere and then quenched in H₂O.

Two sets of as-received and annealed samples were cold mounted with the METLABTM epoxy mounting system. Samples were placed in the cold mount moulds, and were taken out of the moulds 8 h after the epoxy was added. The cold mounted samples were then transferred to an automatic polisher (RotoPol-31 Automatic Polisher). Automated polishing was necessary to obtain high quality surfaces with minimal surface metallographic defects such as grinding scratches and surface twinning. Samples were mechanically ground using 1200, 2400 and 4000, EU p-grade, grit silicon carbide (SiC)

grinding papers and anhydrous ethanol (C_2H_6O) as the lubricant. Afterwards, the specimens were progressively auto-polished using 9 μm , 3 μm and 1 μm H_2O -free diamond suspensions on NAP cloths with a 80% ethylene glycol ($C_2H_6O_2$) solution and 20% glycerin ($C_3H_8O_3$) as the lubricant. Samples then underwent a final auto-polishing stage with 0.05 μm colloidal silica (SiO_2) (OP-S) on MD-Chem cloth. After each step, samples were cleaned with anhydrous C_2H_6O and dried in a warm stream of air.

An acetic-picral ($C_2H_4O_2$ - $C_6H_3N_3O_7$) etchant in accordance with ASTM E407 - 07 [99] was used to etch the samples after the polishing. Samples were exposed to the etchant for about 5 s and then rinsed with anhydrous C_2H_6O and dried with a stream of hot air. The light optical microscopy images of the Mg sheet microstructure are shown in Figure 4.1. The as-received microstructure is displayed in Figure 4.1a, whereas Figure 4.1b shows the annealed microstructure. The annealed microstructure is composed of recrystallized grains with a high density of mechanical twins, which made it difficult to conduct an average grain size measurement in accordance with ASTM E112 - 96 standard. The mechanical twinings are usually formed due to mechanical stresses caused by cold drawing stage; however, they are reported to be created during cutting, grinding, and even handling if the pressures are extreme [100].

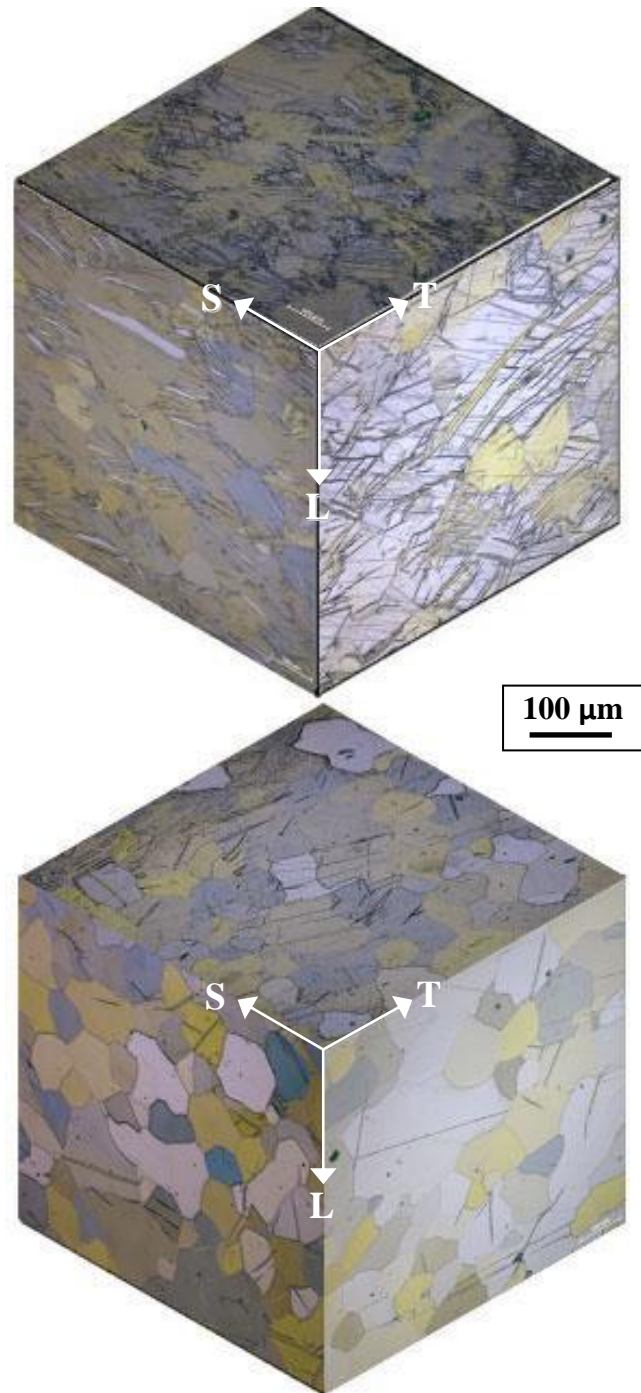


Figure 4.1 Light optical microscopy image of Mg sheet microstructures (a) as-received (b) annealed L: longitudinal direction (rolling direction), T: transverse direction, S: short transverse direction).

Subsequently, the samples were examined with an optical light microscope (Nikon LV100 Eclipse) at various magnifications. An image analysis software (Clemex

Vision Professional Edition) coupled with an optical microscope (Leica DM1 5000) was utilised to measure the average grain size and distribution in accordance with ASTM E112 - 12 method (Standard Test Methods for Determining Average Grain Size) [101]. The average grain size of 89.6 μm was calculated as ASTM grain size number of 4.

4.2. Electrochemical Measurements

4.2.1. Cell Apparatus

The rectangular working Mg electrodes were cut from the sheet stock. The cut electrodes were annealed at 350°C for 0.5 h in an ambient atmosphere and then quenched in H₂O. Prior to cold mounting, a stripped end of a Cu wire was taped to the buried surface of the electrode with a conductive Al tape. The electrical conductivity of the exposed side of the sample to the other end of the electric Cu wire connection was measured using a voltmeter. The electrodes were then cold mounted in an METLABTM epoxy resin, using standard laboratory metallographic procedures to expose one of the 1 cm² surfaces. In order to isolate the Cu wire from exposure to the test solution, a plastic straw tube was placed around the Cu wire and glued to the cold mount. This also provided some rigidity to the cold mounted working electrode.

Figure 4.2 shows a working electrode prepared as described above. All working electrodes prepared in this manner were mechanically ground with SiC grinding papers up to a 4000 grit using anhydrous C_2H_6O as lubricant, then rinsed and dried with a warm stream of air.

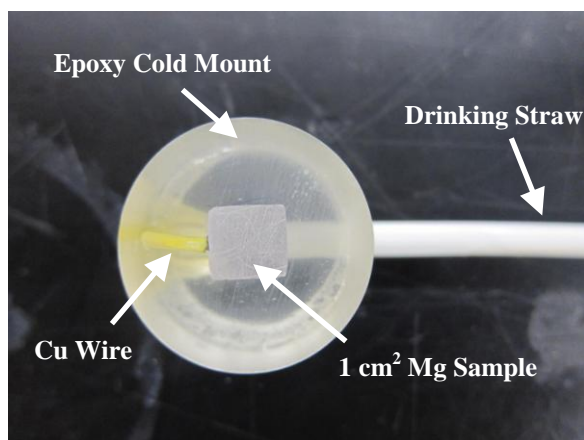


Figure 4.2: Photograph of an as-prepared Mg working electrode used for the electrochemical measurements.

A 1000 mL K0047 PARTM corrosion cell kit was utilized to conduct all electrochemical measurements. A saturated calomel electrode (SCE) coupled with a salt bridge tube filled with saturated KCl solution was used as the reference electrode. A graphite rod fixed within a round glass joint within the cell was used as the counter electrode. The working electrodes were suspended in the corrosion cell from an external to cell clamp holding the plastic straw tube during the measurements. Figure 4.3 shows the experimental setup of the corrosion cell with all compartments.

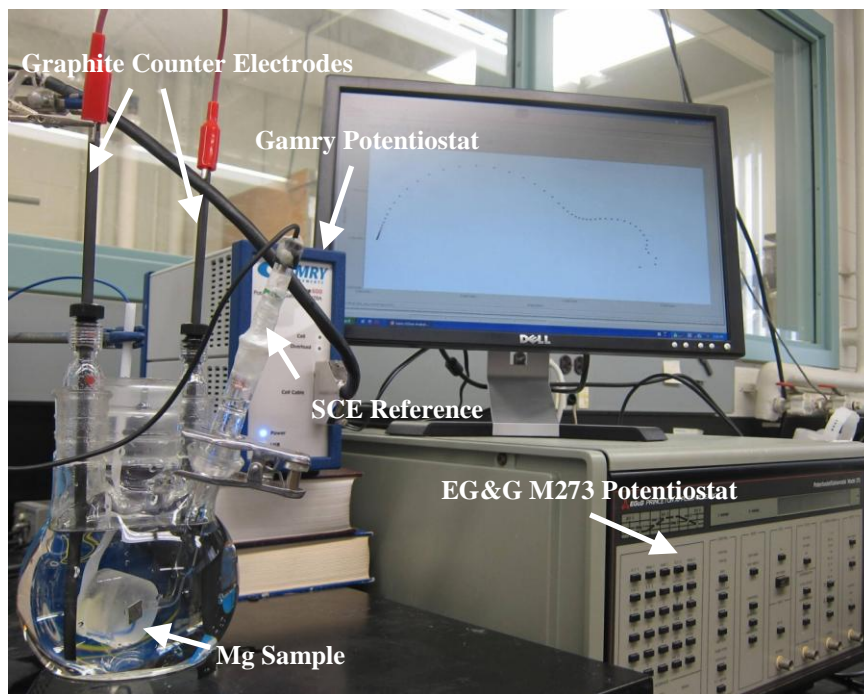


Figure 4.3: Photograph showing the experimental setup for electrochemical measurements.

4.2.2. Test Solutions

Test electrolyte solutions were prepared using ultrapure water (HPLC H₂O), deionized water (DI H₂O), and reagent grade NaCl, Na₂SO₄, NaOH, and Mg(OH)₂ chemicals. To prepare a 1 M NaOH solution with a pH of 14, 40 g of reagent grade NaOH was added to 1000 mL DI H₂O. Additionally, a 0.01 M NaCl solution was produced by mixing 5.842 g of NaCl with 1000 mL DI H₂O. A dilute 0.01 M NaCl solution was selected as a mildly aggressive solution, in which to study the corrosion behaviour, while, DI H₂O represented a non-stable passive film, and the NaOH solution produced stable passivity.

A magnetic stirrer was used to mix the solutions prior to placement in the cell. The pH of the solutions at laboratory temperature was measured with an Accumet™ pH meter. The conductivity of the solutions at room temperature was measured using a

LabtronicsTM conductivity meter. The results of solution conductivities are listed in Table 4.2.

Table 4.2: Measured initial conductivity of test solutions.

Solution	HPLC H ₂ O	DI H ₂ O	0.01 M NaCl	1 M NaOH
Conductivity, $\mu\text{S/cm}$	1.5	6.52	635	20000

4.2.3. DC Measurements

E_{corr} measurements were made before other electrochemical tests such as potentiodynamic polarization and EIS, as well as for samples prepared for surface analysis. Based on the stability required prior to each DC and AC electrochemical measurement, the E_{corr} was measured for 24 h or 48 h. The experiments were conducted using either an EG&G Model 273TM or Gamry Reference 600TM potentiostat. The testing electrolytes were open to laboratory atmosphere during measurements and the half cell potential of the SCE was corrected compared to a master reference electrode prior to each experiment.

All potentiodynamic polarization experiments were carried out after E_{corr} was stabilized. Potentiodynamic polarization measurements were recorded in different solutions including 1 M NaOH, and 0.01 M NaCl using either an EG&G Model 273TM or Gamry Reference 600TM potentiostat. The potential was swept from -0.25 V vs. E_{corr} to 1 V vs. E_{corr} with a scan rate of 1 mV/s in each measurement.

Subsequently, the potentiodynamic curves were analysed using the PowersuiteTM (EG&G 273TM potentiostat) or Gamry Electrochem AnalystTM (Gamry Reference 600TM potentiostat) software package. Values of the corrosion current densities (i_{corr}) in 0.01 M

NaCl were obtained using the cathodic Tafel extrapolation technique [102], whereas in 1 M NaOH, the anodic limiting current density was used to calculate as i_{corr} . Other corrosion kinetics parameters such as E_{corr} , breakdown potential (E_b), cathodic Tafel slope (β_c) and cathodic exchange current density ($i_{o,c}$) were also determined.

4.2.4. AC Measurements

EIS experiments were conducted using either a Solartron 1287TM electrochemical interface coupled with a Solartron 1250TM Frequency Response Analyzer (FRA) or a Gamry Reference 600TM potentiostat. The EIS spectra were recorded in the frequency range from 100 kHz to 1 mHz with 10 points per decade with an AC amplitude 10 mV by means of ZPlotTM or Gamry FrameworkTM software packages. Nyquist and Bode graphs were plotted using the acquired data. All measurements were repeated to ensure reproducibility.

The ZViewTM software package was used to analyse the acquired data. An equivalent circuit of each condition was constructed based on the surface film models derived from the STEM analysis as described in Sections 4.3.2 and 4.3.3. The equivalent circuit of each condition was then used to plot the simulated spectra. Subsequently, the values of electrical circuit parameters were extracted from the simulated results. Moreover, the Kramers-Kronig (K-K) transformation was applied to the proposed equivalent circuits to ensure that the fittings comply with K-K relations. This verifies that the measurements were acquired under steady-state conditions and that a system response is related to the applied perturbation voltages [5,6].

4.3. Magnesium Surface Film Analysis

Mg surface films were primarily examined by SEM-EDS and STEM-EDS from top view and cross-section respectively. Both surface analyses were carried out using the facilities located at the Canadian Centre for Electron Microscopy (CCEM) at McMaster University. A set of 4 square samples (1 cm^2) were cut from the Mg sheet. Samples were again annealed at 350°C for 0.5 h in ambient atmosphere and then quenched in H_2O . One of the samples was cold mounted and made into a working electrode using the procedure described in Section 4.2.1. All 4 samples were mechanically ground on SiC grinding papers up to a 4000 grit using anhydrous ethanol as lubricant. The 3 non-mounted samples were then immersed in separate beakers containing 500 mL of 3 different solutions of pure H_2O , 0.01 M NaCl, and 1 M NaOH. The samples were aged 48 h in pure H_2O , 24 h in 0.01 M NaCl, and 1 M NaOH at E_{corr} . A working electrode aged 24 h in 0.01 M NaCl at E_{corr} , was potentiostatically polarized 100 mV above the measured E_b for 0.5 h. Potentiostatic polarization was conducted in a 3 electrode electrochemical cell filled with 1000 mL of 0.01 M NaCl using a Gamry Reference 600TM potentiostat coupled with Gamry FrameworkTM software package. The electrode was removed after the test, rinsed with ethanol and dried. Afterwards, the 1 cm^2 Mg sample was extracted from the cold mount by cutting the surrounding epoxy and transferred to SEM/FIB.

No attempt was made to aerate or deaerate the test solution. Table 4.3 summarizes the sample preparation condition for all surface films formed for surface analysis. After removal from the test solution, the samples were rinsed with absolute ethanol, dried using

a stream of air, and then transferred to the SEM/FIB chamber. The total time to transport the exposed samples from the test cell to the SEM/FIB chamber was about 0.25 h.

Table 4.3: Sample preparation conditions for all surface films formed for surface analysis.

Solution	Immersion condition	Initial pH	Final pH
H ₂ O	48 h at E _{corr}	7.8	7.2
1 M NaOH	48 h at E _{corr}	14	14
0.01 M NaCl	24 h at E _{corr}	5.5	7.6
	24 h at E _{corr} + 0.5 h at +0.1 V vs. E _b	5.5	8.7

4.3.1. SEM-EDS Analysis

Samples exposed to H₂O and 1 M NaOH electrolytes were glued on an Al stub using a conductive Ag paste. The stubs were placed in a 50°C oven in ambient atmosphere to dry the Ag paste. A thin film of Pt was subsequently deposited on the specimens to facilitate high quality imaging without surface charging and the samples were then transferred to a JEOL 7000F SEM chamber for topographic examination. The SEM analysis was conducted to acquire plan view images from the surface film formed by exposure to the solutions listed in Table 4.3. All SEM images were obtained at an accelerating voltage of 5 kV and working distance of 8.8 mm and 10 mm for H₂O and 1 M NaOH samples respectively.

In order to conduct the SEM-EDS analysis on Mg samples immersed in 0.01 M NaCl and to choose the sites of interest for STEM-EDS cross-sections, samples were transferred to a ZEISS NVision 40 FIB/FE-SEM equipped with an Oxford Instrument Energy Dispersive X-ray Spectrometer (EDS). Plan view SEM images of the surface

films were collected at accelerating voltages of 2, 5 or 10 kV. The FIB image probe was also set at operating voltage of 30 kV with a probe current of 30 pA. EDS was used to quantify the composition of surface film.

4.3.2. FIB Sample Preparation

Different stages of STEM thin-foil preparation by FIB are presented in Figure 4.4. Selected sites of interest from the exposed samples were identified using SEM, then coated with either C or W to protect the corrosion film from beam damage during thin-foil preparation. Trenches on either side of the coated area were then milled away (Figure 4.4a) using Ga^+ at an accelerated voltage of 30 kV. The FIB-prepared thin foil sample was welded to a probe using C or W deposition, and the perimeter of the thin foil was milled away (Figure 4.4b) before being moved to a Cu grid and being welded in place (Figure 4.4c). Two thin windows were then ion-milled to produce a foil area thin enough to be electron transparent, approximately 70 nm in thickness (Figure 4.4d). The electron transparent thin foils were then transferred to TEM chamber.

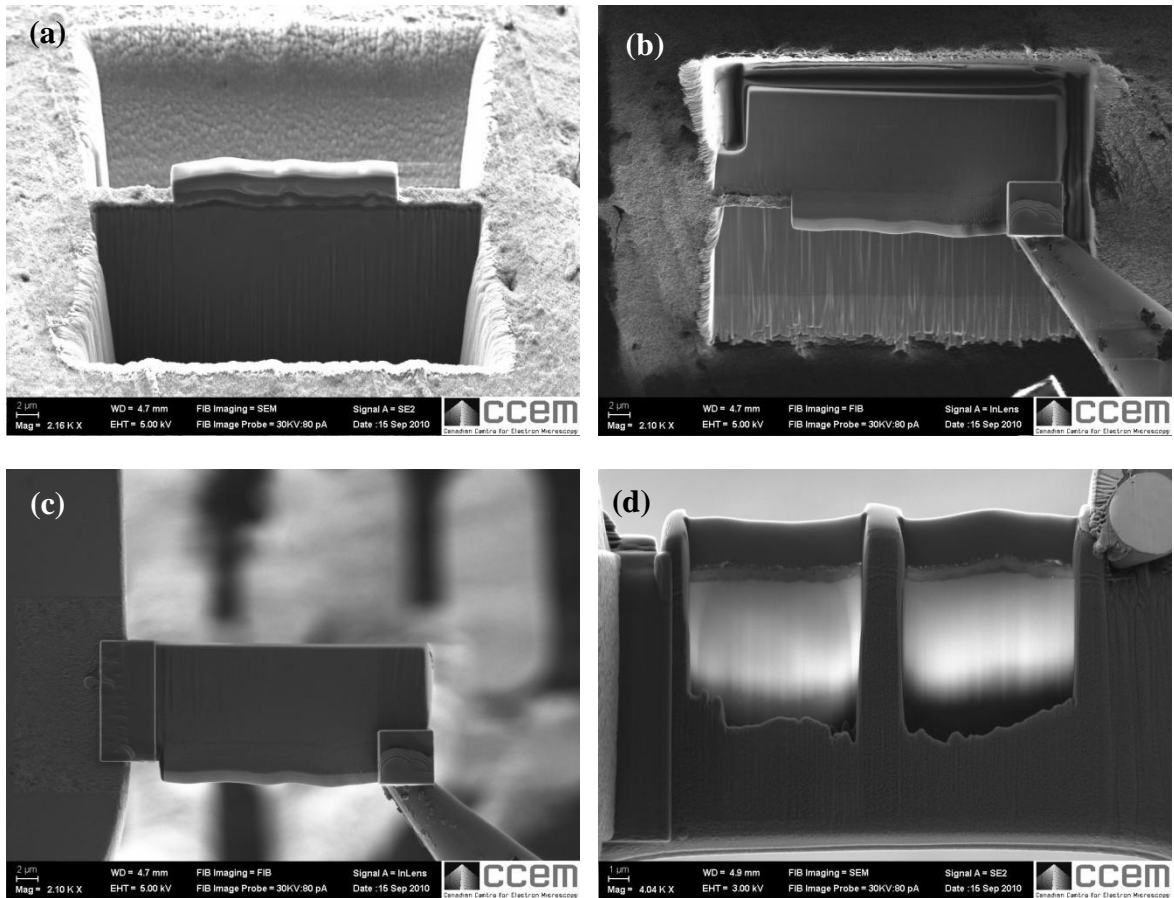


Figure 4.4: Stages in STEM thin-foil preparation using FIB (a) milling trenches on both sides of the sample, (b) milled sample perimeter and welding of the probe to the specimen, (c) sample welding to a Cu grid and probe removal, and (d) two electron transparent windows milled on the sample.

4.3.3. STEM-EDS Analysis

The thin foils were placed in a cryogenic holder capable of maintaining the foil temperature at -178°C . The STEM-EDS analyses on thin foils formed in H_2O and 1 M NaOH solutions were performed using a JEOL JEM-2010F field emission electron microscope equipped with an Oxford Instruments EDS analyzer operating at 200 kV. The thin foils of the surface film formed in 0.01 M NaCl solution were examined by a FEI

Titan 80-300 microscope equipped with an Oxford Instruments EDS analyzer at an accelerating voltage of 300 kV. Bright field (BF), selected area electron diffraction (SAD), and dark field (DF) images were primarily collected in TEM mode, whereas DF and High Angle Annular DF-(HAADF) images were acquired in STEM mode.

Numerous EDS point scans, line scans, and SmartMapsTM were acquired from different sites of interest across the film/substrate interface to examine the composition of the surface layers. EDS data acquisition and elemental quantification was performed using the INCA EnergyTM software package.

SmartMapTM provided the simultaneous acquisition of X-ray data from each pixel on a selected area of an image for most elements that were likely present. This analysis required minimal information regarding the composition and collected all of the X-ray data. This included the collection of numerous spectra from points or areas which were later quantified to create element maps and element line scans. The original mappings were later sub-divided into smaller rectangle/squares and were quantified to construct element concentration variations across the film/substrate interface.

In order to acquire SmartMapsTM in this study, sites of interest, primarily those across the film/substrate interface, were selected on the STEM DF-images. Mapping was carried out by rastering the electron beam over an area of the thin foil until sufficient X-ray counts were collected. Elemental maps were then acquired for Mg, O, Fe, Cl, and C from the selected rectangle/square-shaped sites of interest. The size of the selected areas was different for each film and was calculated using the scale bar on the STEM DF-images.

Mapping obtained O/Mg and Cl concentration depth profiles along the substrate/film interface. An example of this procedure is shown in Figure 4.5 for a site of interest mapped across the film/substrate interface. The procedure involved superimposing a grid of similarly sized ($30\text{ nm} \times 30\text{ nm}$) squares onto the entire mapped area ($240\text{ nm} \times 300\text{ nm}$), which was roughly centered on the film/substrate interface. The $30\text{ nm} \times 30\text{ nm}$ squares were the smallest that the INCA Energy™ software package allowed based on the magnification of the STEM DF-image and number of counts collected during mapping. Each of these squares contained an individual EDS spectrum, which was quantified in terms of the atomic concentration of both O and Mg using the Inca Energy™ software package. An average atomic concentration was calculated for both Mg and O for each row of squares. The average O/Mg atomic ratio for a given row was mapped to a depth, which was taken as the midpoint distance within each row of squares. The depths were measured relative to the film/substrate interface using the scale bar provided on the STEM DF-image.

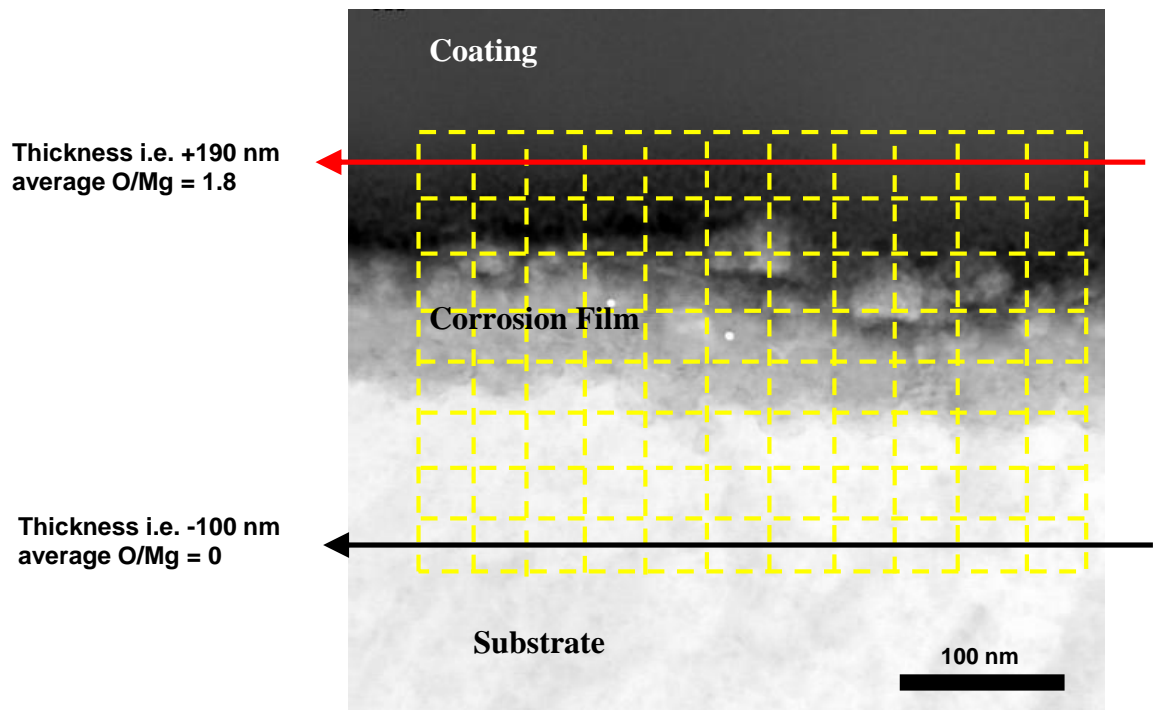


Figure 4.5 STEM DF-image of the film/substrate interface after 48h in 1 M NaOH showing the O/Mg depth profile calculation procedure.

5. FILM STRUCTURE RESULTS

5.1. Mechanically Polished Mg

Figure 5.1 shows the SEM plan view image of the Mg sample mechanically ground with SiC paper to a 4000 grit using ethanol as lubricant and polished up to 1 μm finish. This sample was examined as polished without being placed in a corroding system. The Mg microstructure contains a few inclusions within the matrix. Figure 5.1a and b show SE-SEM and BSE-SEM image of a subsurface particle, in which the adjacent area has been locally attacked during the mechanical polishing stage. This form of is an undermined area surrounding the impurity particle. EDS analysis of this particular inclusion indicates that it is likely a F, Si, and N containing particle.

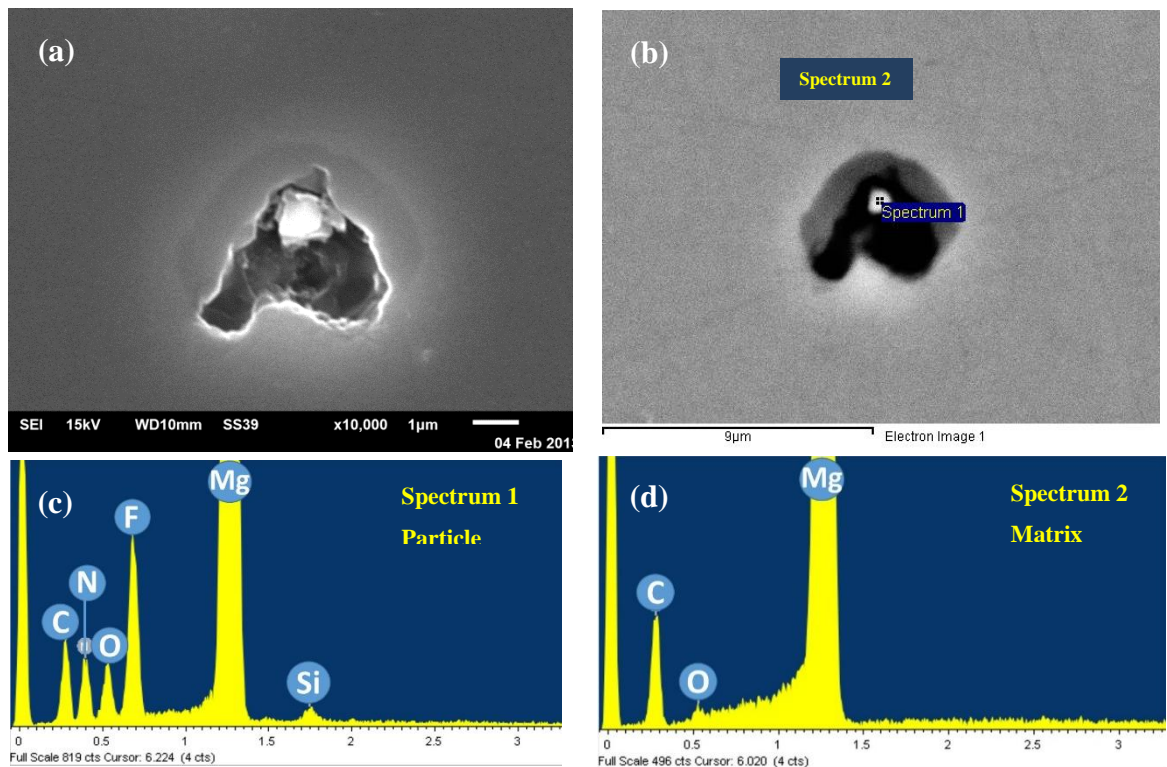


Figure 5.1: (a) SE-SEM and (b) BSE-SEM images of an embedded particle within the mechanically polished polycrystalline microstructure; (c) and (d) EDS spectra from the impurity particle and Mg matrix, respectively.

Similarly, Figure 5.2a-f show BSE-SEM images and corresponding EDS spectra of other embedded particles that are composed of F, Ca, Al, N, and Si containing particles.

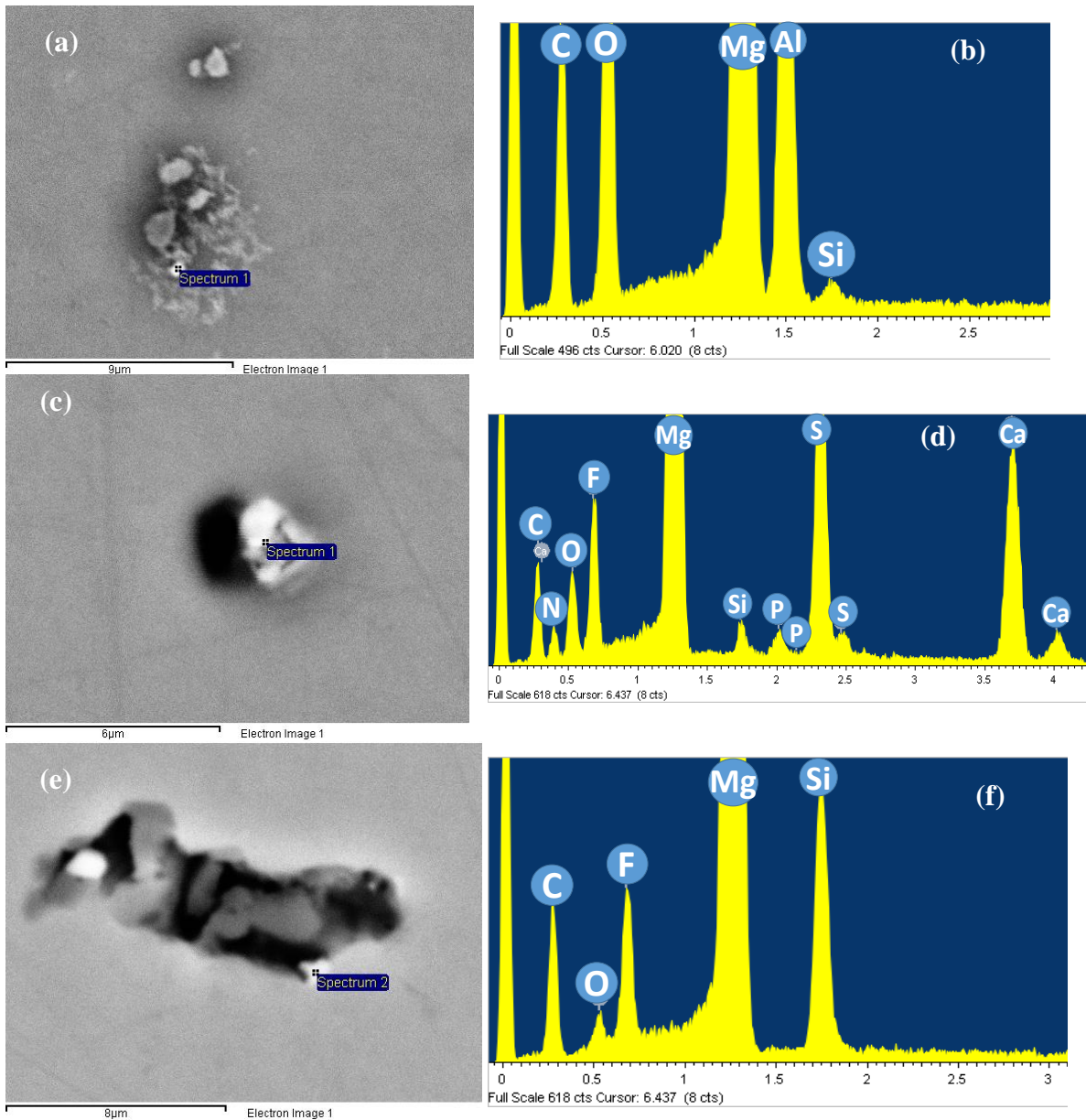


Figure 5.2: (a), (c), and (e) BSE-SEM image of some embedded impurity particle within the mechanically polished polycrystalline microstructure; (b), (d), and (f) EDS spectra from the impurity particle of (a), (c), and (e) images, respectively.

MgF₂ particles have been reported to form on molten Mg surface protected by SF₆ gas [105], [106], [107], [108]. These MgF₂ inclusions were found to be a few microns in diameter, embedded as a subsurface particle in the molten Mg bulk [108]. Furthermore, Si and Ca, as the major impurities of Mg ingots, have been reported to segregate at the surface of wrought Mg processed in presence of SF₆ gas [50], [105], [106], [109]. Ca was proposed to incorporate in the wrought Mg oxide film as CaO [105], [106], [109]. Although mechanical polishing and sputtering in conjunction with XPS have shown to reduce the presence of these elements at the surface, some embedded sub-surface particles are yet likely to exist within the Mg bulk, as shown in Figure 5.2. Similarly, S and N could have been trapped or formed as compound particles at the Mg surface due to utilization of SF₆ and N₂ gas [105], [106], [107], [108] during processing.

5.2. Pure H₂O

Figure 5.3 shows the E_{corr} transient measured immediately upon immersion in pure H₂O at room temperature for 48 h. Immediately upon immersion, the E_{corr} is found to slowly increase from a potential of about -1.83 V_{SCE} to a potential of about -1.54 V_{SCE}. This initial increase in E_{corr} occurs over about a 2 h period. After this slow initial increase, the corrosion potential remains relatively stable at a potential of about -1.54 V_{SCE} for the following 46 h. This test was repeated 3 times during which the steady state potential values are within a ± 5 mV reading range, confirming the reproducibility of the E_{corr} measurement.

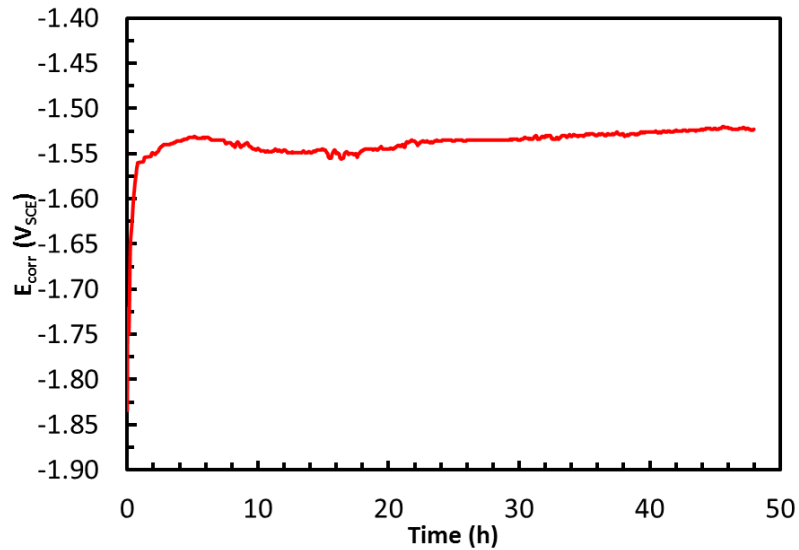


Figure 5.3: E_{corr} transient of 4N Mg exposed to pure H₂O for 48 h.

Figure 5.4a shows a SEM plan view image of the surface film formed on the Mg sample after 48 h exposure to pure H₂O. The film appears to be composed of 100-200 nm platelets. Numerous cracks appear through the film. Figure 5.4b shows a crack in more detail.

Figure 5.5 shows a BF-TEM image of the surface film, in cross-section. The film is continuous and adhered to the surface of the Mg substrate. The film exhibits different contrast for the areas adjacent to the substrate along the film interface. This contrast difference suggests the presence of a crystallographic and/or a mass-thickness/density variation between the areas adjacent to and away from the Mg/film interface [110].

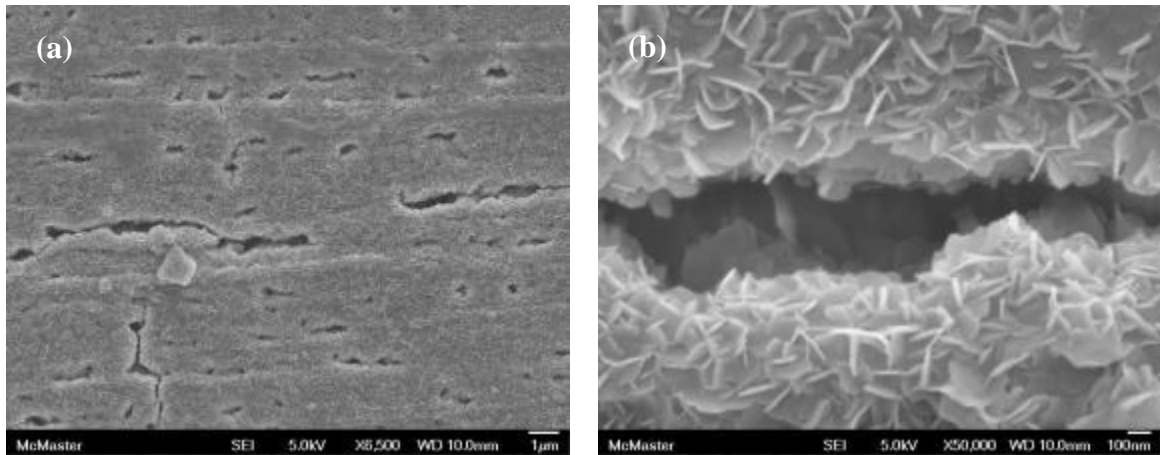


Figure 5.4: (a) and (b) SE-SEM images of Mg sample surface aged 48 h in H₂O at different magnification showing platelets and cracking within the film.

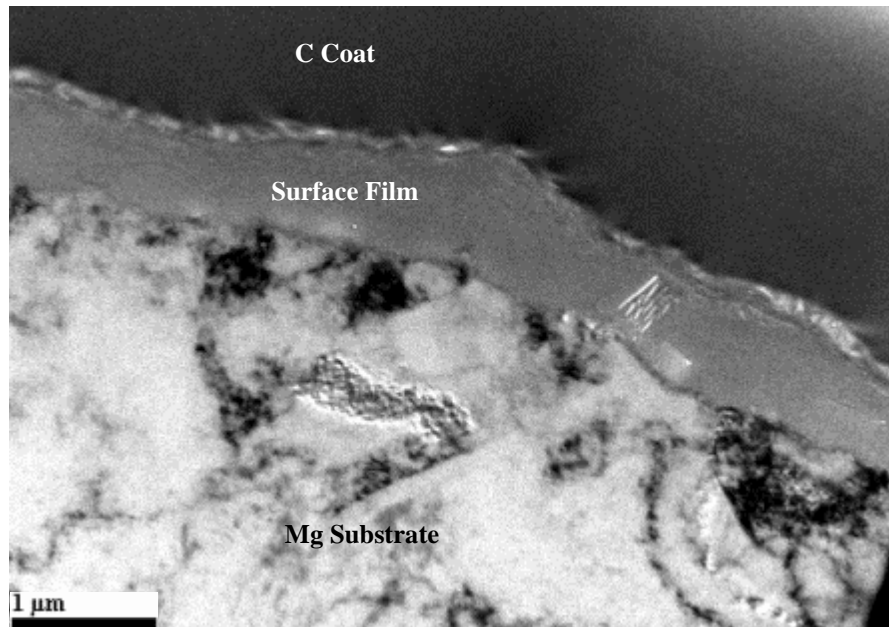


Figure 5.5: TEM BF image showing, in cross-section, the surface film on the Mg sample formed by exposure to pure H₂O at E_{corr} for 48 h.

Another BF-TEM image (Figure 5.6) of the Mg/film interface contains bright and dark regions within the film, which indicate a heterogeneous structure. Variations in mass-thickness/density and/or crystallographic orientation can cause variations in elastic scattering in the specimen. Areas with higher thickness, density or mass undergo more elastic scattering, and therefore appear darker in a TEM BF-image. Since the Mg thin-foil

was prepared using FIB, the thickness variation is less likely compared to mass and density variation, albeit not totally absent. Furthermore, electron scattering occurring at Bragg angles with the crystallographic structure of the material can cause diffraction contrast. Therefore, Figure 5.6 may include diffraction contrast, as well as the mass-thickness contrast. Consequently, a diffraction pattern from this area (Figure 5.7) and a subsequent DF-TEM image from a significant diffraction angle and direction (Figure 5.8) presents a better image of the diffraction contrast present in the BF image. Moreover, ADF and/or HAADF STEM imaging (Figure 5.9a) provides better mass-thickness contrast (with poorer diffraction contrast) due to lower diffraction scattering cross-sections at such these high angles [110].

The dark regions in Figure 5.6 are more concentrated into localized areas situated adjacent to the Mg/film interface, whereas they are more diffuse within the layer away from the interface. The bright regions are only concentrated in the film adjacent to the interface with the substrate. Interestingly, no evidence of a platelet-like structure was observed. This image also shows the rough nature of the Mg substrate surface, which is consistent with it being dissolved.

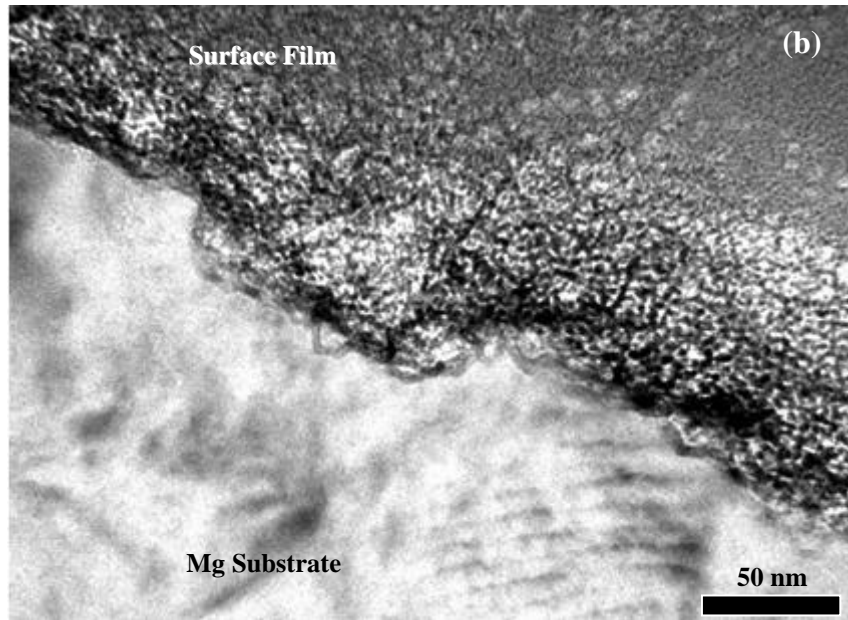


Figure 5.6: TEM BF image of the Mg/film interface, as formed after aging at E_{corr} in pure H_2O at room temperature for 48 h.

Figure 5.7 shows a diffraction pattern obtained from the Mg/film interface. Analysis of the pattern yields a lattice plane separation (d-spacing) of 0.210 and 0.149 nm for the two inner fullest diffractions rings present in the pattern. These d-spacings are, respectively, most consistent with the {200} and {220} crystallographic planes in the face centered cubic MgO substrate, as comparatively shown in Table 5.1. Furthermore, the MgO SAD ring pattern was simulated using the JEMS software package and published crystallographic data for MgO [111]. The simulated MgO polycrystalline ring pattern is superimposed on acquired pattern in Figure 5.7, which indicates a good agreement indicates that the obtained pattern corresponds to the MgO.

Figure 5.8 shows a selected area DF-image of this interface region, in which the {200} crystallographic plane of MgO is selected using the SAD technique. The extent of crystallinity, as defined by the {200} plane in MgO, is found to be predominantly nano-

sized crystals within the film, adjacent to the Mg/film interface. These nano-sized crystals appear as the bright spots adjacent to the Mg/film interface, in which the scattered electrons are diffracted by their sets of specific hkl orientation and collected using SAD aperture. Consequently, the dark features (observed in Figure 5.6) are attributed to a less porous film (likely nano-crystalline regions), whereas the bright regions are attributed to porosity.

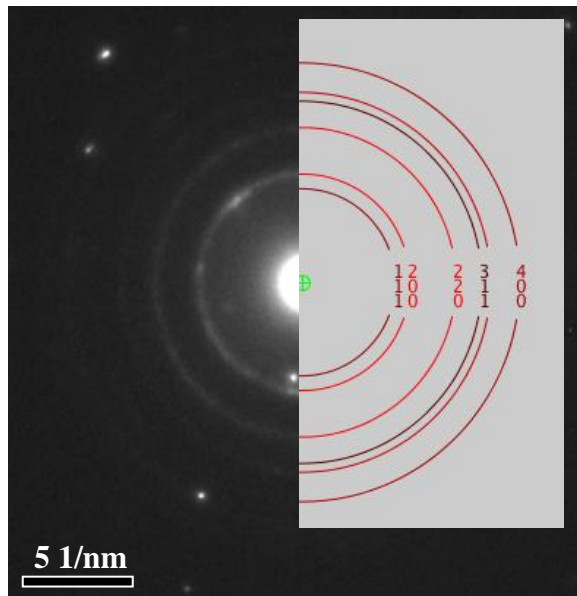


Figure 5.7: Diffraction pattern obtained from the Mg/film interface.

Table 5.1: Diffraction analysis data obtained from the Mg/film interface, as shown in Figure 5.7.

Ring	Calculated d-spacing (Å)	MgO (fcc) [112]		Mg(OH) ₂ (hcp) [112]		Mg (hcp) [112]	
		d-spacing (Å)	(<i>h k l</i>)	d-spacing (Å)	(<i>h k l</i>)	d-spacing (Å)	(<i>h k l</i>)
1	2.15 Å	2.1099	(200)	2.3493	(001)	1.8970	(102)
2	1.49 Å	1.4919	(220)	1.4851	(111)	1.4700	(103)
3	1.22 Å	1.2181	(222)	1.1775	(004)	1.2237	(202)

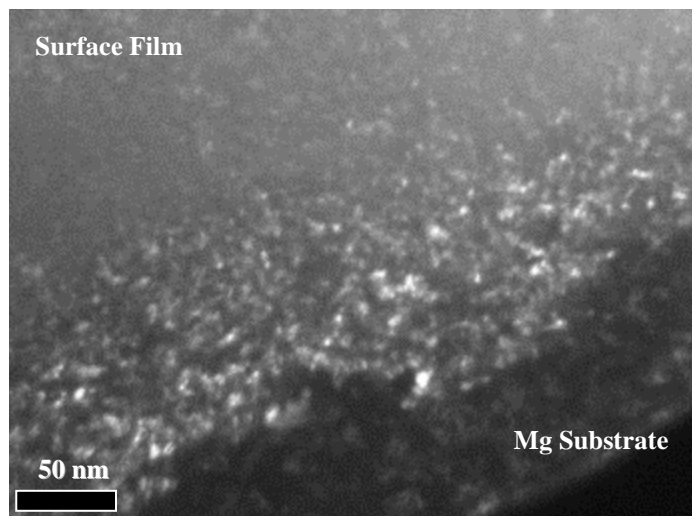


Figure 5.8: TEM dark-field image of the Mg/film interface region showing the extent of nano-crystalline region, as defined by the {200} spacing in MgO.

Figure 5.9 shows the results of the element maps collected across the Mg/film interface formed in H₂O using EDS. Not surprisingly, the intensity of the Mg signal is highest in the substrate and lowest in the film furthest away from the interface, whereas the intensity of the O signal is highest in the film and lowest in the substrate. Unfortunately, little information can be extracted from the C map in terms of the distribution within the film since it is unclear whether a genuine signal has detected. Nevertheless, there does not appear to be any significant enrichment of C within the film.

The sum spectrum of the selected EDS analysis area is shown in Figure 5.10. The Cu characteristic peak is likely due to the Cu TEM grid, and the Ga peak is due to Ga⁺ ion beam used in FIB sample preparation technique. The C peak could also be either from surface contaminations or the C top coat applied before FIB cross-sectioning. Figure 5.11 shows a plot of the O/Mg atomic ratio as a function of position across the Mg/film interface. The solid line represents the average O/Mg ratio for that position relative to the Mg/film interface. For positions within the Mg substrate, the calculated average O/Mg

atomic ratio is relatively small. In contrast, the average ratio calculated for positions in the film, both adjacent and away from the interface, are significantly larger, yet dissimilar.

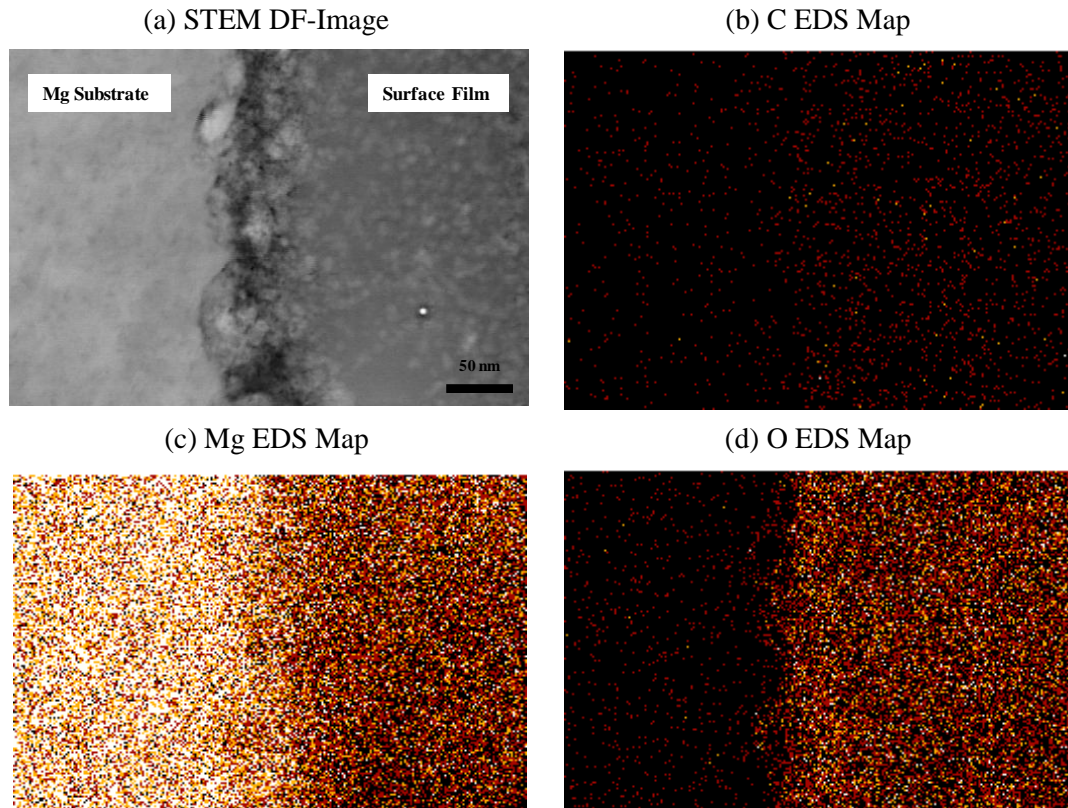


Figure 5.9: (a) STEM DF-image of the Mg/film interface, formed after aging at E_{corr} in pure H_2O at room temperature for 48 h, utilized to capture (b) a C EDS map, (c) a Mg EDS map and (d) an O EDS map.

The average ratio is just above 1 for positions adjacent to the interface, whereas it is about 2 for positions away from the interface. This suggests the film is a bilayer structure, albeit diffuse. These calculated average ratios are consistent with the thinner inner layer being mainly comprised of MgO and the thicker outer layer being mainly comprised of $\text{Mg}(\text{OH})_2$. The spatial resolution of the EDS technique is limited by beam spreading, estimated in the worst case scenario in Mg as 4 nm at 200 keV for a 100 nm thick sample.

Therefore, the apparent change in concentration in the profile is related to a change in composition combined with a possible interface roughness in the direction of propagation of the beam [113].

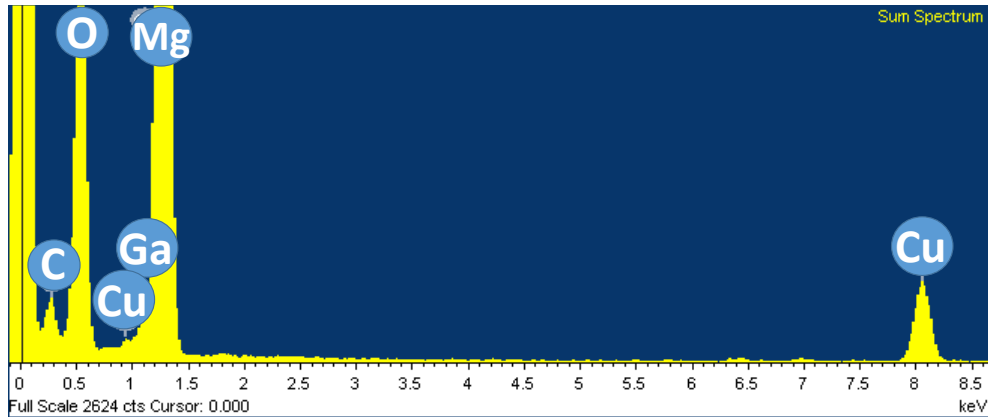


Figure 5.10: EDS sum spectrum of the SmartMap™ characteristic section analyzed in Figure 5.9.

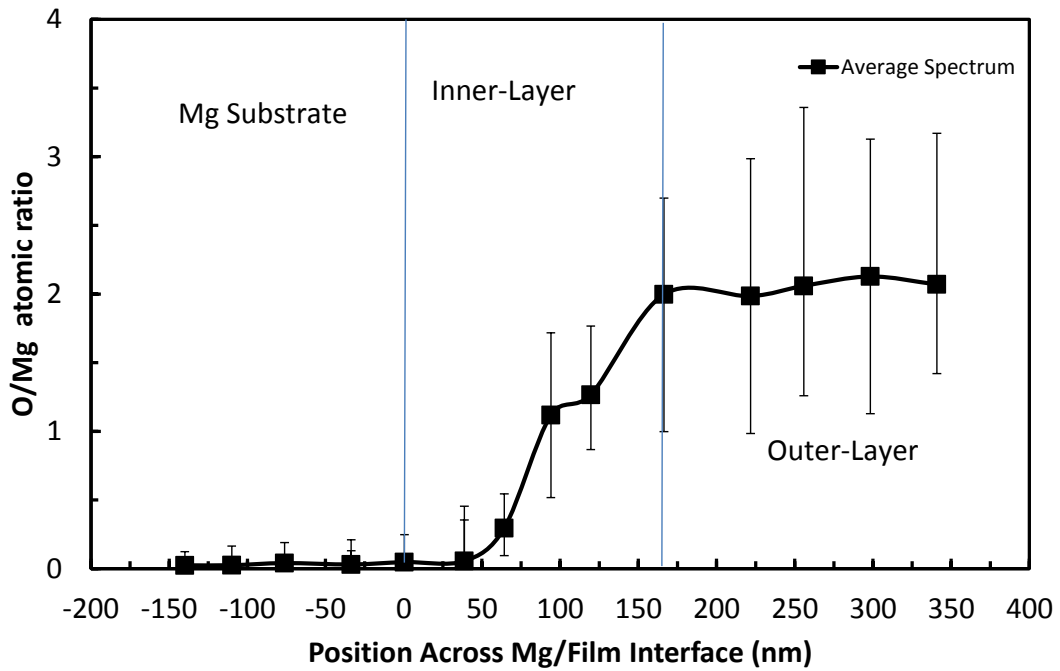


Figure 5.11: Plot of the calculated atomic O/Mg ratio as a function of position across the interface between the surface film and the Mg substrate.

5.2. 0.01 M NaCl

The Mg E_{corr} transient measured immediately upon exposure in 0.01 M NaCl for 24 h maintained at room temperature is shown Figure 5.12. Similar to pure H₂O measurement, the E_{corr} increases rapidly from -1.87 V_{SCE} to -1.57 V_{SCE} and slowly levels off after 0.3 h at -1.55 V_{SCE}. This test was also repeated to confirm the reproducibility of the measurement. Repeated tests showed that the steady state potential values are in a ± 5 mV range, which confirms the reproducibility of the measurement.

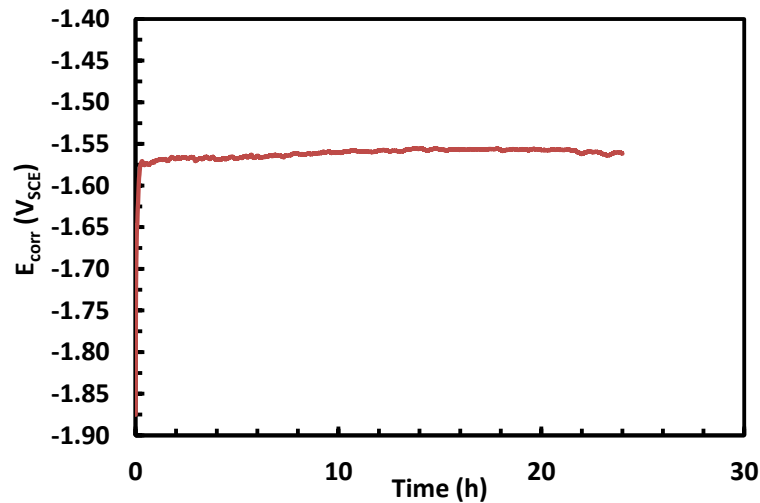


Figure 5.12: E_{corr} transient of 4N Mg exposed to 0.01 M NaCl for 24 h.

The potentiodynamic polarization curve measured in 0.01 M NaCl solutions after aging for 24 h is shown in Figure 5.13. This test was repeated to ensure the reproducibility. The average electrochemical kinetic parameters, including E_{corr} , i_{corr} , β_c , and E_b are calculated and summarized in Table 5.2. These values are also superimposed on the polarization curve, shown in Figure 5.13. The E_b measured -1.1 V_{SCE}, 0.4 V more

noble than the E_{corr} , measured as $-1.50 V_{SCE}$. The i_{corr} , estimated by Tafel extrapolation, was $5 \mu A/cm^2$.

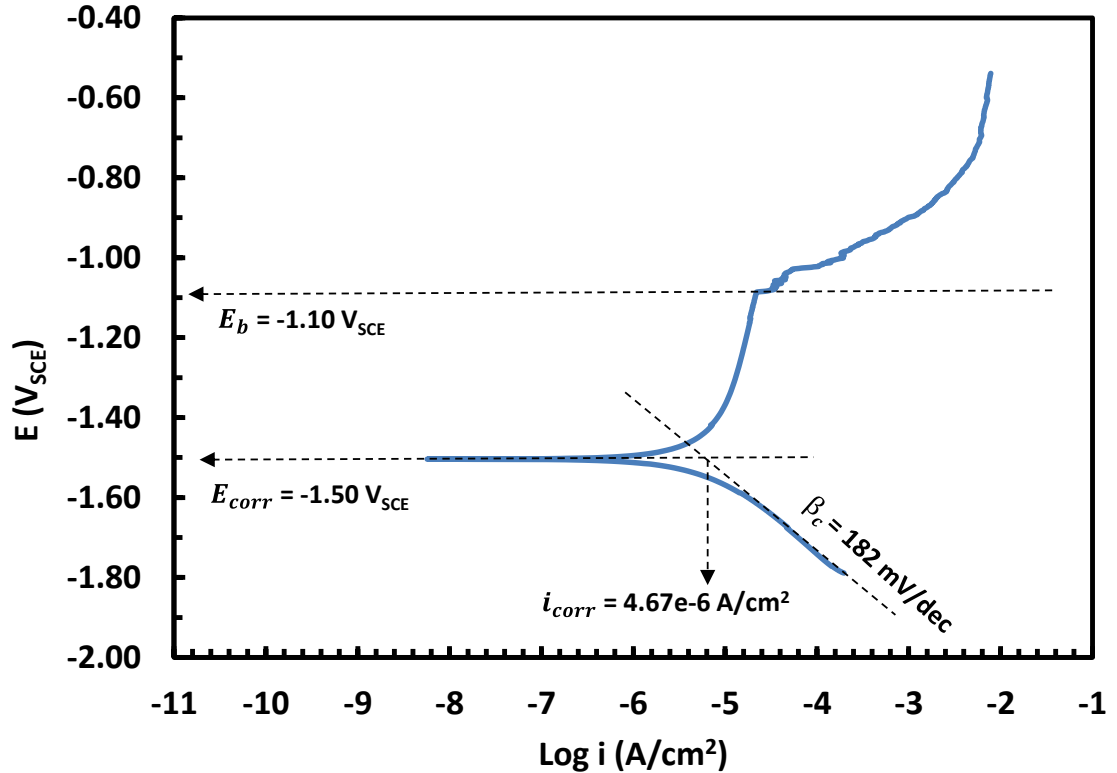


Figure 5.13: Potentiodynamic polarization curves of 4N Mg, after aging at E_{corr} for 24 h in 0.01 M NaCl solution.

Table 5.2: Electrochemical kinetic parameters extracted from potentiodynamic polarization curves recorded for Mg in 0.01 M NaCl

Aging time	E_{corr} (V_{SCE})	i_{corr} (A/cm^2)	β_c (V/dec)	E_b (V_{SCE})
24h	-1.50	4.67E-06	0.182	-1.10

Figure 5.14 shows the variation of current density with time under potentiostatic exposure at $+0.1 V$ vs. E_b ($-1 V_{SCE}$) in 0.01 M NaCl solution for 0.5 h. The measured current density is anodic for the entire hold time. The anodic current density exhibits a slight increase at times up to nearly 200 s of potentiostatic exposure, while the electrode

surface remains unaffected. Subsequently, the electrode surface started to show an intense evolution of gas bubbles (likely H₂) on randomly distributed locations. This is coupled with a sharp increase of the anodic current density up to 2 mA/cm² after 400 s of hold time, in which dark pits initiated underneath gas evolution locations. Beyond this time, the current density leveled off and pits continued a steady-state radial growth until the cell was shut down at 1800 s. The electrode surface after exposure is shown in Figure 5.15a. Figure 5.15b shows the Mg surface, once removed from the solution and dried.

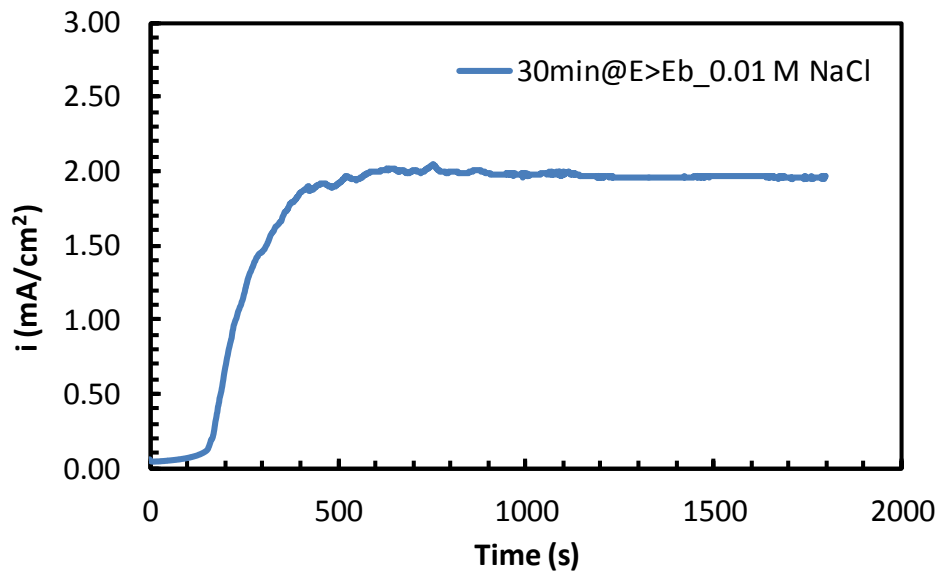


Figure 5.14: Potentiostatic diagram of Mg held 0.5 h at +0.1 V vs. E_b (1 V_{SCE}) after 24 h aging in 0.01 M NaCl.

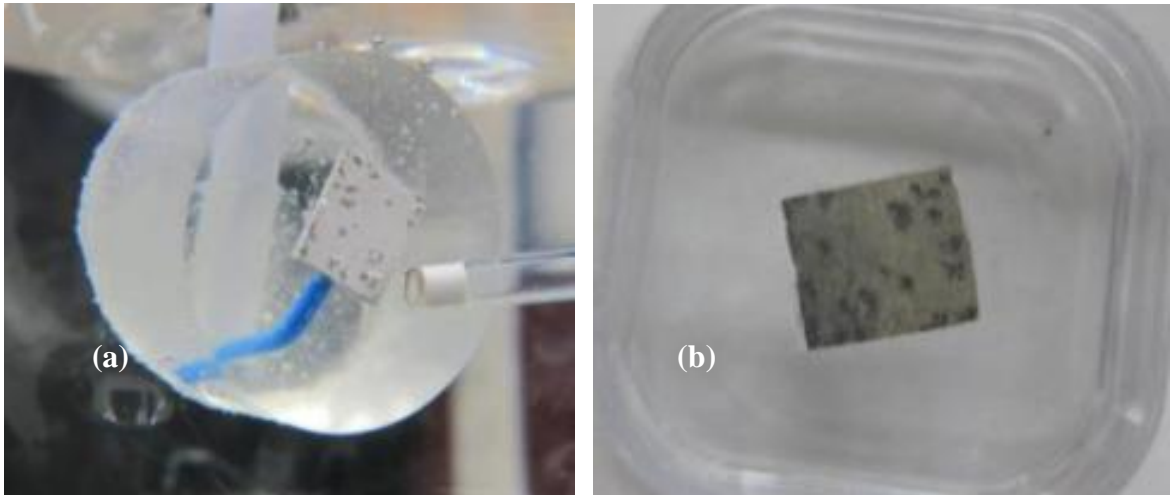


Figure 5.15: Characteristic surface appearance of 24 h aged Mg sample after 0.5 h potentiostatic exposure (a) in 0.01 M NaCl 0.1 V above E_b (b) Dried sample after the test.

5.2.1. Film Formed at E_{corr}

The film formed in 0.01 M NaCl solution after 24 h exposure at E_{corr} (Figure 5.16), exhibits a similar structure as the film formed in pure H_2O . The film consists of platelets, and is cracked to a significant degree (Figure 5.16a and b).

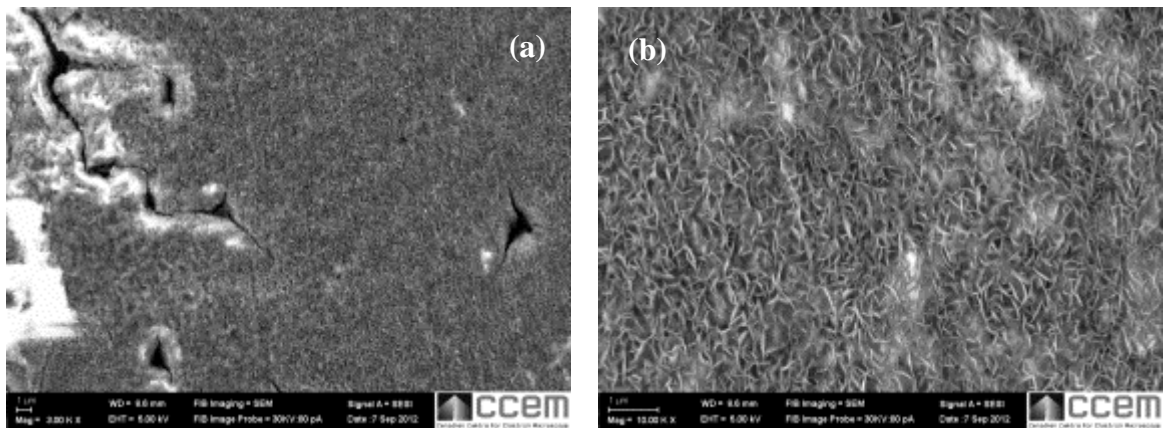


Figure 5.16: SEM images of the film, in plan view, formed on Mg after exposure to 0.01 M NaCl for 24 h at E_{corr} , (a) low magnification, (b) and high magnification.

A plan view SE-SEM image of a crack is shown in more detail in Figure 5.17a. Interestingly, platelets are observed within the crack. Figure 5.17a and Figure 5.17b show

the locations where an EDS analysis were captured and the corresponding spectra are presented in Figure 5.17c and Figure 5.17d respectively. The crack contains small amounts of Si and Cl, whereas neither Si nor Cl was observed adjacent to the crack. Additionally, a higher O intensity is observed inside the crack than that observed outside.

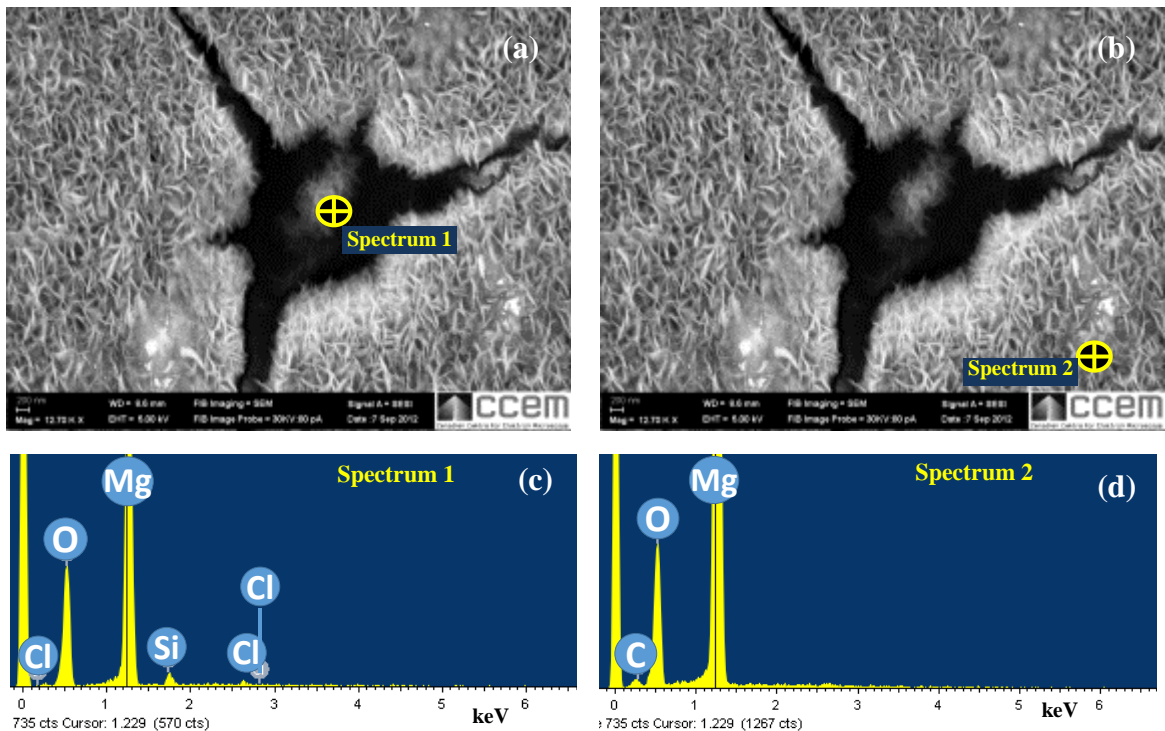


Figure 5.17: (a) and (b) SEM images, and (c) and (d) EDS spectra of Mg surface aged for 24 h in 0.01 M NaCl showing the cracked platelet film.

Figure 5.18 indicates another feature, a cracked nodule. EDS spectra (Figure 5.18c-d) were acquired from the nodule, as well as the adjacent film. The cracked nodule exhibits a higher O intensity compared to that acquired from the adjacent film. This suggests that the nodule likely consists of more O containing corrosion product, such as $Mg(OH)_2$.

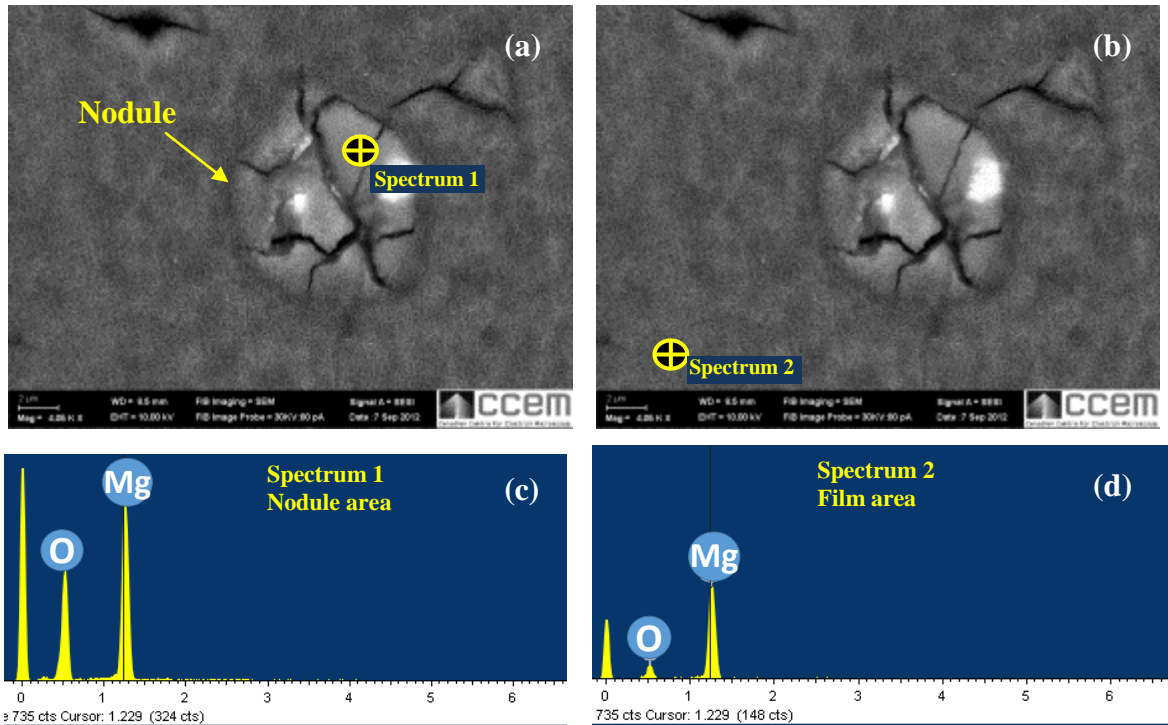


Figure 5.18: (a) and (b) SEM images, and (c) and (d) EDS spectra of Mg surface aged for 24 h in 0.01 M NaCl showing a nodule residing on film.

Figure 5.19a-b show rectangular shaped embedded particles within the film. The particles, also tend to be present along with cracks. Si exhibits the highest EDS intensity, while C is also identified along with Mg and O. These results suggest the presence of Mg_2Si or SiC particles embedded during the mechanical polishing stage.

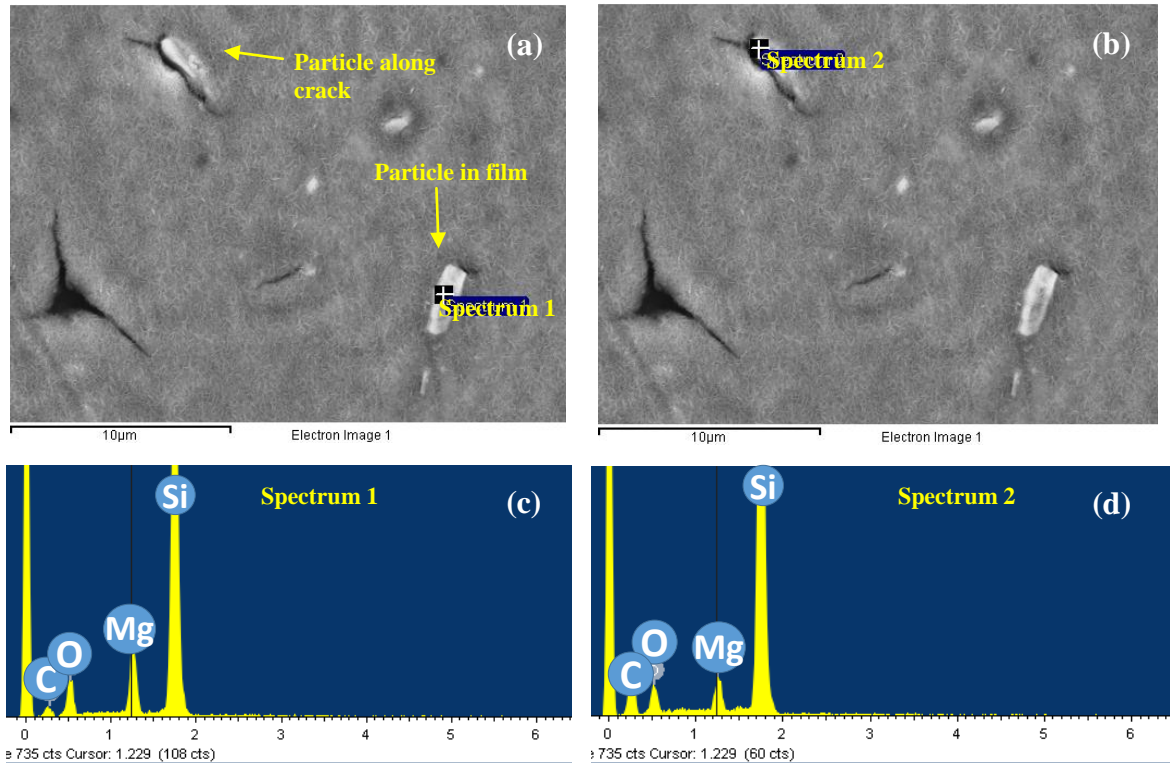


Figure 5.19: (a) and (b) SEM images, (c) and (d) EDS spectra of Mg surface aged for 24 h in 0.01 M NaCl showing Si containing embedded particles within the film.

Figure 5.20a and Figure 5.20b show the SEM plan view image of the location selected for FIB milling. The EDS spectrum of the selected site is also displayed in Figure 5.20c. Note that this location was chosen since the EDS spectra results confirmed that this site contains Cl as well as Mg and O. Furthermore, surface damage can be seen adjacent to the selected site. This damage neither resembles a pit nor a filliform damage, which are usually observed on corroded Mg surface formed in more aggressive saline environments at E_{corr} or above E_b [2], [4], [14]. Generally, pit and/or filliform damage are visually observed to initiate as dark spots on the Mg electrode and grow in size with prolonged exposure times, but this was not observed for this sample.

The TEM bright-field image shown in Figure 5.21 displays the general features of the film, in cross-section. It appears to be continuous and adhered to the surface of the Mg substrate; however the surface of the film seems to be rougher than that formed in H₂O. As shown in the image, the film is about 700 nm thick.

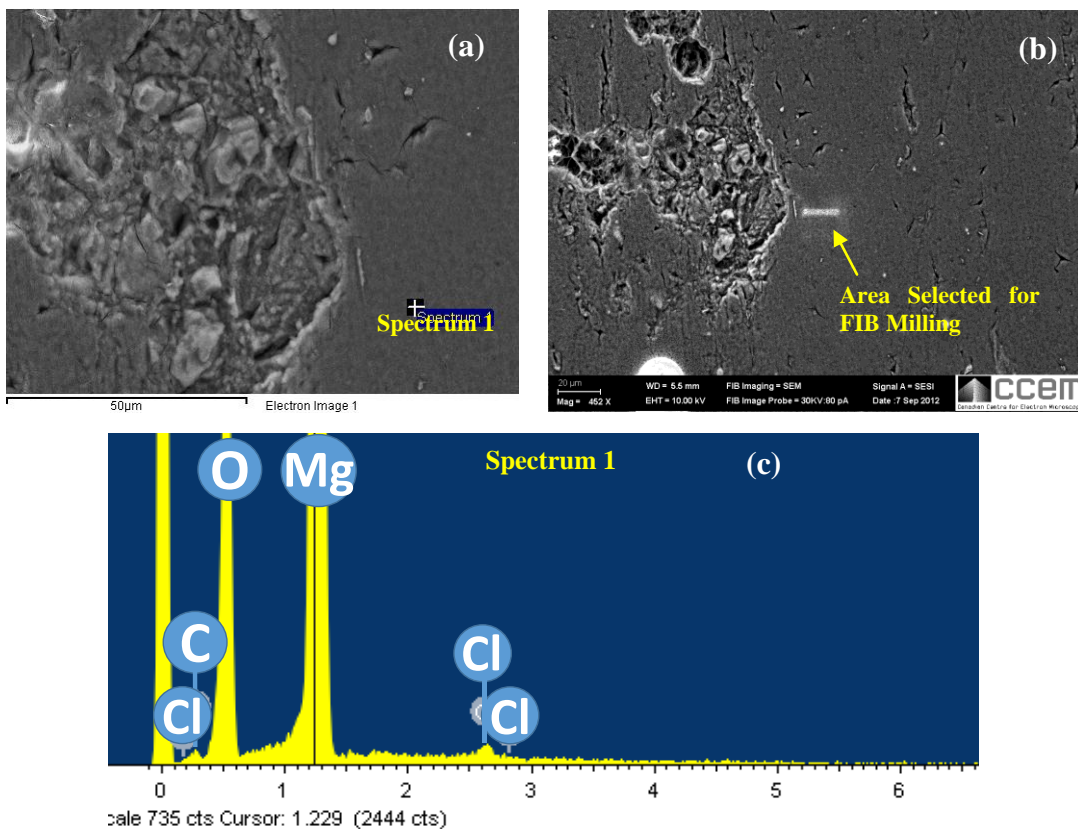


Figure 5.20: (a) and (b) SEM images, and (c) EDS spectrum from area selected for FIB milling of 24 h aged Mg sample in 0.01 M NaCl.

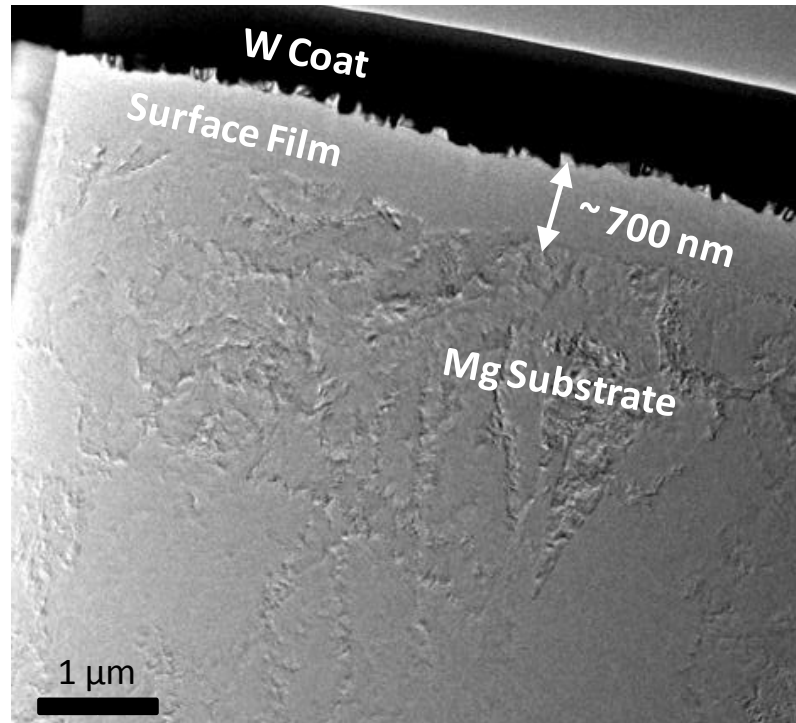


Figure 5.21: TEM BF-image showing, in cross-section, the film on the Mg sample formed by exposure to 0.01 M NaCl at E_{corr} for 24 h.

A more detailed STEM DF-image of the surface film formed is shown in Figure 5.22a. Similar to that observed on the H₂O sample, the film adjacent to Mg/film interface exhibits a different contrast than that far removed from the Mg/film interface. This indicates that the film has a bi-layer structure, in which a thicker outer-layer of about 300-600 nm is formed on top of a 50-100 nm thick inner-layer. Since in DF-STEM imaging the diffraction contrast is poor, the mass-thickness contrast dominates. Moreover, the FIB prepared samples exhibit relatively uniform thickness. Therefore, the observed contrast generated is likely due to different elastic scattering of the transmitted electron beam within the specimen caused by variations in mass or density [110].

The outer-layer appears to be composed of numerous dark regions (porosity). The size of these dark spots reaches nearly to 50 nm at some locations. This suggests that the

outer-layer is significantly porous. Furthermore, the brighter appearance of the inner-layer versus the outer-layer implies a lower porosity at the areas adjacent to the Mg/film interface. A higher magnification DF-STEM view of the Mg/film interface (Figure 5.22b) confirms the porous nature of the inner-layer film along with the rough nature of the Mg substrate surface. This is consistent with the Mg substrate being corroded. Moreover, HR-TEM BF-image of the interface verifies the presence of randomly oriented nano-crystals within the inner-layer (Figure 5.22c).

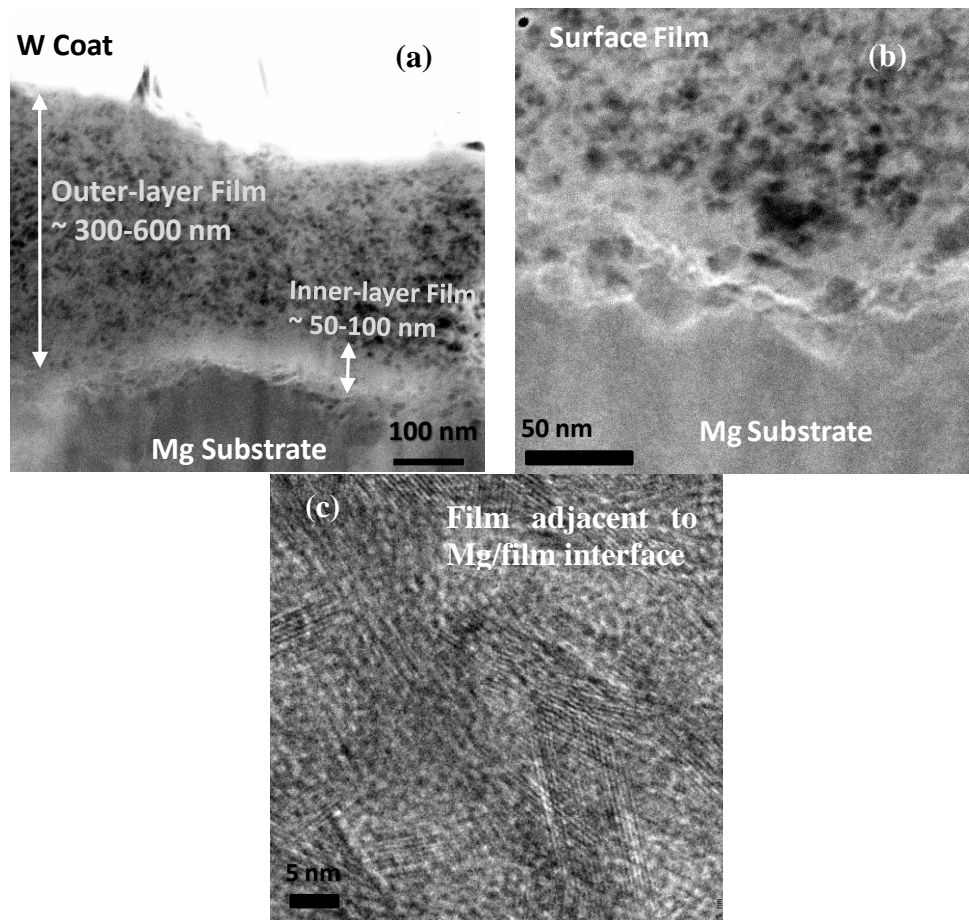


Figure 5.22: (a) and (b) STEM DF-images of Mg surface film formed after exposure to 0.01 M NaCl at E_{corr} for 24 h, (c) HR-TEM image of the film adjacent to the Mg/film interface.

The SAD pattern acquired from the Mg/film interface region, is shown in Figure 5.23a. A simulated ring pattern simulated using JEMS software package and published crystallographic data for MgO, is superimposed on the acquired diffraction pattern [110]. The ring pattern corresponds to polycrystalline MgO. Moreover, using SAD technique, a DF-TEM image of the Mg/film interface region was captured, in which the {200}/{220} reflections of the cubic MgO structure are highlighted (Figure 5.23b). The surface film adjacent to the Mg/film interface is found to have more crystallinity, as defined by having more of the {200} and {220} planes in MgO. The number of MgO nano-crystals appears to gradually diminish within the outer-layer.

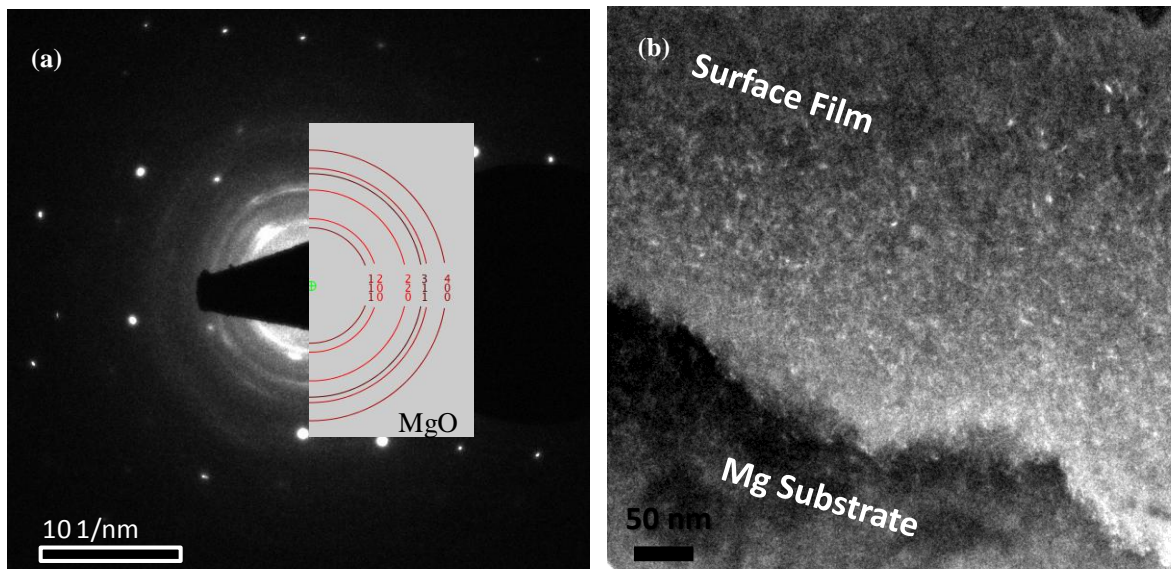


Figure 5.23: (a) SAD pattern acquired from the film/substrate interface after exposure to 0.01 M NaCl at E_{corr} for 24 h; DF- TEM image of the film/substrate, as defined by the {200} and {220} reflections of the cubic MgO structure.

A characteristic section of the film formed was identified and is shown in Figure 5.24a. The corresponding SmartMap™ across the Mg/film interface was collected for the elements of interest (Mg, O, Cl and W) and is displayed in Figure 5.24b-e.

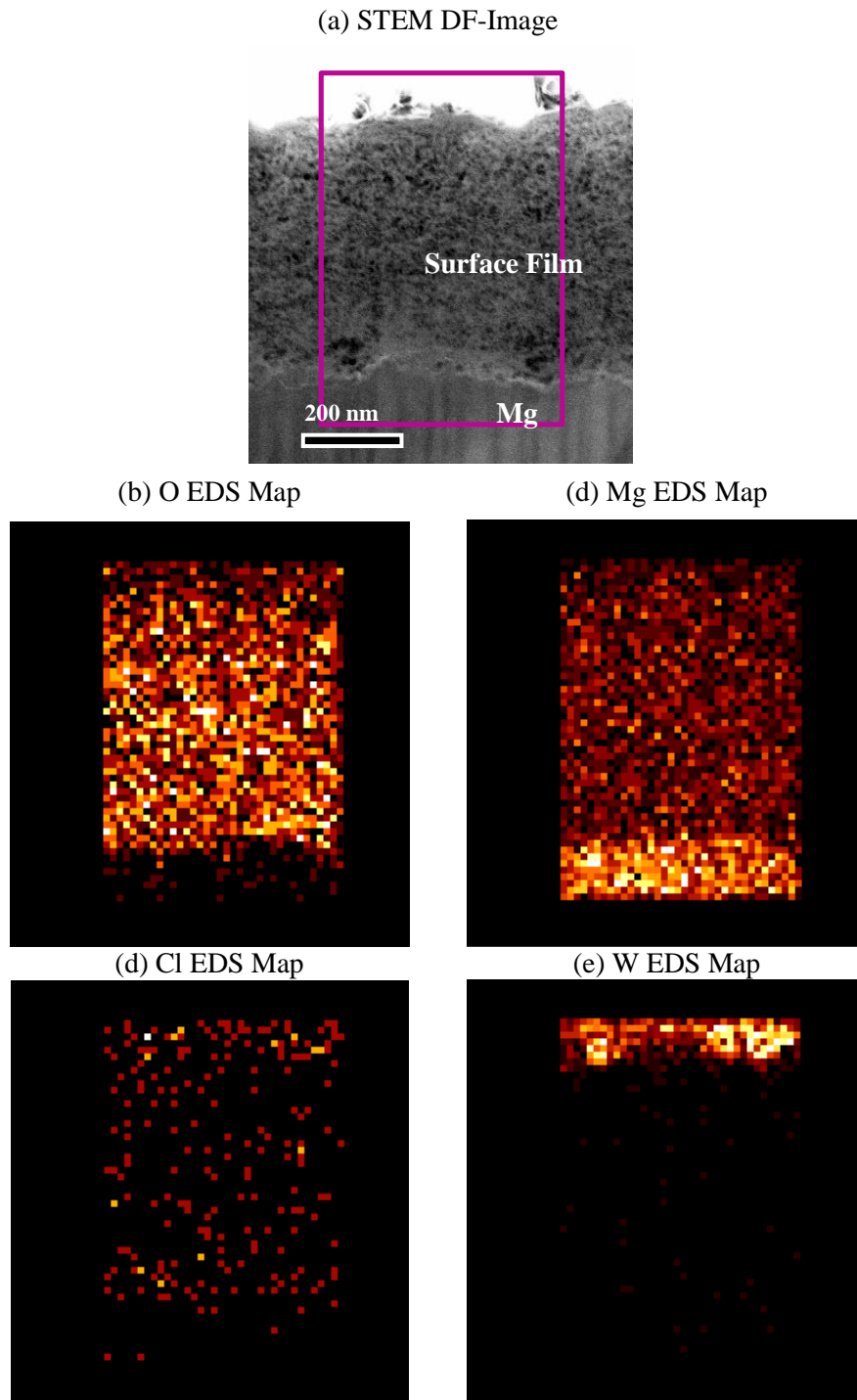


Figure 5.24: (a) STEM DF-image of the film formed on Mg exposed to 0.01 M NaCl after 24 h aging at E_{corr} , utilized to capture an (b) O EDS map, (c) Mg EDS map, (d) Cl EDS map and (e) W EDS map.

As expected, the intensity of W is highest in the coated W layer. Also, the intensity of the Mg signal is lowest in the film away from the interface and highest in the substrate, whereas O intensity shows the opposite trend. The Cl map exhibits no significant enrichment within the film. However, since Cl characteristic peaks were identified in the sum spectrum of the selected area (Figure 5.25), Cl likely exists within the film.

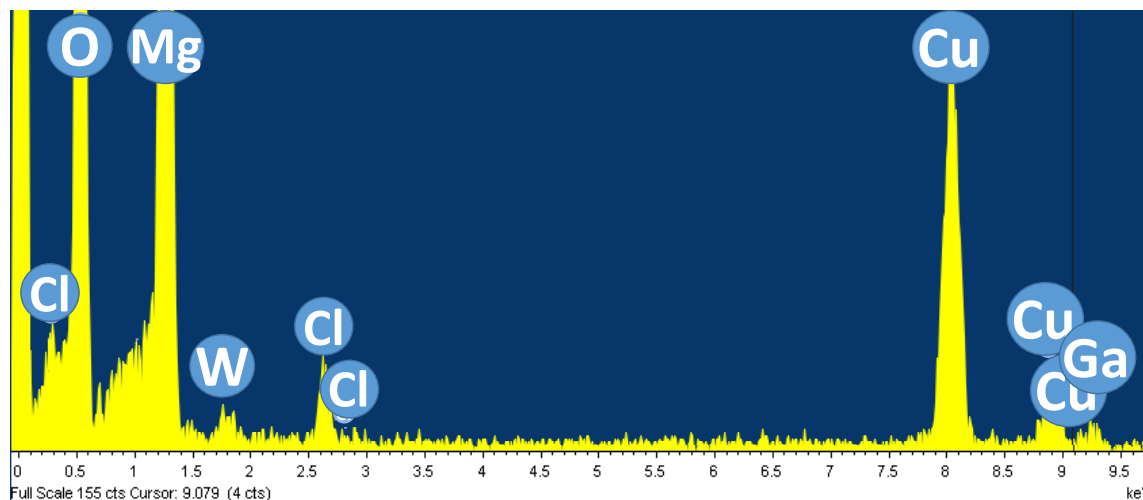


Figure 5.25: Sum spectrum of the SmartMap™ characteristic section analyzed in Figure 5.24.

The O/Mg atomic ratio depth profile across the Mg/film interface is shown in Figure 5.26. The calculated average O/Mg atomic ratio of the positions within the Mg substrate is relatively small (Figure 5.26), whereas the film adjacent to and away from the interface exhibits significantly larger values. For the positions adjacent to the interface, the calculated average ratio is about 1, which is consistent with the formation of a MgO-rich layer. In contrast, the positions away from the interface acquired an average O/Mg atomic ratio of higher than 2, which is more consistent with the formation of a Mg(OH)₂-rich layer. Some average O/Mg atomic ratios are greater than 2; however, the O/Mg

atomic ratio of 2 lies between the error bars, as defined by the standard deviation of the quantified data. This confirms the outer layer being a $\text{Mg}(\text{OH})_2$ -rich layer. A question may arise here is that whether the formation of other forms of oxide/hydroxide or Mg-Cl compounds have affected the mean value of the O/Mg atomic ratios. Examining this requires more accurate surface analysis measurements such as XPS and SIMS.

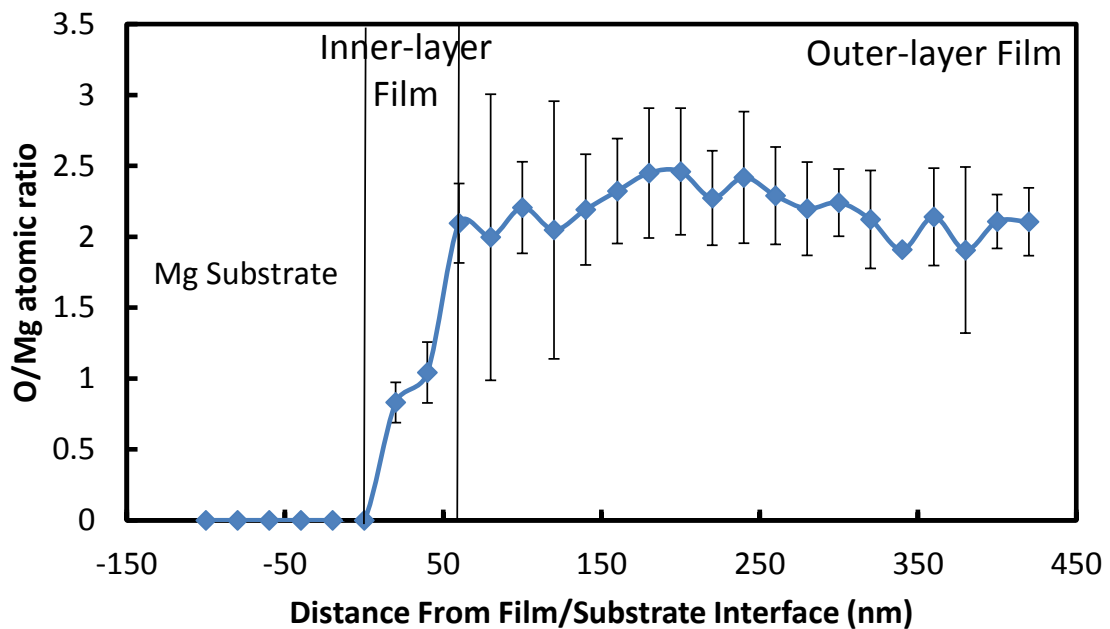


Figure 5.26: O/Mg atomic ratio depth profile through the Mg/film interface, and the Mg substrate on Mg exposed to 0.01 M NaCl after 24 h aging at E_{corr} .

5.2.2. Anodic Film

The plan view SEM image of a pit formed on the surface after 24 h aging at E_{corr} then potentiostatic polarization at +0.1 V vs. E_b for 0.5 h in 0.01 M NaCl is shown in Figure 5.27a. Interestingly, it can be seen that the interior area of the pit is covered with corrosion film. Figure 5.27b-d display more details of the surface inside the pit at higher

magnification. A platelet film structure is apparent in Figure 5.27c and Figure 5.27d, which seems to contain significant porosity.

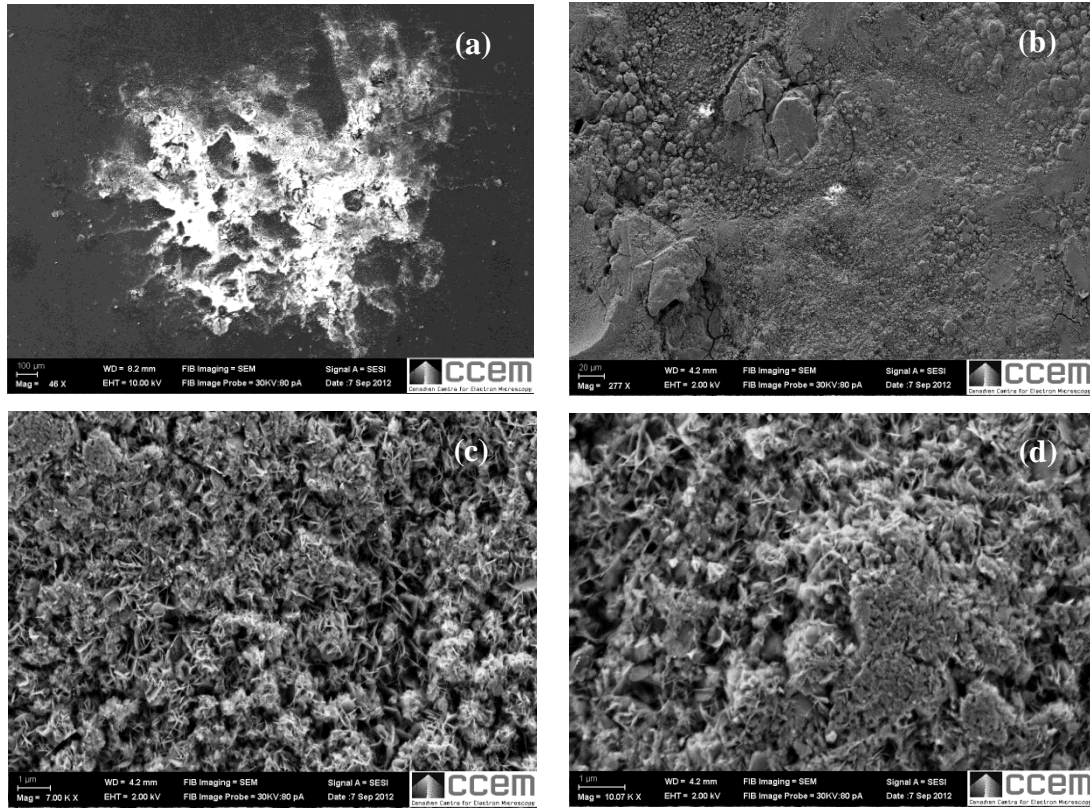


Figure 5.27: SEM images of Mg sample surface aged 24 h in 0.01 M NaCl and potentiostatically polarized at +0.1 V vs. E_b for 0.5 h prior to FIB milling at different magnification (a) a pit (b), (c), and (d) higher magnification of the pit surface showing a film with more porosity.

Figure 5.28a, captured from about the center of the pit, indicates that the surface includes micro-cracks. In order to analyze the composition of the film formed in the pit, EDS spectra were acquired, as shown in Figure 5.28b-d. To maintain accuracy, attention was paid to acquire EDS film spectra from nearby of the same image under similar imaging conditions. The EDS results indicates that the film formed on the pit surface includes only Mg and O, whereas areas adjacent to the micro-cracks include Cl and Fe.

Since Fe impurities are proposed as a pit initiation and growth mechanism [51], the micro-crack in which the Fe EDS signal observed was studied with EDS at higher magnification (Figure 5.29).

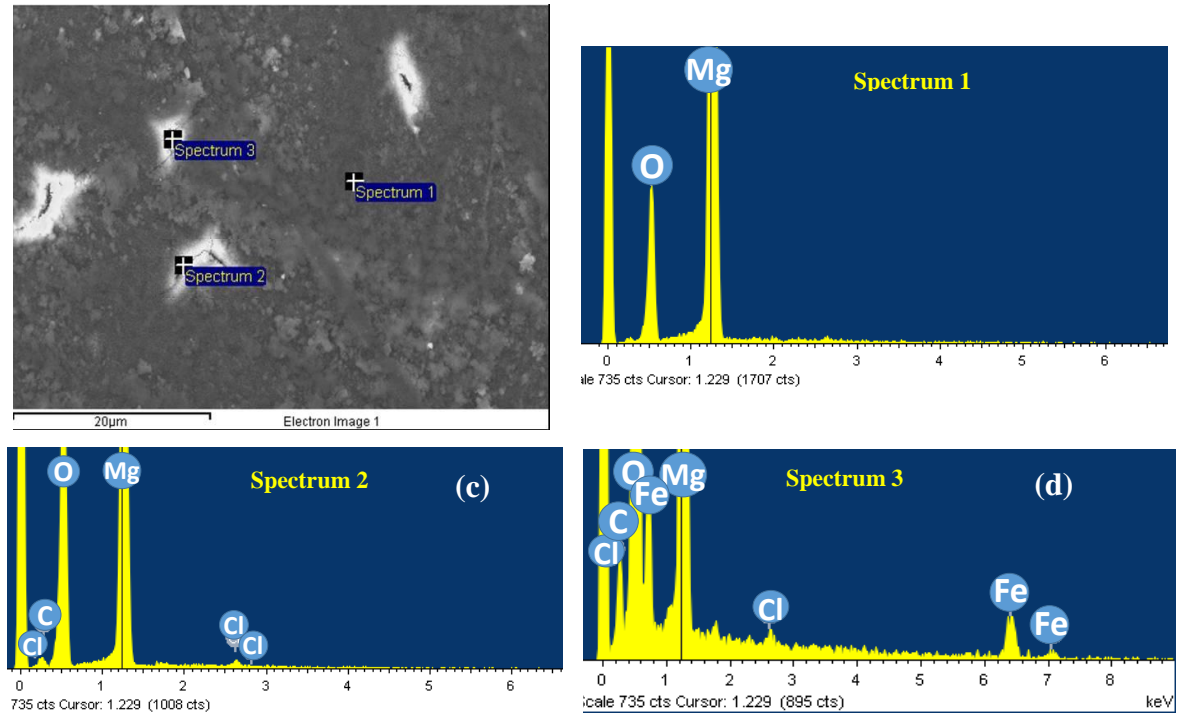


Figure 5.28: (a) SE-SEM images (b), (c), and (d) EDS spectra of Mg sample surface aged 24 h in 0.01 M NaCl and potentiostatically polarized at +0.1 V vs. E_b for 0.5 h showing the presence of Cl and Fe adjacent to cracks inside the pit surface.

The white circles in Figure 5.29a indicate small particles, smaller than 500 nm in diameter observed around the micro-crack. EDS film spectra were acquired from nearby of the same image under similar imaging conditions to maintain maximum the accuracy for comparison of quantification results. The EDS spectra captured from these particles verified the presence of Fe (Figure 5.29c-d). In order to study the composition and

structure of the film formed near the Fe containing particle, a FIB thin foil including this particle was prepared (Figure 5.30).

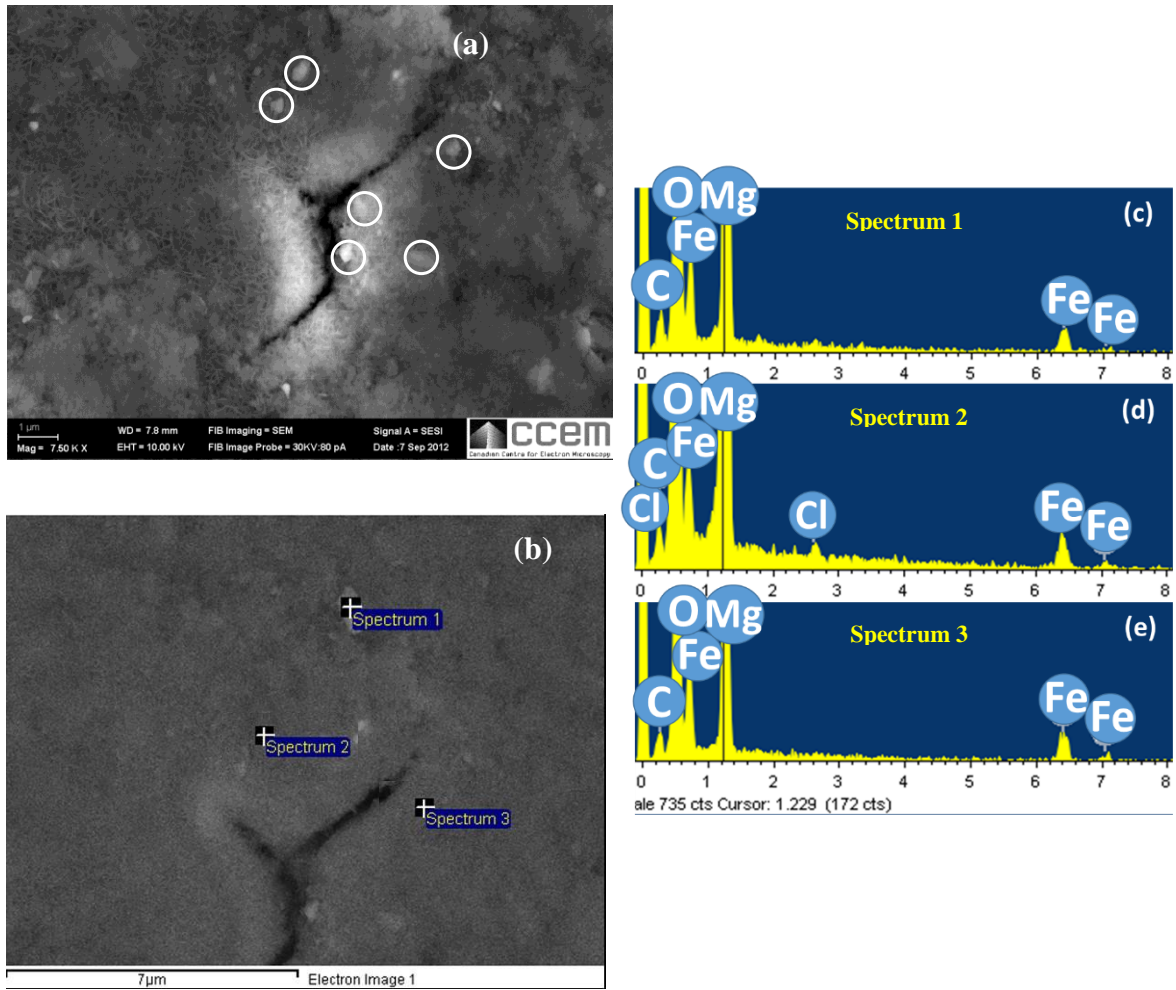


Figure 5.29: (a) SE, (b) BSE-SEM images and (c), (d), and (e) EDS spectra from adjacent to a local cracking inside a pit formed on the Mg sample surface aged 24 h in 0.01 M NaCl and potentiostatically polarized at +0.1 V vs. E_b for 0.5 h; white circles in (a) shows the particles containing Fe.

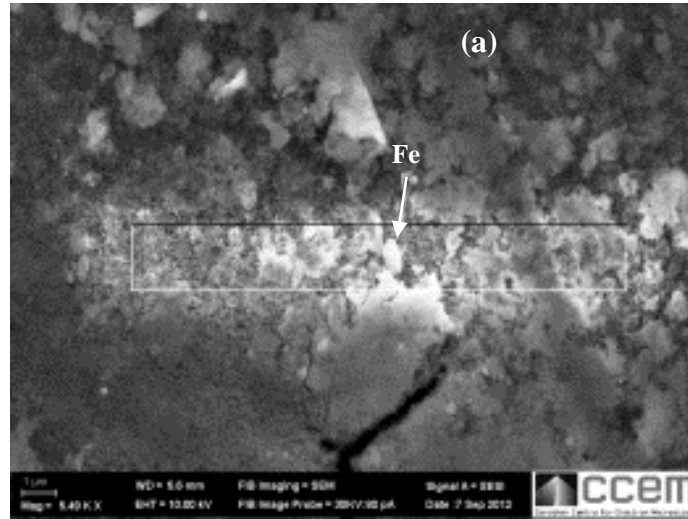


Figure 5.30: SE-SEM image of the selected area from Mg sample surface aged 24 h in 0.01 M NaCl and potentiostatically polarized 0.5 h at +0.1 V vs. E_b for FIB milling.

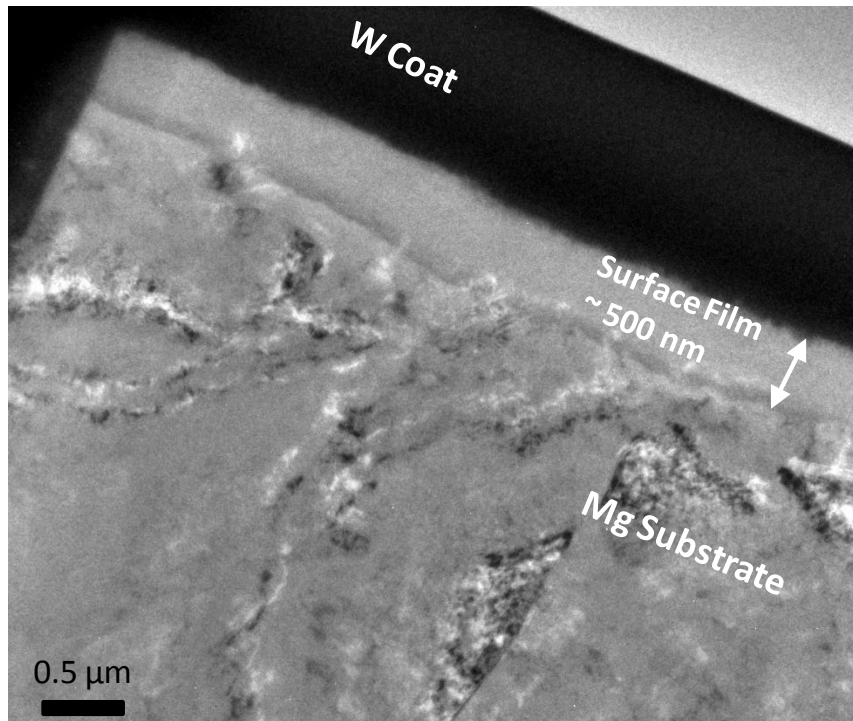


Figure 5.31: TEM bright-field image showing, in cross-section, the non-pitted region film formed on Mg exposed to 0.01 M NaCl at +0.1 V vs. E_b for 0.5 h after 24 h aging at E_{corr} .

Figure 5.31 shows TEM BF-image of the film formed in a un-pitted region. The film appears to be composed of two layers due to the differing contrast adjacent to the Mg/film interface. The total thickness of the film is also about 500 nm.

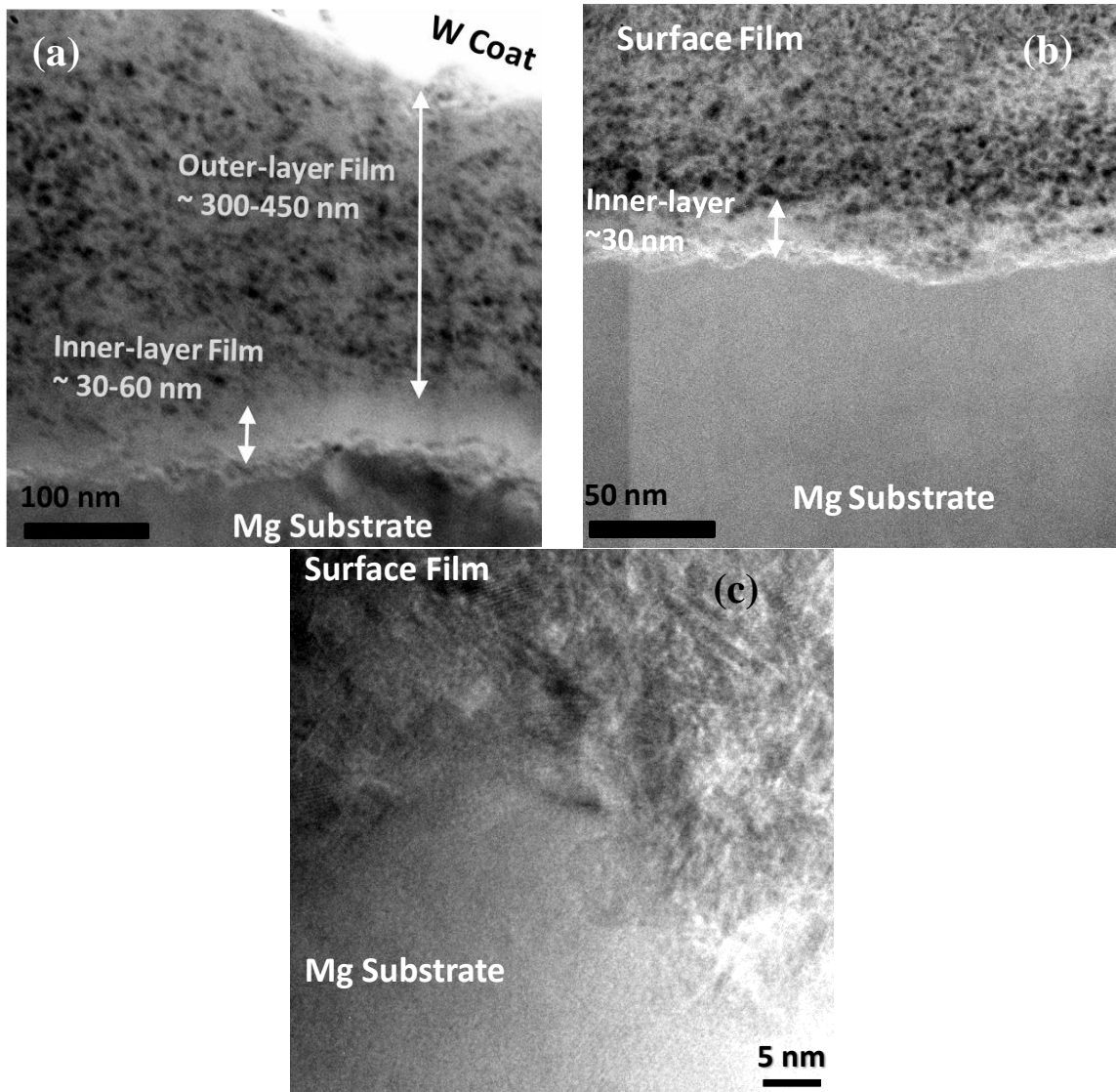


Figure 5.32: (a), (b) STEM DF-images of the non-pitted region formed on Mg exposed to 0.01 M NaCl at +0.1 V vs. E_b for 0.5 h after 24 h aging at E_{corr} , (c) HR-TEM image of Mg/film interface.

DF-STEM images, shown in Figure 5.32a and Figure 5.32b, present the film in more detail. A thinner inner-layer is formed underneath a thicker more porous outer-layer. The outer-layer film consists of numerous dark regions assumed to be porosity. Moreover, the inner-layer exhibits higher contrast compared to the outer-layer. This indicates that the inner-layer has relatively lower porosity than the outer-layer. However,

the inner-layer contains some dark regions (pores) at the areas adjacent to the Mg substrate interface (Figure 5.32b). A HR-TEM BF-image of the interface also confirms the presence of randomly oriented nano-crystals within the inner-layer (Figure 5.32c).

The SAD pattern captured from the inner-layer of the film (Figure 5.33a) confirms that this layer contains a nano-crystalline structure. Also, DF-TEM image (Figure 5.33b), as defined by $\{200\}$ and $\{220\}$ reflections of the cubic MgO structure, indicates that the extent of crystallinity is higher within inner-layer and diminishes across the outer-layer.

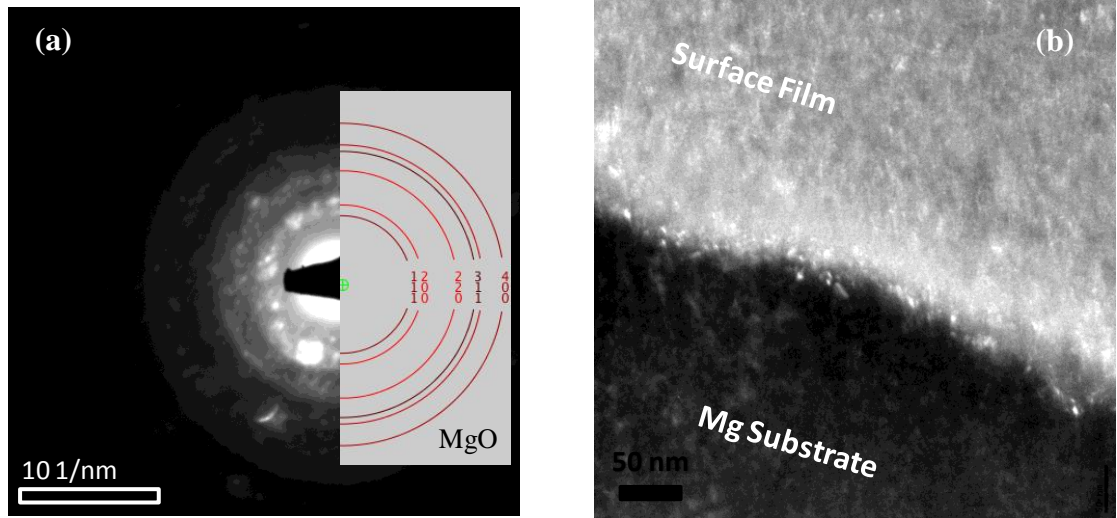


Figure 5.33: (a) SAD pattern acquired from the film/substrate interface formed on Mg exposed to 0.01 M NaCl at +0.1 V vs. E_b for 0.5 h after 24 h aging at E_{corr} ; DF-TEM image of the Mg/film, as defined by the $\{200\}$ and $\{220\}$ reflections of the cubic MgO structure.

In contrast to the un-pitted region, the TEM BF-image of the pit surface (Figure 5.34) shows that a thick needle-like top layer has formed in addition to the two layers just described (Figure 5.31). This third layer increases the total thickness of the film to 1000 nm.

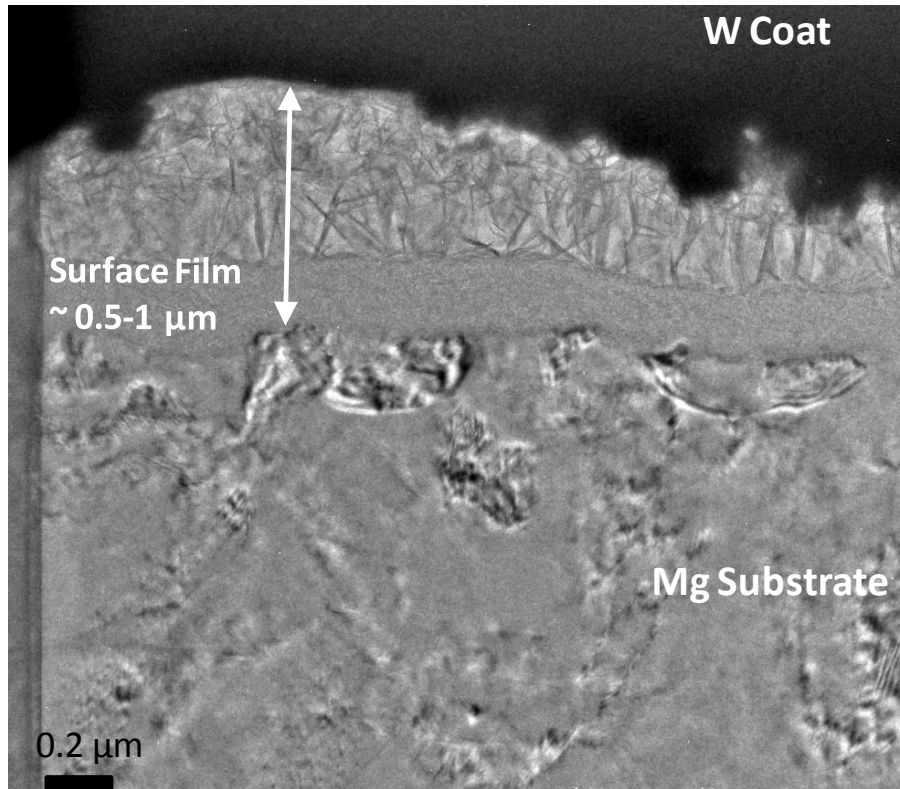


Figure 5.34: TEM BF-image showing, in cross-section, the pitted region formed on the Mg sample exposed to 0.01 M NaCl at +0.1 V vs. E_b for 0.5 h after 24 h aging at E_{corr} .

Figure 5.35a and Figure 5.35b show the pit film in more detail. The needle-like top layer appears to be thicker and more porous compared to the non-pitted region film (Figure 5.32). The large dark regions between the needles verify high porosity in this region. Similar to the non-pitted region film, the outer and inner layers contain dark regions, indicative of porosity. Furthermore, the DF-STEM image of the pit film, Figure 5.35b, shows the presence of a macro-pore within the inner-layer.

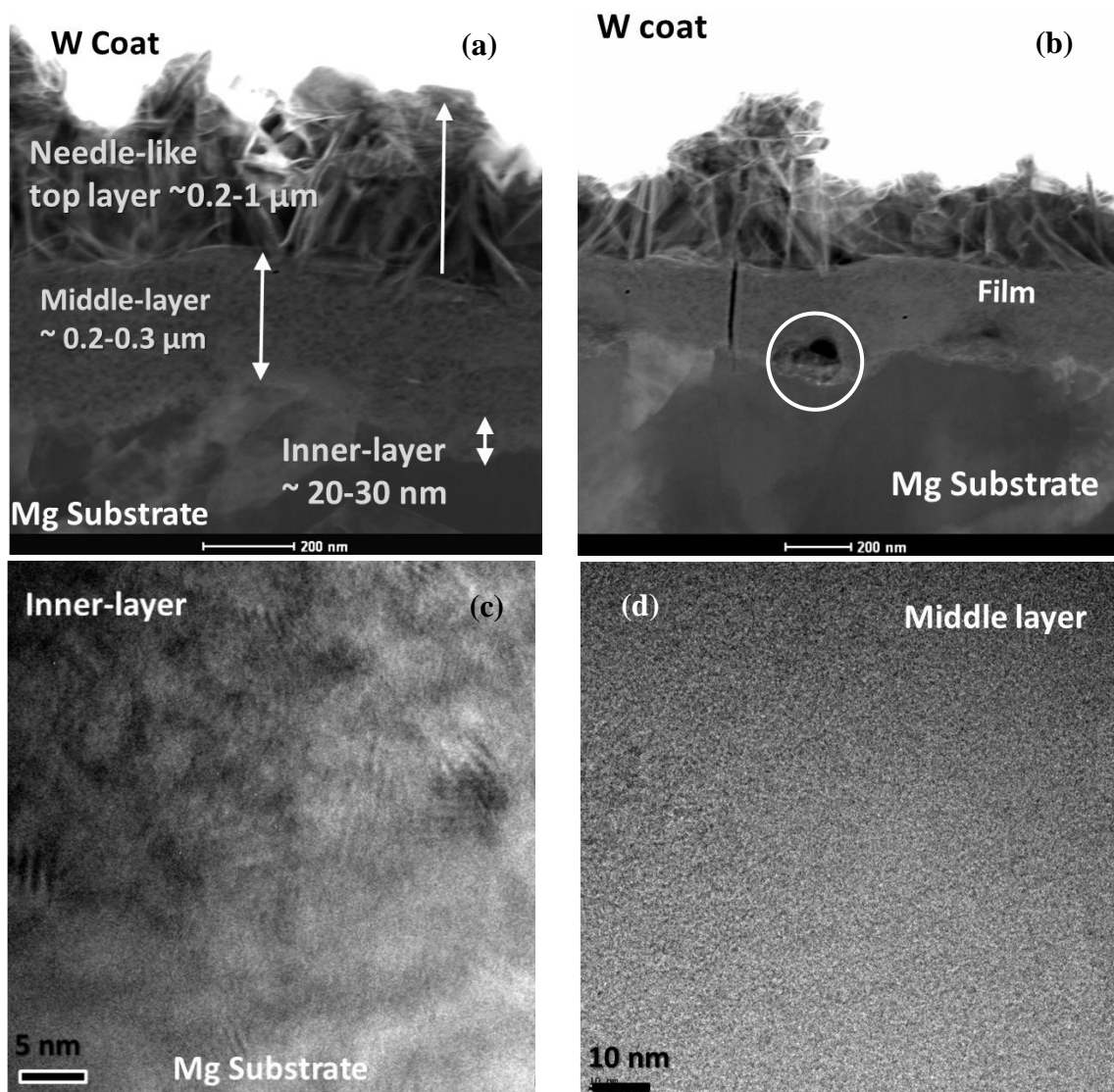


Figure 5.35: (a), (b) STEM DF-images of the pitted region film formed on the Mg sample exposed to 0.01 M NaCl at +0.1 V vs. E_b for 0.5 h after 24 h aging at E_{corr} . (c) HR TEM image of the Mg/film interface, (d) HR TEM image of the middle-layer film. Circle in (b) shows a macro-pore.

Nano-crystals can still be seen in HR TEM image of the Mg/film interface (Figure 5.35c), whereas this crystallinity cannot be observed in areas farther from the Mg/film interface within the middle layer area (Figure 5.35d). This suggests that the middle layer is an amorphous layer.

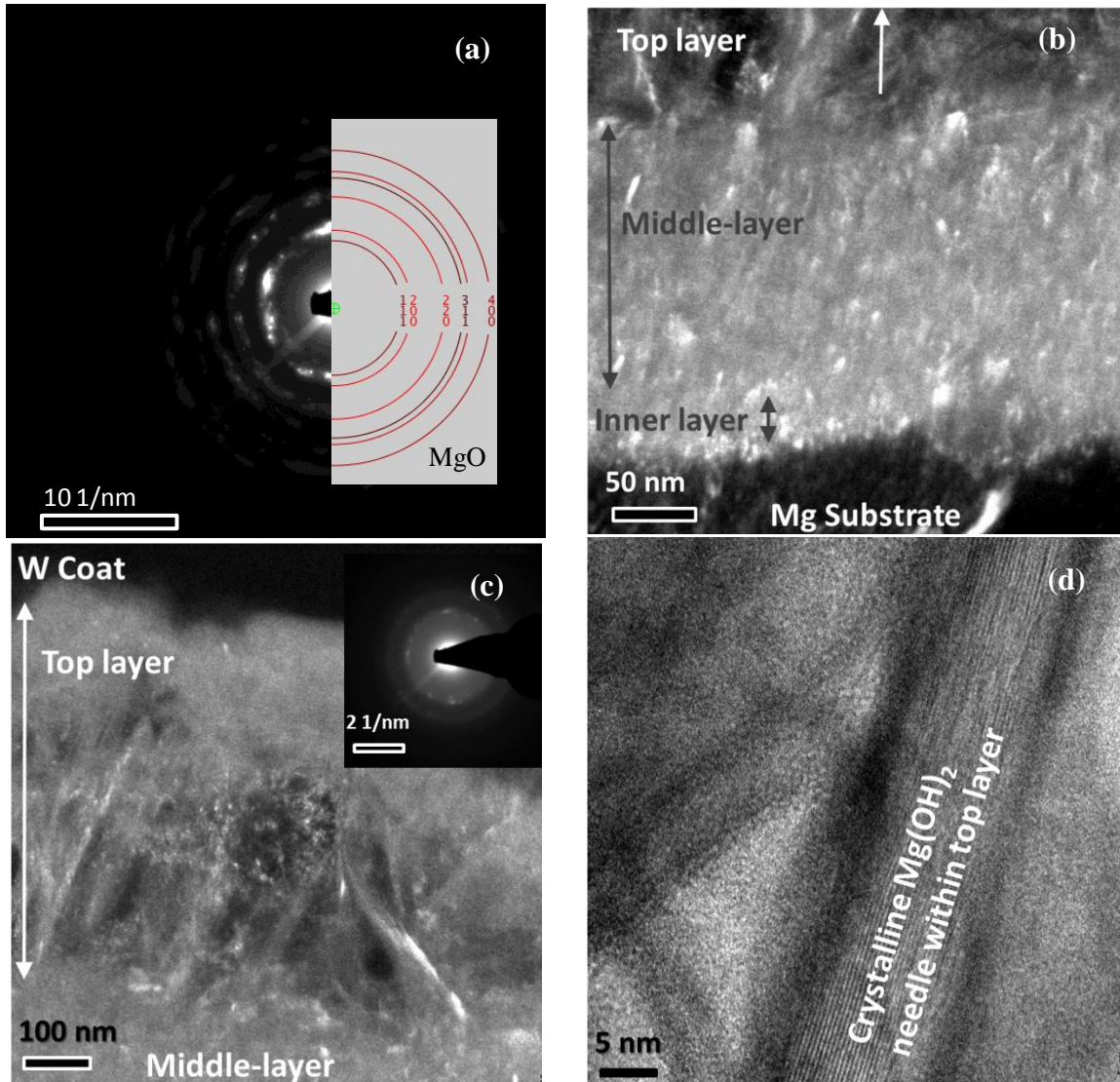


Figure 5.36: (a) SAD pattern acquired from the Mg/film interface of pitted region film formed on Mg exposed to 0.01 M NaCl at +0.1 V vs. E_b for 0.5 h after 24 h aging at E_{corr} ; DF-TEM image of the Mg/film interface, as defined by the {200} and {220} reflections of the cubic MgO structure; (c) DF-TEM image of the top layer as defined by the {111} reflection of the hexagonal $Mg(OH)_2$ structure acquired in the SAD pattern; (d) HR TEM image acquired from of a $Mg(OH)_2$ needle in top layer.

Figure 5.36a presents the SAD diffraction pattern acquired from the middle layer. Accordingly, Figure 5.36b shows the extent of crystallinity, as defined by the {200} and {220} reflections of the cubic MgO structure. It appears that MgO nano-crystals are enriched adjacent to the Mg/film interface; however, the nano-crystals are also distributed

across the middle layer. Moreover, a DF-TEM image recorded using $\{111\}$ reflection of $\text{Mg}(\text{OH})_2$ (Figure 5.36c) confirms the crystallinity of a portion of top layer needles. A HR-BF-TEM image of the top layer also shows this form of crystallinity formed within a needle (Figure 5.36d).

The area selected for EDS analysis is shown in Figure 5.37a. The corresponding SmartMap™ of O, Mg, Cl and W elements across the film area displayed in Figure 5.37b to Figure 5.37e. The intensity of W is highest in the top coat, the intensity of the Mg signal is lowest in the film furthest from the interface and highest in the substrate, and O intensity is highest in the film. Moreover, the Cl map shows a random counts intensity across the film suggesting no significant enrichment. An enriched Cl region can be seen within the W top coat. This is likely due to the collection of background intensity instead the weak Cl intensity. Therefore, this cannot represent Cl distribution across the film. The EDS sum spectrum identified Cl peaks (Figure 5.38), which confirms the presence of Cl within the film. The Cu peak is likely due to the Cu TEM grid, and the Ga peak is due to the Ga^+ ion beam used during FIB sample preparation. The C peak could also be either from surface contamination or MgCO_3 formation. Nevertheless, there does not appear to be any significant enrichment of C within the film (Figure 5.10).

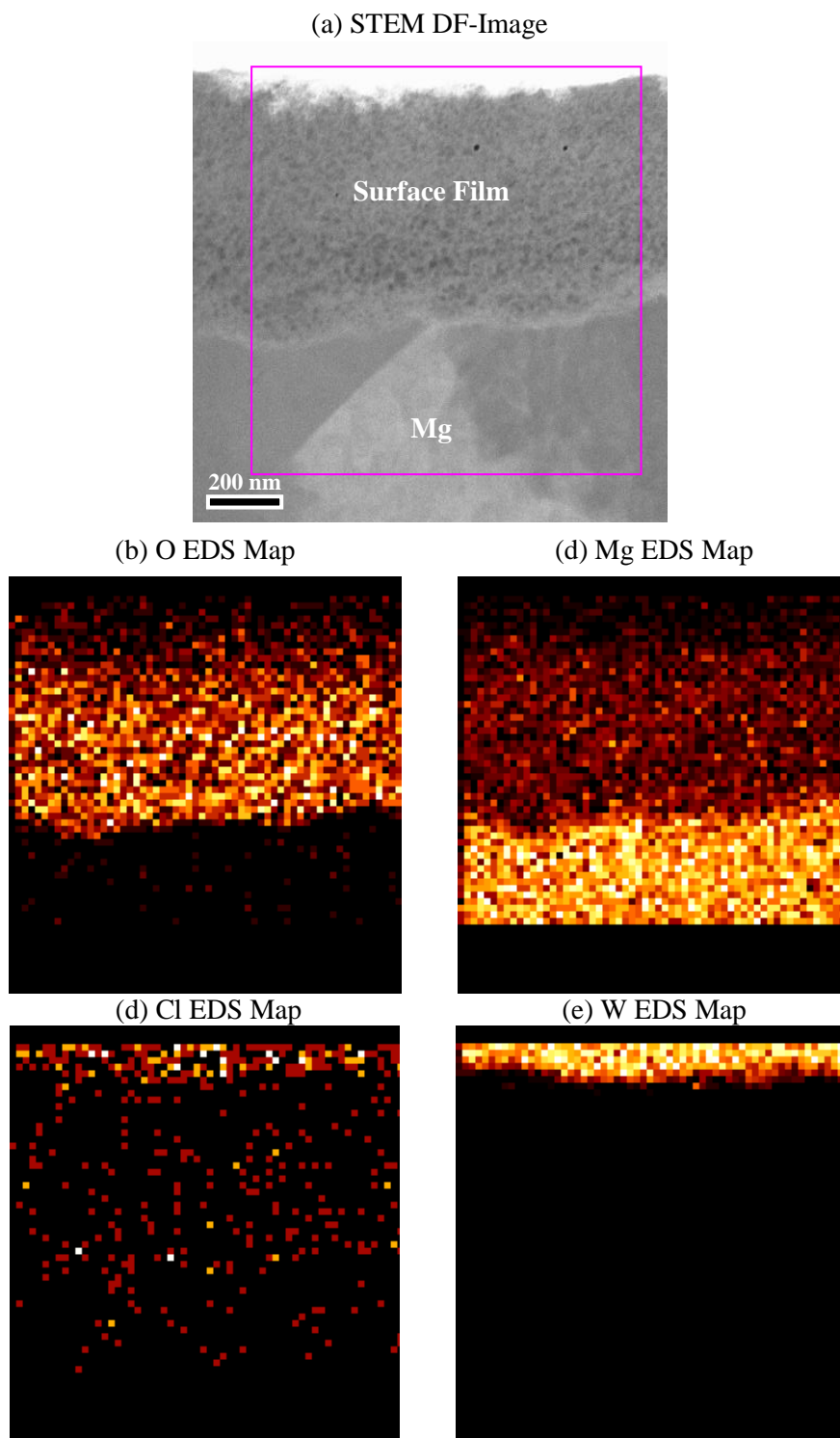


Figure 5.37: (a) DF-STEM image of the non-pitted region film formed on Mg exposed 0.5 h to 0.01 M NaCl at +0.1 V vs. E_b after 24 h aging at E_{corr} , utilized to capture an (b) O EDS map, (c) Mg EDS map, (d) Cl EDS map and (e) W EDS map.

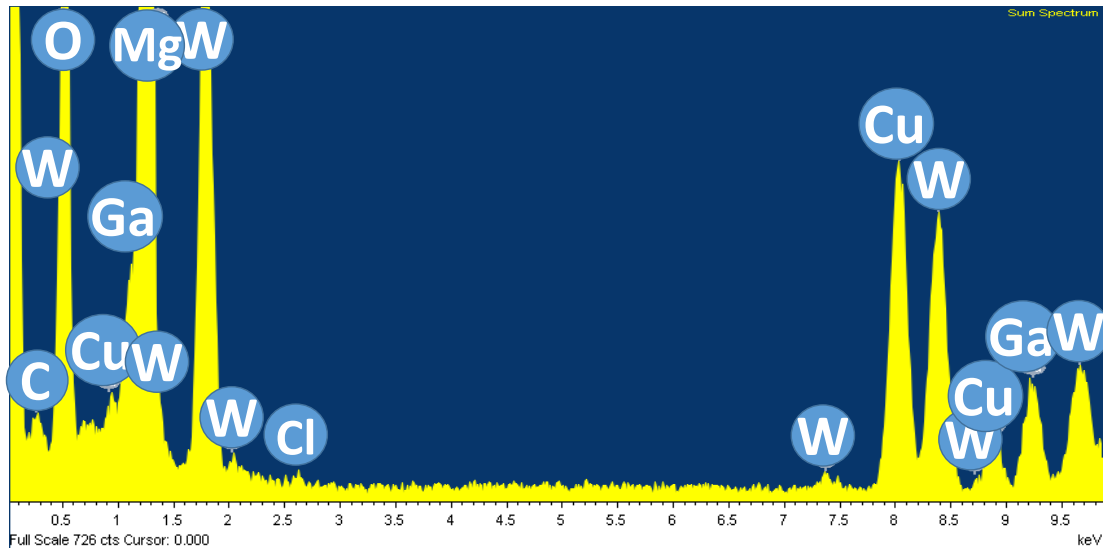


Figure 5.38: EDS sum spectrum of the SmartMapTM characteristic section analyzed in Figure 5.37.

Figure 5.39 displays the average O/Mg atomic ratio calculated for the selected non-pitted region film area using EDS SmartMapTM results (Figure 5.37). The inner-layer, characterized by a brighter contrast adjacent to Mg/film interface (Figure 5.37a), was used to split this area versus the outer-layer in the O/Mg depth profile. The average O/Mg ratio measured in this area acquired a maximum value of 1, which suggests the presence of a MgO-rich layer adjacent to Mg substrate/film positions. Moreover, the outer-layer depth profile exhibits a descending O/Mg atomic ratio of 2.3 to 1.5. Note that attention was paid to consider the thickness variation in the calculation of the quantifications. Therefore, chances of collecting W in this range are short. Except the last data point (nearly 320 nm away from the substrate/film interface), the O/Mg atomic ratio of 2 lies between the error bars as defined by the standard deviation of the data. Therefore, the O/Mg atomic ratios of about 2 suggests a Mg(OH)₂-rich outer layer.

In addition, the sharper transition of the O/Mg atomic ratio from the Mg substrate region to the $\text{Mg}(\text{OH})_2$ -rich outer-layer, suggests that the MgO-rich inner-layer is likely thinner versus the film formed at E_{corr} (Figure 5.26). This is consistent with the inner-layer being more damaged or dissolved at potentials above E_b .

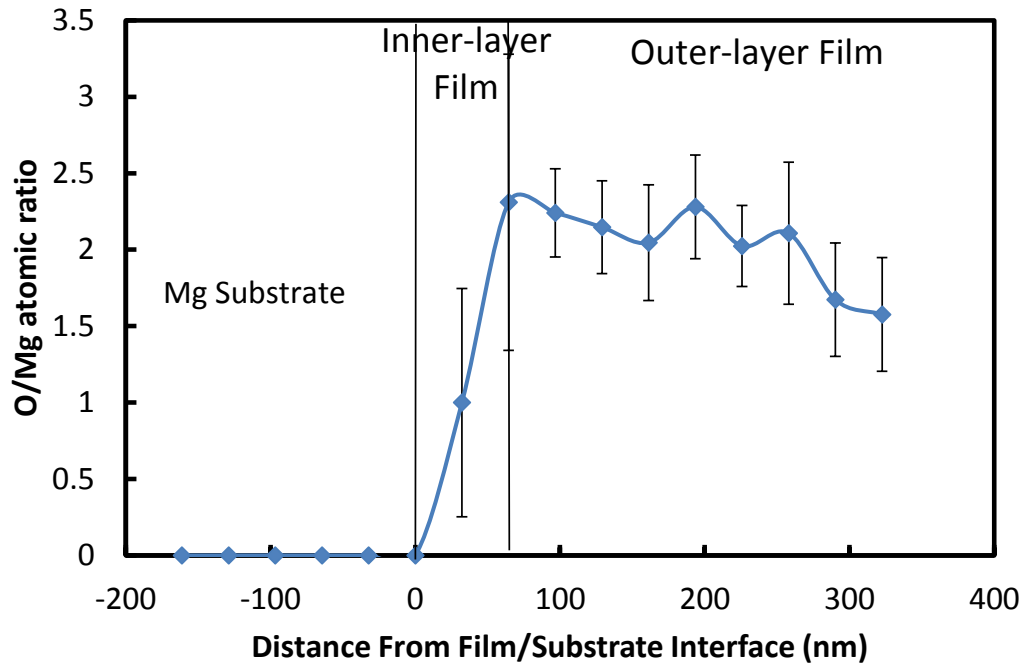


Figure 5.39: O/Mg atomic ratio depth profile through the Mg/non-pitted region film interface formed on Mg after 0.5 h exposure in 0.01 M NaCl at +0.1 V vs. E_b .

A preliminary attempt to acquire a point scan from a characteristic section of the film inside a pit containing a Fe-rich particle (Figure 5.29 and Figure 5.30), is shown in Figure 5.40a. The EDS quantification of the dashed circle, Table 5.3, confirms that the impurity contains Fe. The EDS spectrum shows the presence of other elements such as W, Ga, Cu, and O. W is likely from the W deposited coat prior to FIB milling, Ga due to Ga^+ ion beam used during FIB, Cu from the Cu TEM grid, and O is indicative of oxide

form of the identified elements. However, a more accurate chemical surface analysis such as XPS or AES is required to identify these oxides more precisely.

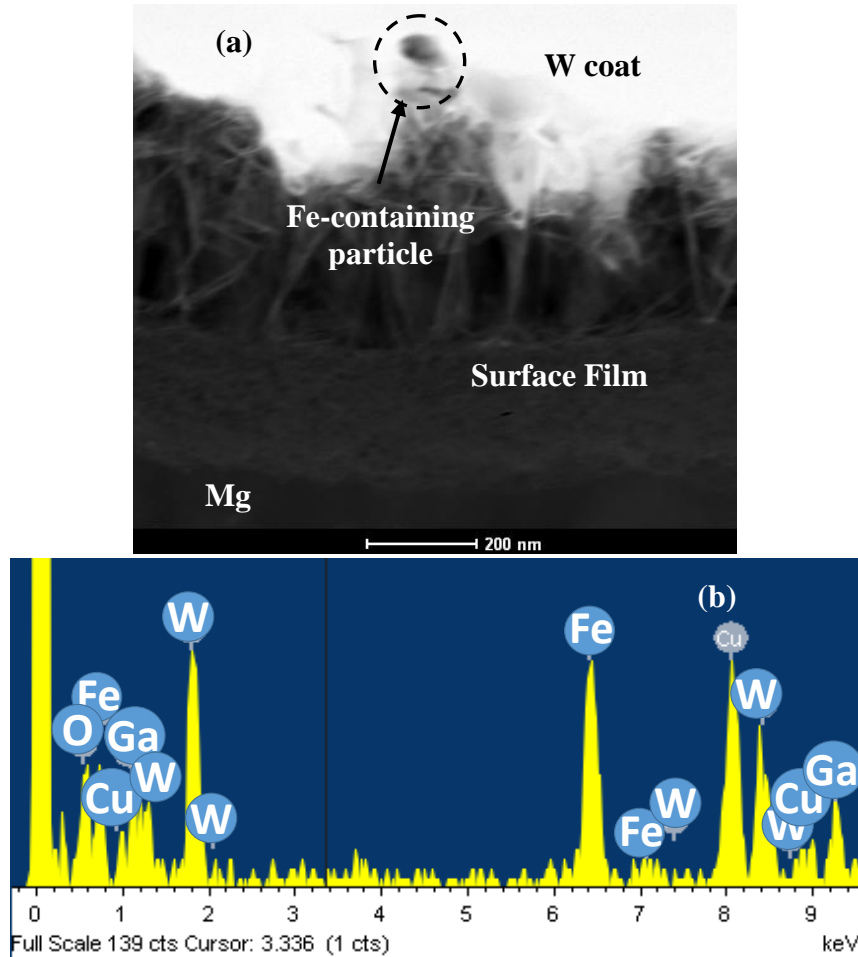


Figure 5.40: (a) DF-STEM image of the pitted region film formed on Mg after 0.5 h exposure in 0.01 M NaCl at +0.1 V vs. E_b , after 24 h aging at E_{corr} , utilized to capture (b) EDS spectra from the Fe containing particle found in Figure 5.30.

Table 5.3: EDS elemental quantification of spectra recorded in Figure 5.40.

	O K	Fe K	Cu K	Ga K	W L
Fe containing particle	39*	18*	21*	7*	15*

*An error of $\pm 2-5$ % is likely [114], [115].

The DF-STEM image, shown in Figure 5.41a, indicates the area selected for EDS analysis of the pit film. This area also includes the previously identified Fe-rich impurity

particle (Figure 5.40a). The corresponding SmartMap™ of O, Mg, Cl, W, and Fe across the film is also displayed in Figure 5.41b to Figure 5.41f. As expected, the intensity of W is highest in the top coat; the intensity of the Mg signal is lowest in the needle-like top layer. Moreover, O intensity, which is highest in the middle and inner layers, appears to diminish in the top layer. This is consistent with formation of highly porous needles on top of the film in these areas. The W top coat exhibits increased Cl counts. As stated earlier, the Cl map is likely a random counts intensity across the film suggesting no significant enrichment. This is likely due to collection of background intensity instead the weak Cl intensity. Therefore, this cannot represent Cl distribution across the film. However, observation of the Cl characteristic peaks in the EDS sum spectrum (Figure 5.42) confirms the presence of Cl within the film. Additionally, an area is identified in the Fe SmartMap™ in which the intensity of the Fe is highest. This maximum Fe intensity area in the cross-section is consistent with the plan view SEM images, which shows the Fe-rich impurity particle (Figure 5.30). This site was from the plan view was the location chosen to ion mill the cross-section sample from the middle of the pit corrosion film.

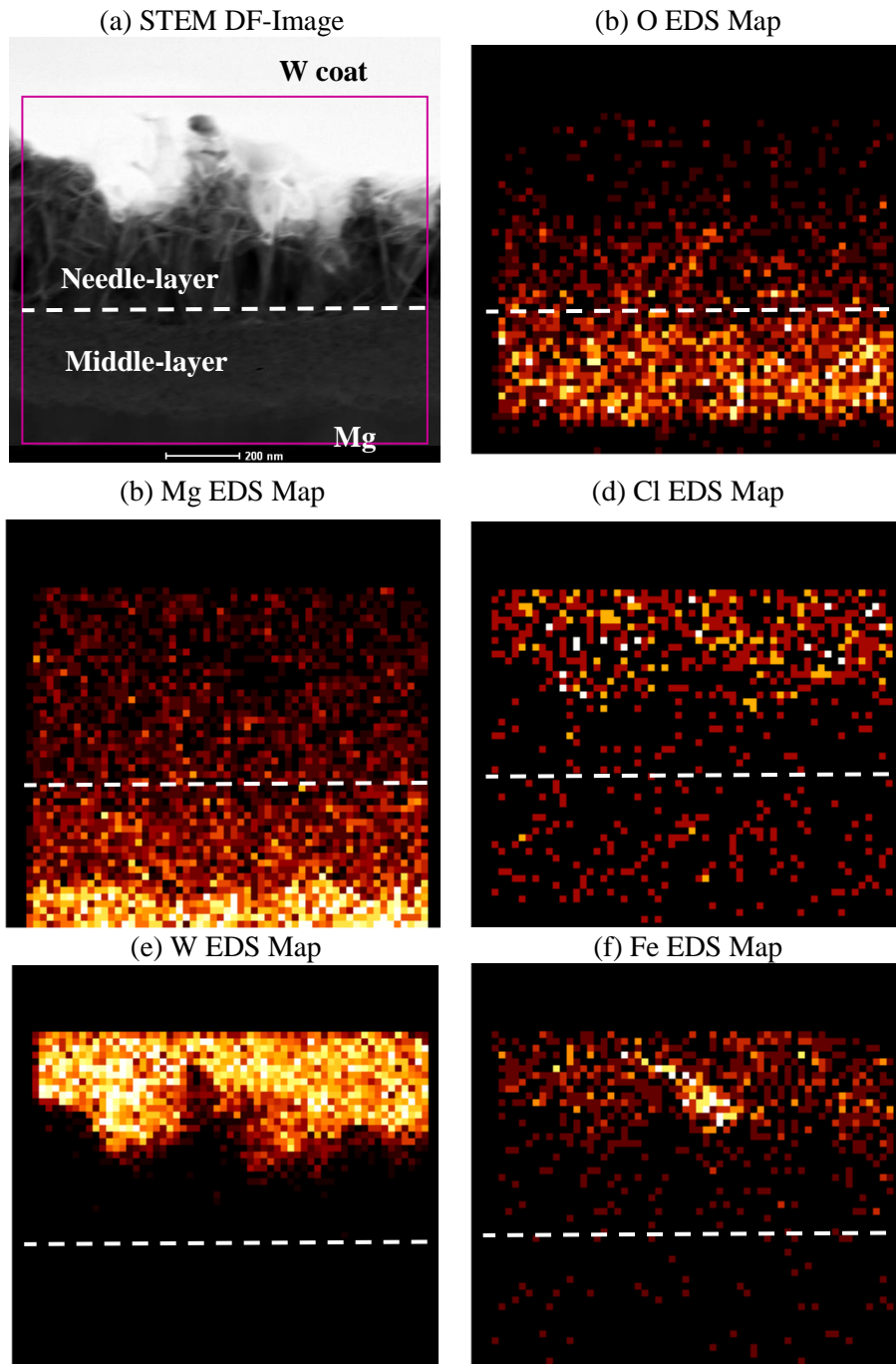


Figure 5.41: (a) STEM DF-image of the pitted region film containing Fe, formed on Mg exposed 0.5 h to 0.01 M NaCl at +0.1 V vs. E_b after 24 h aging at E_{corr} , utilized to capture an (b) O EDS map, (c) Mg EDS map, (d) Cl EDS map, (e) W EDS map and (e) Fe EDS map.

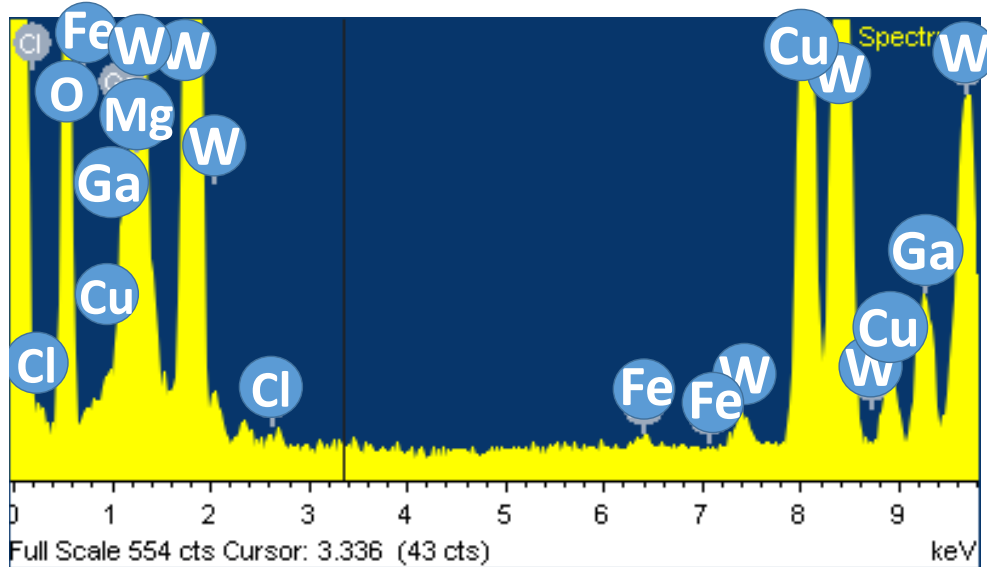


Figure 5.42: EDS sum spectrum of the SmartMap™ characteristic section analyzed in Figure 5.41.

The average depth profile of the O/Mg atomic ratio across the film atop the centre of a pit is shown in Figure 5.43. The depth profile appears to exhibit a similar O/Mg atomic ratio gradient to that observed for the film on the non-pitted region (Figure 5.39). The positions adjacent to the Mg/film interface acquired a ratio of about 1, which is consistent with the formation of a thin MgO-rich inner-layer. Nonetheless, the positions with the ratio of about 2 are consistent with the formation of a Mg(OH)₂-rich outer-layer formed away from the interface. Similar to SAD results (Figure 5.36c), this confirms that the highly porous needle-like top layer is Mg(OH)₂-rich.

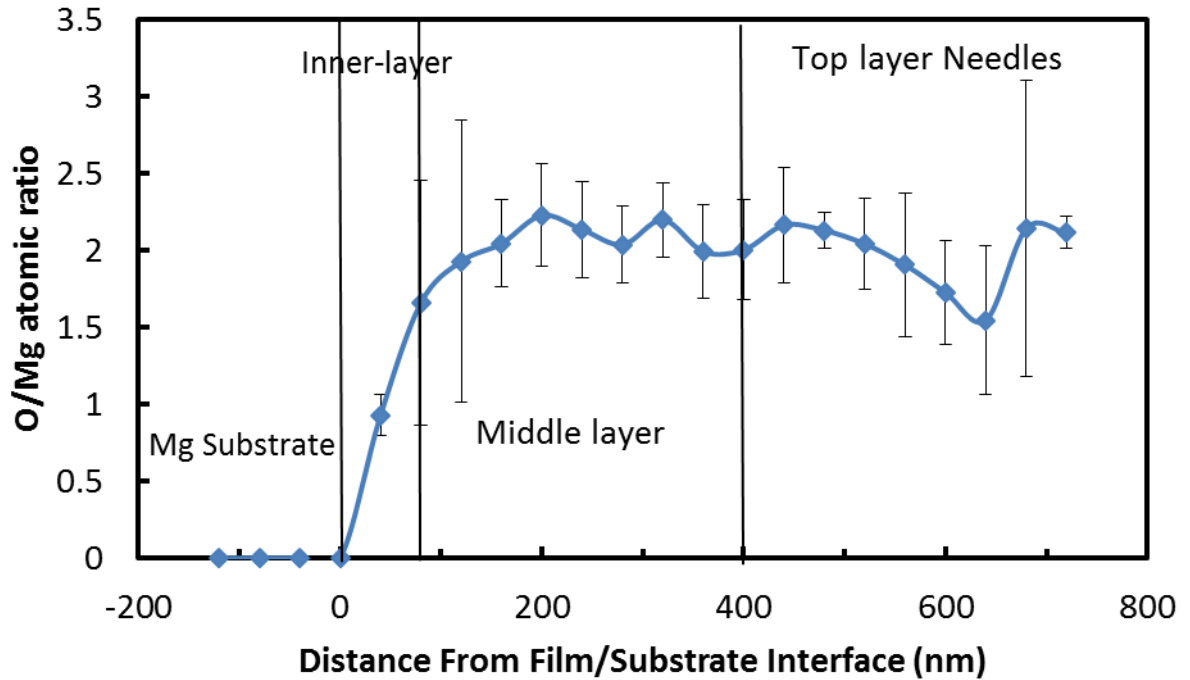


Figure 5.43: O/Mg atomic ratio depth profile through the Mg/pitted region film interface formed on Mg after 0.5 h exposure in 0.01 M NaCl at +0.1 V vs. E_b .

In order to achieve a Cl depth profile inside the pitted region film, a similar EDS spectra integration of the characteristic section (Figure 5.41a) to that used for the O/Mg atomic ratio was carried out to plot the gradient of Cl and the results are shown in Figure 5.44. The diamond points shows average value of the Cl at. % recorded at given distance from the Mg/film interface. It can be seen that Cl exists everywhere across the film even in the inner layer area. At the beginning of the immersion in 0.01 M NaCl, Cl is expected to incorporate only on top of the Mg film. However, the porous nature of the Mg film during prolonged exposures can provide easier ingress of Cl^- to the film, and therefore, the Cl gradient is expected to become uniform across the film.

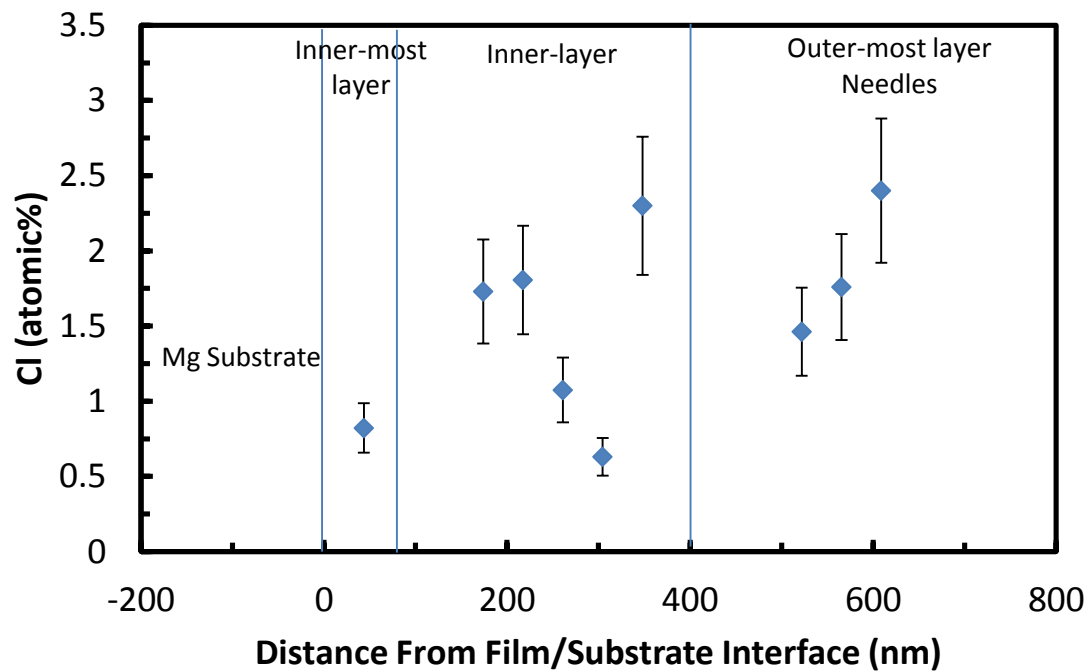


Figure 5.44: Cl at. % depth profile through the interface region between the Mg/pitted region film interface formed on Mg after 0.5 h exposure in 0.01 M NaCl at +0.1 V vs. E_b .

5.3. 1 M NaOH

Figure 5.45 shows the E_{corr} variation with time in 2 separate experiments, measured immediately upon exposure in 1 M NaOH maintained at room temperature for 48 h. Although both transients consist of a general drift towards significantly more positive potentials, they show several time intervals of different rates of increase, as well as several significant potential drops (fluctuations). The fine features, namely the maximum potential attained, the fluctuation amplitude and the fluctuation frequency are not reproducible. Despite not being reproducible, the larger of the potential drops in either transient tend to occur from the highest value to almost the initial value. Transient 1 appears to attain a steady-state value of about $-0.64 \text{ V}_{\text{SCE}}$, which is about 1.15 V more positive than the initial potential.

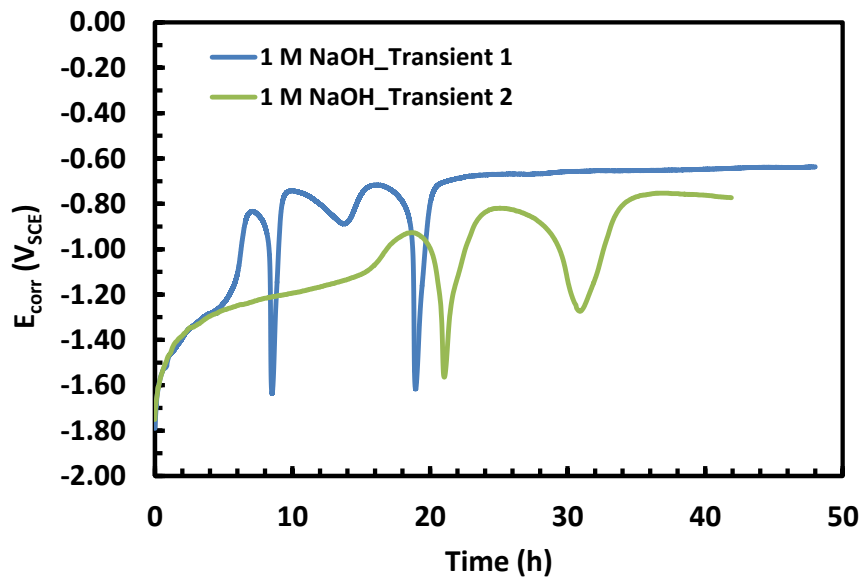


Figure 5.45: E_{corr} transients of 4N Mg exposed to 1 M NaOH for 48 h.

To compare the E_{corr} behaviour exhibited by Mg in 1 M NaOH alkaline solution compared to a near-neutral aqueous solutions, 2 samples were aged one in 0.01 M Na_2SO_4 , and the other in 0.01 M $\text{Na}_2\text{SO}_4 + 1 \text{ M NaOH}$ solutions. Figure 5.46 superimposes the two E_{corr} curves during aging for 24 h in both solutions. The E_{corr} in 0.01 M Na_2SO_4 solution is immediately stabilized at $-1.60 \text{ V}_{\text{SCE}}$ after approximately 1 h of exposure, whereas in 0.01 M $\text{Na}_2\text{SO}_4 + 1 \text{ M NaOH}$ the E_{corr} (similar to 1 M NaOH) exhibits a rising trend towards significantly more positive potentials accompanied with considerable potential drops. Interestingly, the lowest value for two of the potential drops coincides with the steady potential observed in 0.01 M Na_2SO_4 . To ensure reproducibility, all E_{corr} measurements were repeated. Repeated tests showed that the E_{corr} transients are in a $\pm 5 \text{ mV}$ reading range.

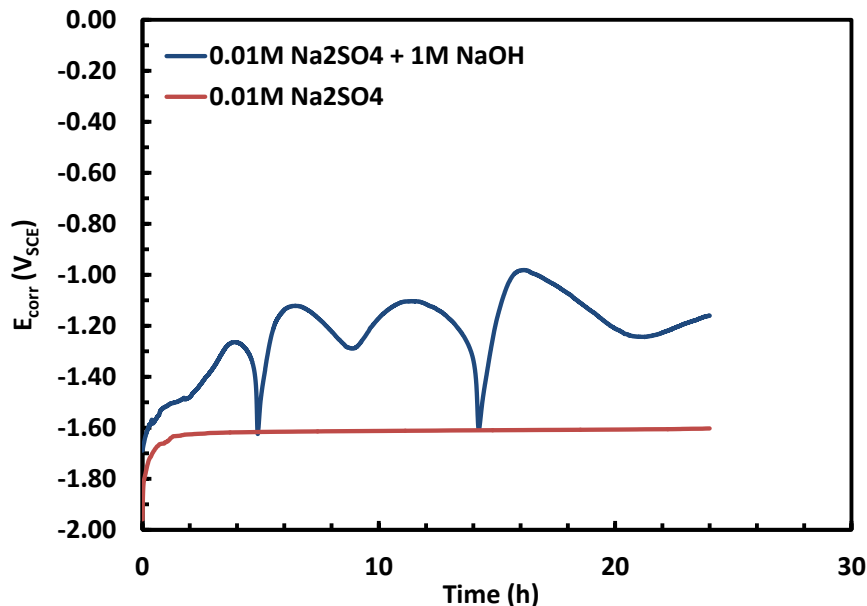


Figure 5.46: E_{corr} transients of 4N Mg, exposed to 0.1 M Na_2SO_4 and 0.1 M $\text{Na}_2\text{SO}_4 + 1 \text{ M NaOH}$ solution for 24 h.

The polarization curve of Mg measured after aging for 24 h in 1 M NaOH is displayed in Figure 5.47. No breakdown is observed during anodic polarization and Mg

shows a limiting current density of $46.8 \mu\text{A}/\text{cm}^2$. E_{corr} is ennobled to a value of $-0.94 \text{ V}_{\text{SCE}}$. In addition, $0.01 \text{ M Na}_2\text{SO}_4$ was also added to the 1 M NaOH solution and the potentiodynamic polarization experiment was measured after 24 h aging for consistency. The polarization behaviour of Mg after 24 h aging in $1 \text{ M NaOH} + 0.01 \text{ M Na}_2\text{SO}_4$ and $0.01 \text{ M Na}_2\text{SO}_4$ solutions are compared in the potentiodynamic graph shown in Figure 5.48. Moreover, in order to ensure their reproducibility, all polarization measurements were repeated. The repeated tests were found to be consistent and no significant variation in the potentiodynamic curves were observed.

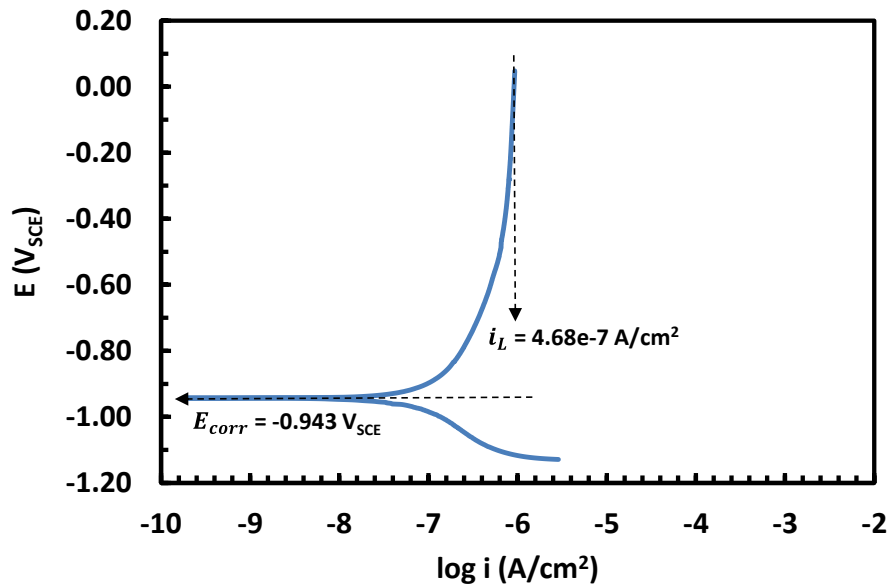


Figure 5.47: Potentiodynamic polarization curve of 4N Mg, after aging 48 h at E_{corr} in 1 M NaOH

Values of electrochemical kinetic parameters are calculated and listed in Table 5.4. Qualitatively speaking, the significantly improved corrosion resistance exhibited by Mg in the alkaline solution is demonstrated by the substantial reduction in anodic kinetics, as well as a mild reduction in the cathodic kinetics. The i_{corr} , estimated by the

cathodic Tafel extrapolation method, is $3 \mu\text{A}/\text{cm}^2$ in the $0.01 \text{ M Na}_2\text{SO}_4$ solution, whereas it is $0.0137 \mu\text{A}/\text{cm}^2$ in the $0.01 \text{ M Na}_2\text{SO}_4 + 1 \text{ M NaOH}$ solution.

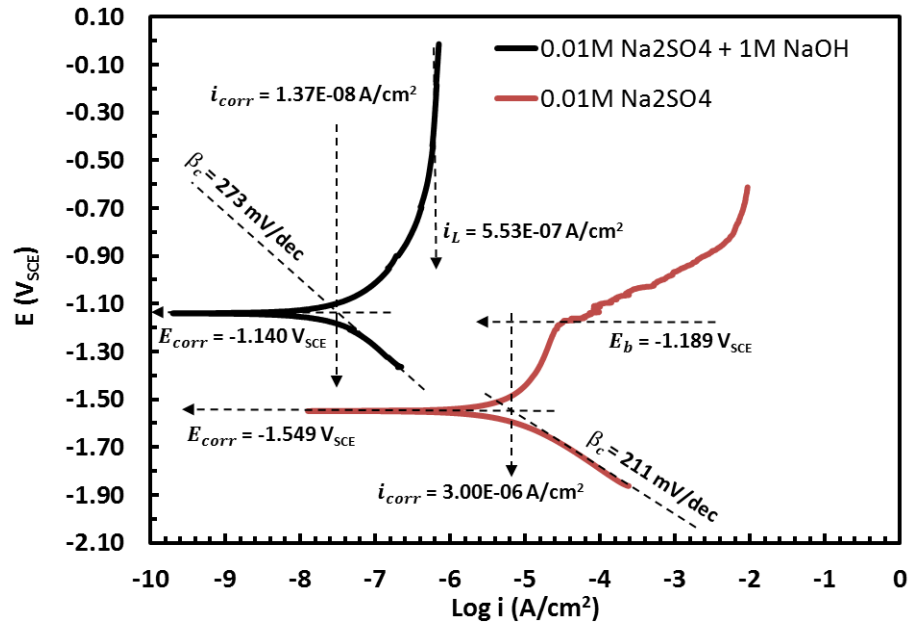


Figure 5.48: Potentiodynamic polarization curves of 4N Mg, after aging 24 h at E_{corr} in $1 \text{ M Na}_2\text{SO}_4$ and $1 \text{ M Na}_2\text{SO}_4 + 1 \text{ M NaOH}$ solution.

Table 5.4: Electrochemical kinetic parameters extracted from potentiodynamic polarization curves recorded for Mg in 1 M NaOH and $0.01 \text{ M Na}_2\text{SO}_4$ solutions after 24 h aging

Solution	i_{corr} (A/cm^2)	E_{corr} (V_{SCE})	β_{C} (mV/dec)	E_{b} (V_{SCE})
$0.01 \text{ M Na}_2\text{SO}_4 + 1 \text{ M NaOH}$	$1.37\text{E}-08$	-1.140	273	N/A
$0.01 \text{ M Na}_2\text{SO}_4$	$3.00\text{E}-06$	-1.549	211	-1.189

Figure 5.49a-c show the SE-SEM images of the Mg surface film formed after exposure to the 1 M NaOH test solution for 48 h at E_{corr} . The grain boundaries are clearly visible under relatively low magnification (Figure 5.49a), which indicates that the film formed is very thin. The surface is also randomly decorated with nodules. Moreover, a striation-like feature originating from the center is also apparent within each grain. A

more detailed image of the nodule reveals that the nodules grew on top of the surface (Figure 5.49b) and were cracked. Interestingly, as marked with a dashed circle in Figure 5.49b, several platelets have formed near the cracked nodule.

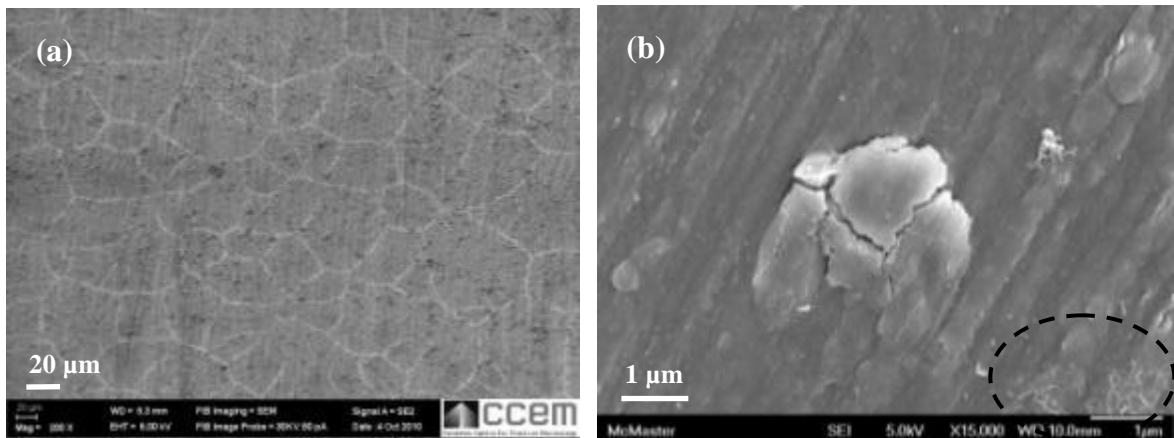


Figure 5.49: SEM images of the film, in plan view, formed on Mg after exposure to 1 M NaOH for 48 h, (a) low magnification (b) and high magnification.

Figure 5.50 shows a TEM bright-field image of a FIB thinned foil containing the corrosion film and a nodule in cross-section. The film appears to be continuous, compact and adherent. At this magnification the general features of the film do not indicate a contrast difference at the Mg/film interface along the film adjacent to the nodule. As shown by the arrow, the nodule is located at the middle of the window and a continuous film covers the Mg substrate on either side of the nodule.

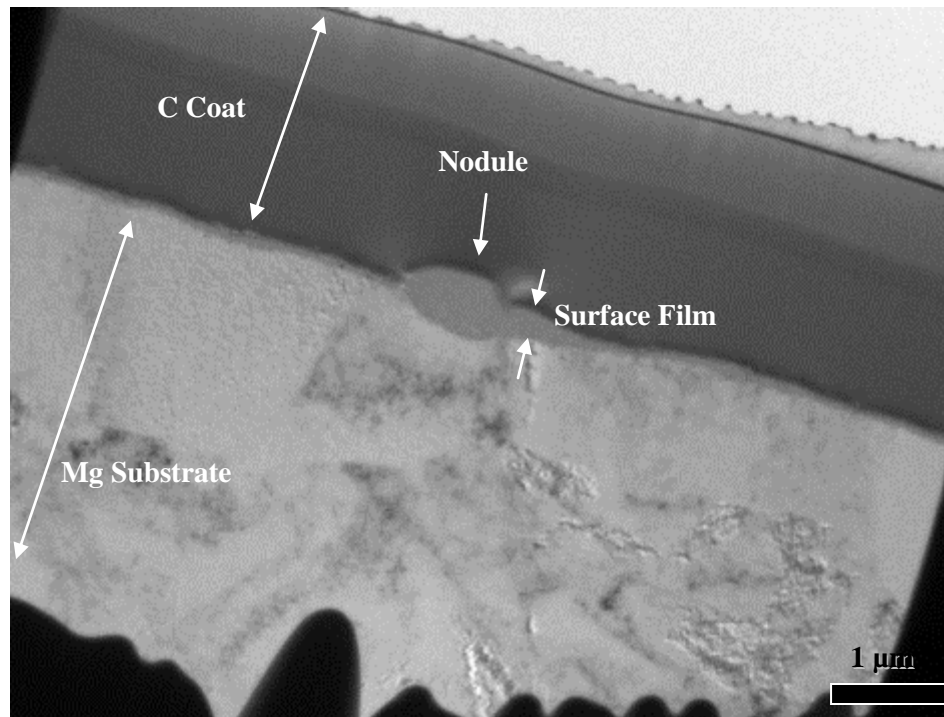


Figure 5.50: BF-TEM image showing, in cross-section, the film on the Mg sample formed by exposure to 1 M NaOH at E_{corr} for 48 h.

Figure 5.51a and Figure 5.51b show BF-TEM cross-section images of the Mg/film interface without (Figure 5.51a) and with (Figure 5.51b) a nodule present. Similarly, Figure 5.51c and Figure 5.51d show DF-STEM images of the film without and with nodule, respectively. As shown in Figure 5.51b and Figure 5.51d, some beam induced holes are formed within the film.

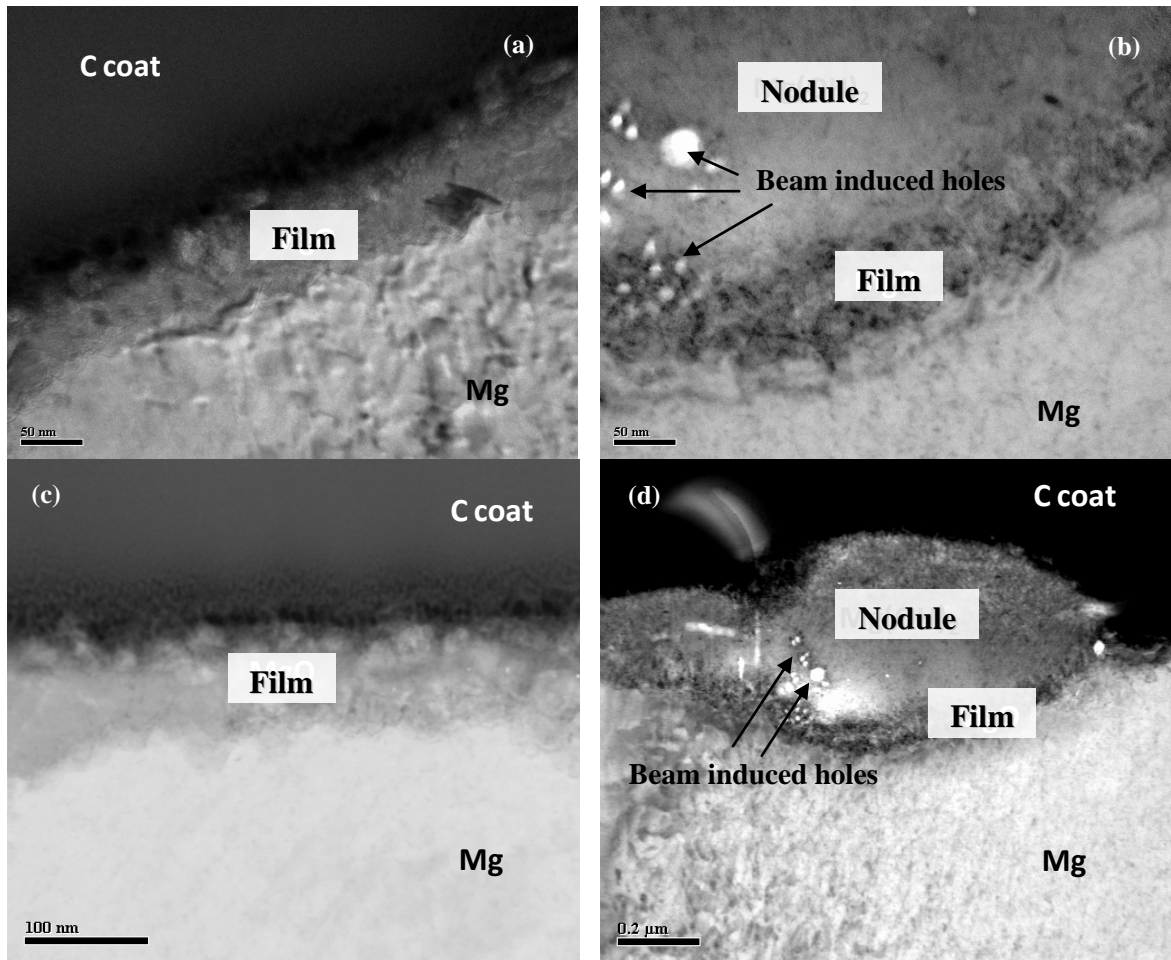


Figure 5.51: BF-TEM image of film/substrate interface (a) without nodule, and (b) with nodule present, and STEM DF-image of (c) the interface without nodule and (d) with nodule present on the film formed after exposure in 1 M NaOH for 48 h.

The thin film formed on the Mg substrate without a nodule present appears to be continuous, dense and adherent. In contrast, the thin inner layer present underneath a nodule appears to be porous and poorly bonded to the Mg substrate. Despite the obvious difference in appearance, the thickness of the inner-layer with and without a nodule present is similar, ranging from about 50 nm to 150 nm. In contrast to the thin inner layer on which it resides, the thicker nodule appears to be continuous and dense. The maximum thickness of the nodule is about 500 nm.

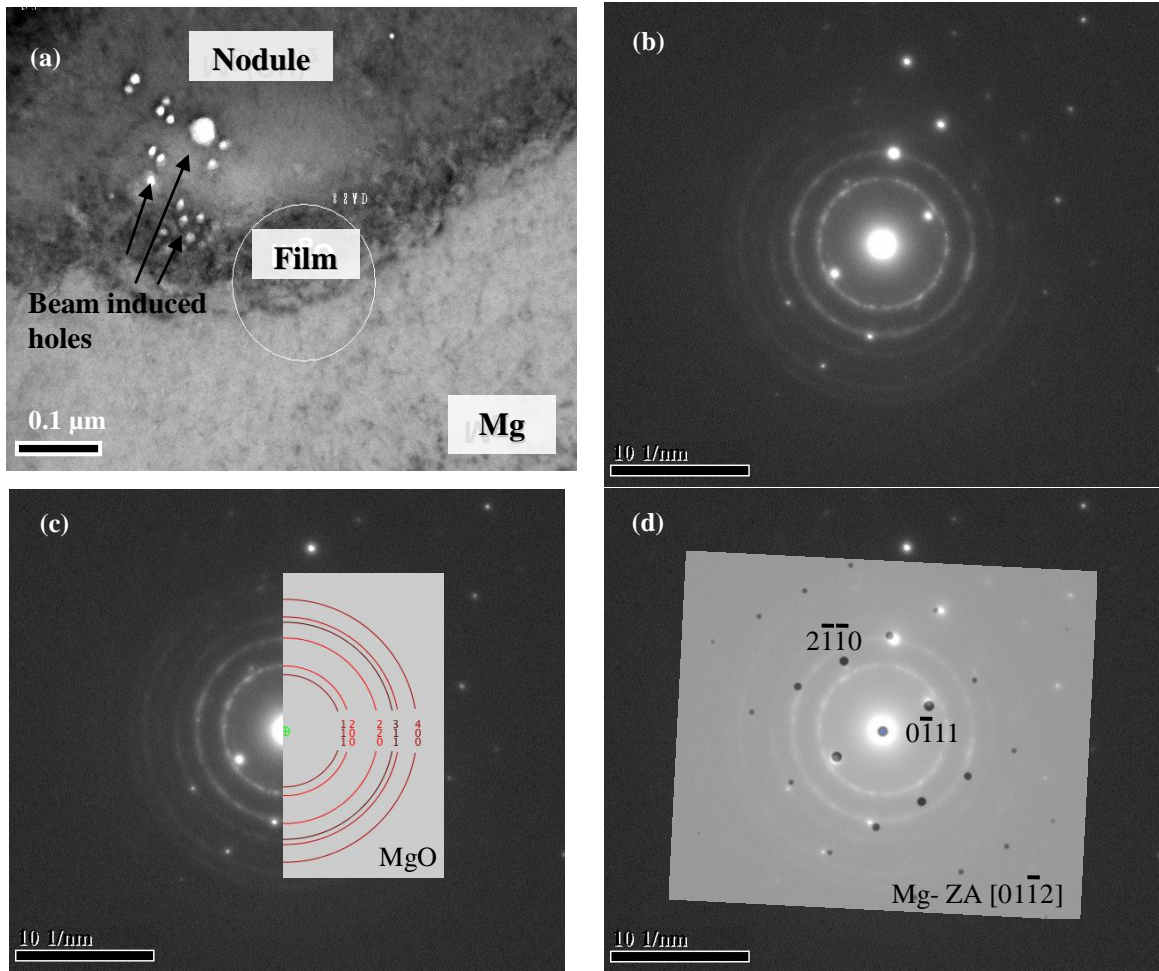


Figure 5.52: SAD pattern acquired from the film/substrate interface directly underneath a nodule.

The SAD pattern acquisition area is presented in the DF-STEM image shown in Figure 5.52a. The smallest aperture size was inserted to select an area of about 150 nm centered on the inner layer. The aperture size and placement was such that the substrate, inner layer and nodule were all included in the measurement. The SAD pattern acquired is shown in Figure 5.52b. The pattern consists of both rings and spots. Figure 5.52d compares the acquired spot pattern with a simulated one determined for single crystal Mg. The simulation was carried out using the JEMS software package and published crystallographic data for Mg [114]. The good agreement indicates that the spot pattern

corresponds to the Mg substrate. Figure 5.52c compares the acquired ring pattern with a simulated one for polycrystalline MgO (using published crystallographic information [111]). The good agreement indicates that the ring pattern corresponds to polycrystalline MgO. Note that $\{111\}$ reflection is only a spot, which is consistent with Mg substrate. It does not show a ring form, and therefore, MgO 111 reflection is missing. Crystalline $\text{Mg}(\text{OH})_2$ can be ruled out since it has a strong reflection at 4.77 \AA (001), which is significantly larger than the first reflections of MgO or Mg [115].

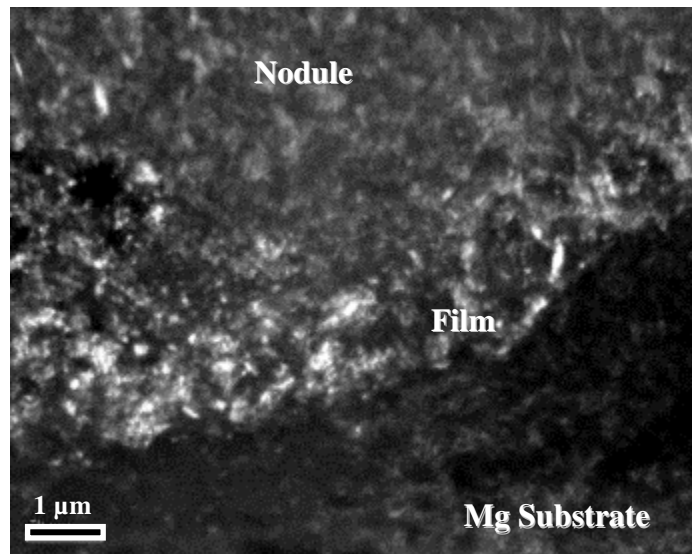


Figure 5.53: DF-TEM image of the film/substrate interface underneath a nodule showing the extent of crystallinity, as defined by the $\{200\}$ reflection of the cubic MgO structure.

Figure 5.53 shows a DF-TEM image of film/substrate interface region residing underneath a nodule, in which a portion of the $\{200\}$ reflection of the cubic MgO structure is identified (bright contrast) using the SAD technique. The extent of crystallinity, as defined by the $\{200\}$ plane in MgO, is found to be more prevalent within the thin film. Few of the MgO crystals appear to be scattered within the nodule.

Figure 5.54 and Figure 5.55 show the results of the element maps collected across the Mg/film interface without and with nodule using EDS. The main difference between the interfaces is seen in the Mg EDS map, in which the film between the nodule and the Mg substrate (Figure 5.55d) exhibits more Mg intensity versus the Mg/film interface without the nodule. This is consistent with formation of a distinct outer-layer within the nodule that acquired lower intensity of Mg.

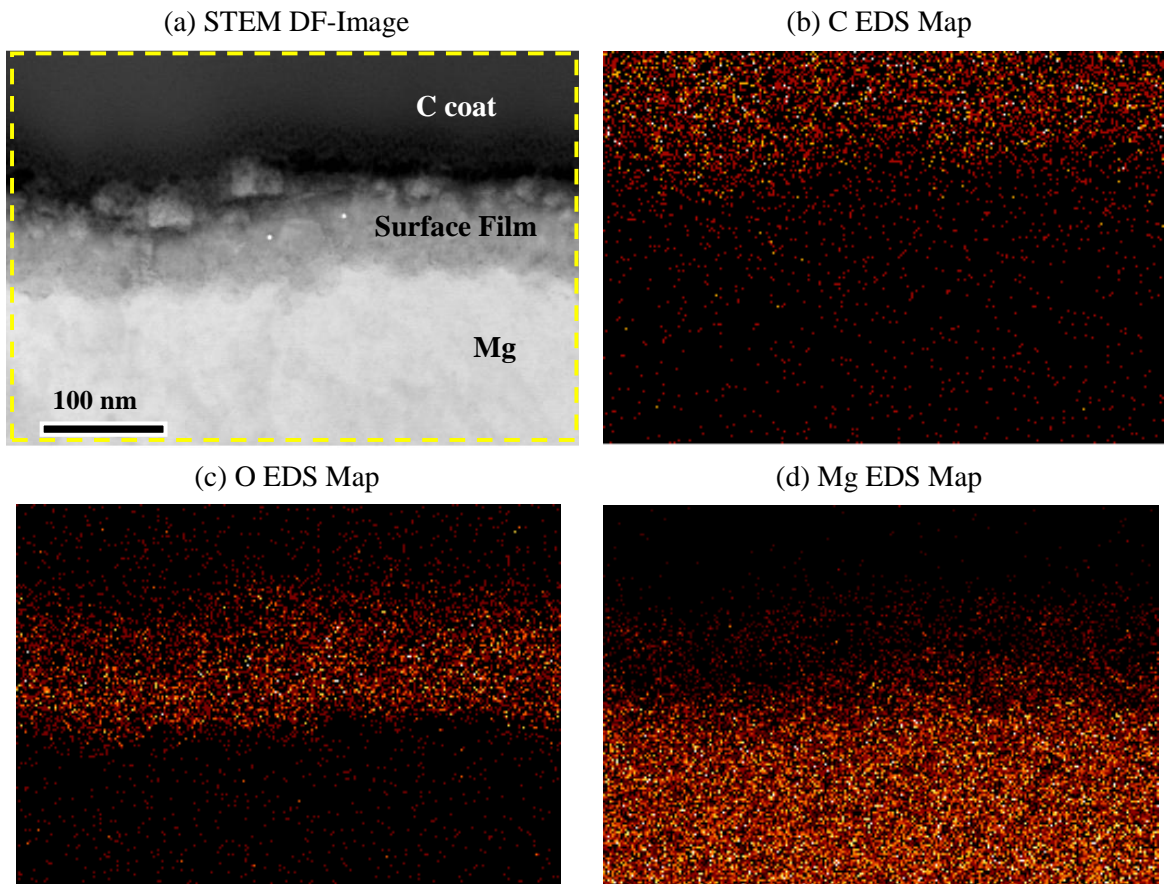


Figure 5.54: (a) DF-STEM image of the Mg/film interface without nodule and the Mg substrate, formed after aging at E_{corr} in 1 M NaOH for 48 h, utilized to capture an (b) C EDS map, (c) O EDS map and (d) Mg EDS map.

The O/Mg atomic ratio depth profile across the Mg/film interface with and without a nodule is shown in Figure 5.56. Both profiles through the film (with and

without a nodule) exhibit a similar form, namely a monotonic increase in the O/Mg atomic ratio moving away from the interface towards the surface. A maximum O/Mg atomic ratio of about 2, which is consistent with the formation of $\text{Mg}(\text{OH})_2$ is attained within both profiles (film with and without nodule). However, this maximum O/Mg atomic ratio is observed at the surface of the film without a nodule, whereas it is observed away from the surface of the film with a nodule.

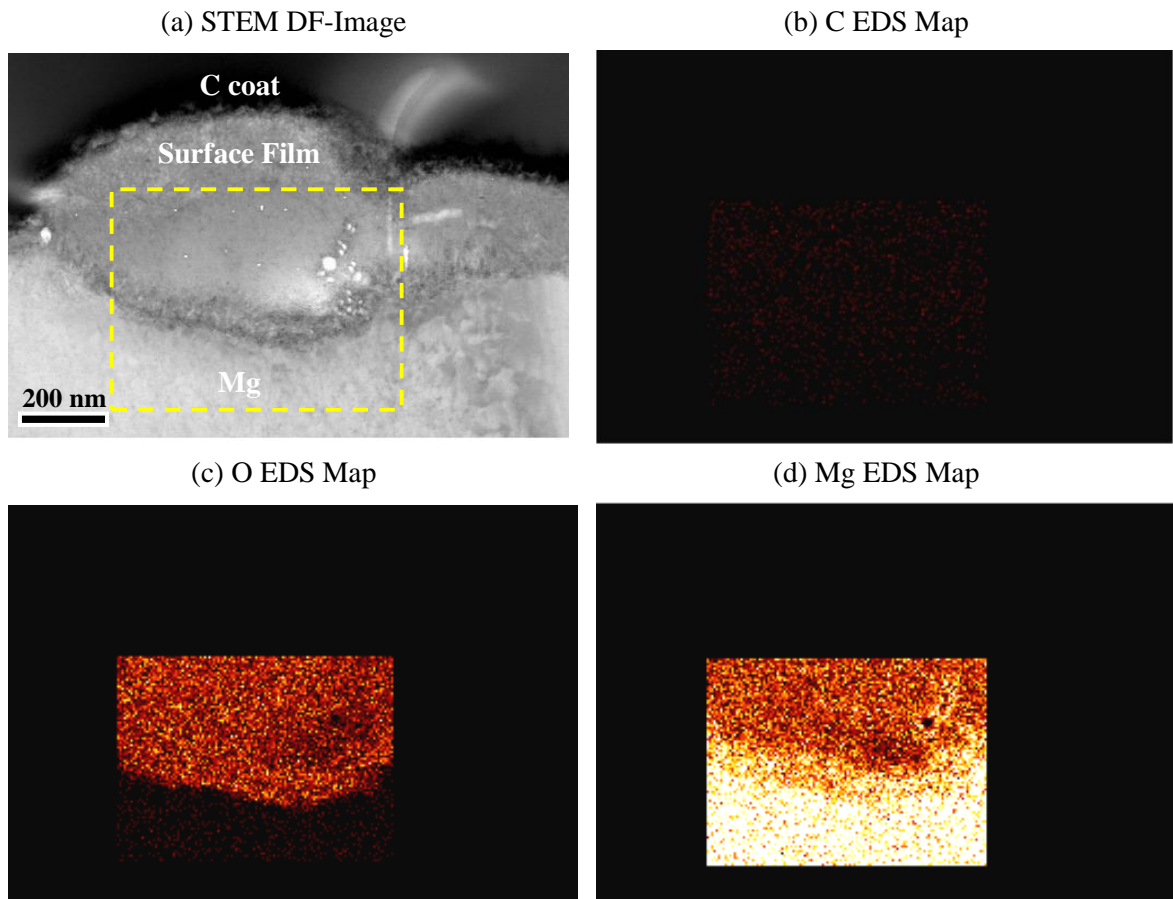


Figure 5.55: (a) DF-STEM image of the Mg/film interface directly underneath a nodule and the Mg substrate, formed after aging at E_{corr} in 1 M NaOH for 48 h, utilized to capture an (b) C EDS map, (c) O EDS map and (d) Mg EDS map.

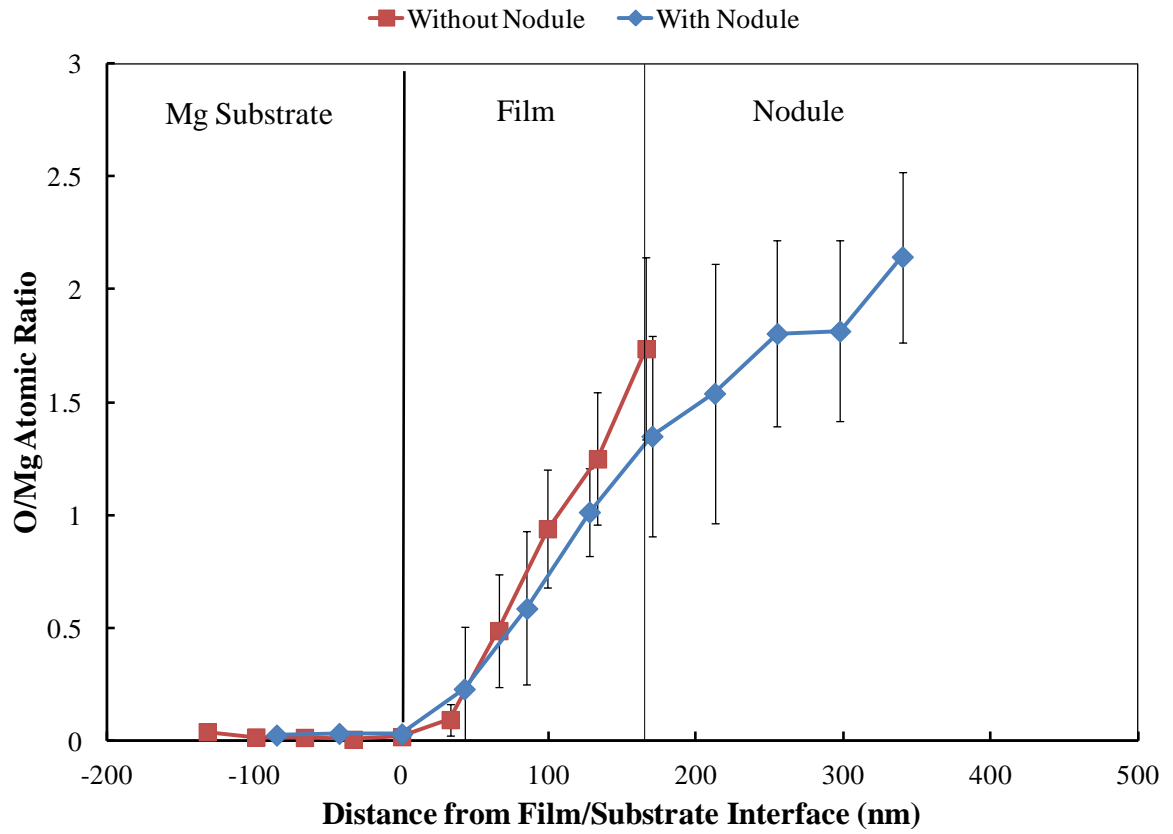


Figure 5.56: O/Mg atomic ratio depth profile through the Mg/film interface, with and without nodule formed after exposure to the 1 M NaOH solution for 48 h.

6. FILM STRUCTURE MODELS

6.1. Pure H₂O

Based on the direct imaging results of STEM–EDS examination, the film formed on Mg after mechanically polishing in laboratory air and subsequent exposure in H₂O at E_{corr} for 48 h consists of a diffuse bi-layer structure. The bi-layer structure consists of a relatively thin (50-90 nm), more porous, nano-crystalline MgO-rich inner layer and a much thicker (~700 nm), less-porous Mg(OH)₂-rich outer layer. A schematic of this diffuse bi-layer is shown in Figure 6.1.

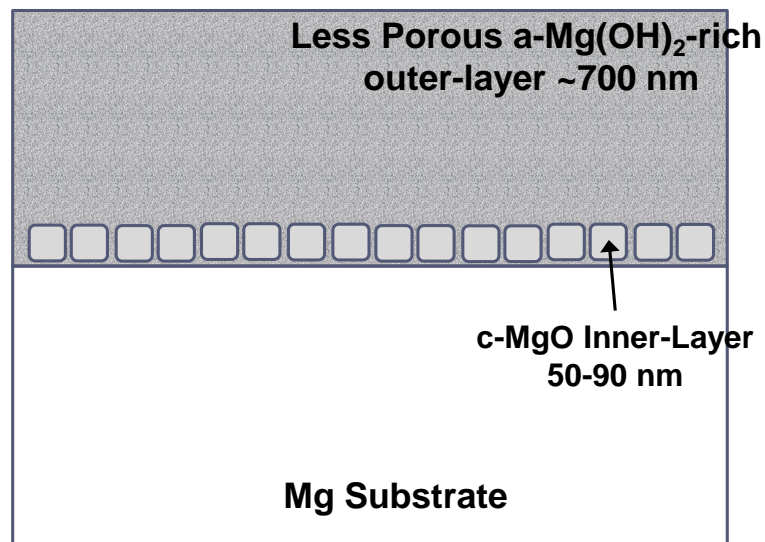


Figure 6.1: Schematic of the diffuse bi-layer structure of the film formed on Mg after aging at E_{corr} in pure H₂O at room temperature for 48 h.

The formation of a diffuse bi-layer consisting of an thicker outer hydroxide-rich film on top of a much thinner inner oxide-rich film agrees well with the analysis of the film formed on mechanically polished Mg after aging in H₂O reported by others using XPS [21], [25], [116] and ToF SIMS [31]. These studies all show that the mechanically

polishing in laboratory air produces a bi-layer structure comprised of an ultrathin $\text{Mg}(\text{OH})_2$ layer on top of a relatively thicker MgO inner layer. The inner MgO is believed to form from the interaction with O_2 gas, whereas the outer $\text{Mg}(\text{OH})_2$ layer is believed to form from the reaction of MgO and H_2O vapor (hydration). Aging in H_2O simply promotes the growth of the outer $\text{Mg}(\text{OH})_2$ surface layer by a dissolution-precipitation reaction involving the corrosion of the Mg substrate.

The observations reported herein, however do not agree all that well the direct imaging results reported by Nordlien et al. [24], particularly with respect to film structure. A third hydrated layer, which is susceptible to electron beam damage, is not observed to have formed at the Mg/film interface. Nordlien et al. did report that the subsequent dehydration and crystallization to MgO of this hydrated inner-layer with sustained irradiation was prevented for an extended period when the specimen holder was cooled with liquid nitrogen. Since the exposed cross-section sample utilized in this study was also cooled by a liquid nitrogen TEM holder, it seems reasonable that a similar layer would have been preserved during the TEM-EDS examination, if present. However, the EDS results presented in Figure 5.54 are not consistent with this possibility, since the calculated O/Mg atomic ratio is too low beneath the MgO -rich inner layer to account for the presence of a hydrated structure. The cause of this discrepancy is not well understood at this time, but it seems likely that the sample preparation procedure (FIB-milling verse ultramicrotomy) has a strong influence.

Moreover, Nordlein et al. [24] reported that the intermediate layer (seen as the inner layer in this study) was amorphous and dense, whereas formation of a porous

crystalline inner layer is observed in this study. The DF image shown in Figure 5.8 clearly shows that the inner MgO layer is likely nano-crystalline. The formation of a crystalline MgO layer is consistent with the generally recognized Mg oxidation process, which proceeds by an initial step of oxygen chemisorption, followed by the nucleation and lateral growth of oxide islands, and subsequent thickening after coalescence [6], [19], [117], [118], [119]. This crystalline film is also expected to be continuous, since, as Splinter et al. [19] reported, the rate of island (lateral) growth stage is significantly faster than that of the oxide thickening stage.

The observed porosity within the inner MgO-rich layer reveals that this inner film has undergone a breakdown to a reasonable extent. This breakdown is likely chemical in nature, resulting from the hydration of the native MgO layer. The energetically favorable hydration of MgO to Mg(OH)₂ [57], [58], [78], [79], [80], [120], [121], [122] produces a sizeable volume expansion, which likely plays a significant role in creating the observed porosity. This porosity may explain the discrepancy between the thickness of the MgO-rich inner layer formed after very short exposure times (up to 120 s) [21], [23], [25], [31], [32] and after much longer times (after 48 h) [24].

The E_{corr} transient measured in pure H₂O increased rapidly during exposure times of less than 2 h from negative values of -1.8 V_{SCE} up to a more noble potential of about -1.57 V_{SCE} and then stabilized at a slightly lower potential (~20 mV lower). The rapid increase of E_{corr} at shorter immersion times coincides with rapid dissolution of Mg [42], whereas the relatively steady E_{corr} coincides with the presence of a relatively thick surface film.

The aforementioned physical properties of the Mg surface film formed in H₂O, suggest that its EIS Nyquist spectrum will include two time constants. A higher frequency time constant that accounts for the capacitance of the film (CPE_{film}) and the solution resistance present within the film pores (R_{por}). $CPE_{\text{film}}/R_{\text{por}}$ will be used in the following text to describe this time constant. Also, a second, lower frequency time that accounts for the double layer capacitance (CPE_{dl}) and the charge transfer resistance (R_{ct}) of the faradic reactions occurring at Mg/film interface. This time constant will be described with $CPE_{\text{dl}}/R_{\text{ct}}$ in the following.

The diffuse bilayer film formed on Mg in H₂O includes an outer, less porous Mg(OH)₂-rich layer and a thinner, more porous, MgO-rich inner layer. Therefore, this porous film exhibits a film capacitance and resistance element for the electrolyte within the pores. However despite Al oxide film case, too much porosity in MgO-rich layer rules out its inhibitive role here. This is discussed in more detail in Section 7.1.

A charge transfer electrochemical reaction takes place when a reductant (usually metal) electrolytically dissolves at the electrode/electrolyte interface, the electrons moves into the electrode, and then the oxidant (metal ion) diffuses into the electrolyte. Charge transfer resistance is a unique kinetic characteristic of this redox reaction that describes its inherent speed at the electrode/electrolyte interface [94], [123]. Therefore, the R_{ct} term represents the resistance of the system against anodic dissolutions of Mg at the substrate interface with the solution. The observed porosity of the film formed on Mg shows that H₂O can penetrate via the pores, facilitating the charge transfer dissolution of Mg at the substrate/solution interface. Also, this observed porosity is presumed to facilitate a steady

flow of redox species such Mg^{2+} , OH^- and H^+ within the film. Therefore, the presence of a concentration gradient is not likely, and no mass transfer element is considered in the equivalent circuit. The EIS results, shown in Section 7.1, will indicate that the absence of a Warburg impedance element is consistent with this hypothesis.

Similarly, H_2O penetrating via the film porosity results in the accumulation of ions from the solution with the opposite charge of the excess electrode surface charge. This leads to the formation of a double layer capacitor (C_{dl}) across the substrate/solution interface [94], [123]. This is shown as CPE_{dl} in the equivalent circuit. CPE impedance is dependent on the frequency as follows:

Equation 6.1

Where C is the CPE constant, ω is rotary frequency ($\omega = 2\pi f$; f : frequency), and α is an exponent which equals 1 when the CPE is a pure capacitor.

6.2. Influence of Cl^- and η_{anodic}

The film formed by exposure in 0.01 M NaCl for 24 h at E_{corr} is found to be composed of a diffuse bilayer structure as well. This bi-layer structure consists of a relatively thin (50-100 nm) and porous nano-crystalline MgO-rich inner layer and a much thicker (~600 nm) and more porous $Mg(OH)_2$ -rich outer layer.

The intact film in un-pitted regions formed in 0.01 M NaCl solution at +0.1 V above E_b for 0.5 h after 24 h aging at E_{corr} exhibits a similar bilayer structure to 24 h aged sample at E_{corr} . However, both the outer $Mg(OH)_2$ -rich layer (~450 nm) and inner MgO-rich layer (~30-60 nm) are thinner (Figure 5.33). Furthermore, the pitted region film formed after polarizing at +0.1 V above E_b for 0.5 h after 24 h aging at E_{corr} exhibited a

thinner MgO-rich inner-layer (~20-30 nm) and Mg(OH)₂ rich middle-layer (~200-300 nm) buried under Mg(OH)₂-rich needle-like layer.

The significant findings regarding the composition and structure of the film formed in 0.01 M NaCl based on the SEM and STEM-EDS studies are summarized in Table 6.1. A schematic of the film inside a pit is shown in Figure 6.2. The film formed at E_{corr} and the film formed during anodic polarizing are assigned a similar film structure model as that assigned to the pure H₂O case (Figure 6.1).

Table 6.1: Summary of Mg film composition and structure formed in 0.01 M NaCl.

Film Formation Condition	Film Structure	Film Composition	Film Thickness
24 h aged @ E_{corr} in 0.01 M NaCl	Diffuse bi-layer: porous outer + broken-down inner layer	Porous outer layer: a-Mg(OH) ₂ -rich + Cl through film ----- Porous inner layer: c-MgO-rich + Cl through film	~300-600 nm ----- ~ 50-100 nm
Outside a pit; 24 h @ E_{corr} + 0.5 h anodically polarized @ $E > E_b$	Diffuse bi-layer: porous outer + broken-down inner layer	Porous outer layer: a-Mg(OH) ₂ -rich + Cl through film	~300-450 nm
		Porous inner layer: c-MgO-rich + Cl through film	~ 30-60 nm
Inside a pit; 24 h @ E_{corr} + 0.5 h anodically polarized @ $E > E_b$	Diffuse tri-layer: porous needle-shape top layer + porous middle and inner-layer + large inner-layer free areas	Porous top layer: a-Mg(OH) ₂ -rich + Cl through film ----- Porous middle layer: c-Mg(OH) ₂ -rich + Cl through film ----- Porous inner layer: c-MgO-rich + Cl through film	~ 0.2-1 μm ----- ~200-300 nm ----- ~ 20-30 nm

Qualitatively speaking, by comparing the STEM images of the film formed in H₂O and 0.01 NaCl (Figure 5.9a vs. Figure 5.22a-b), it appears that the Mg(OH)₂-rich layer formed at E_{corr} in 0.01 M NaCl exhibits more porosity (dark spots) with relatively

larger pore size. At some locations (Figure 5.22b), these pores are increased in size, up to ~50 nm, and extend into the MgO-rich layer. This suggests that the $\text{Mg}(\text{OH})_2$ -rich layer is more damaged in presence of Cl^- anions.

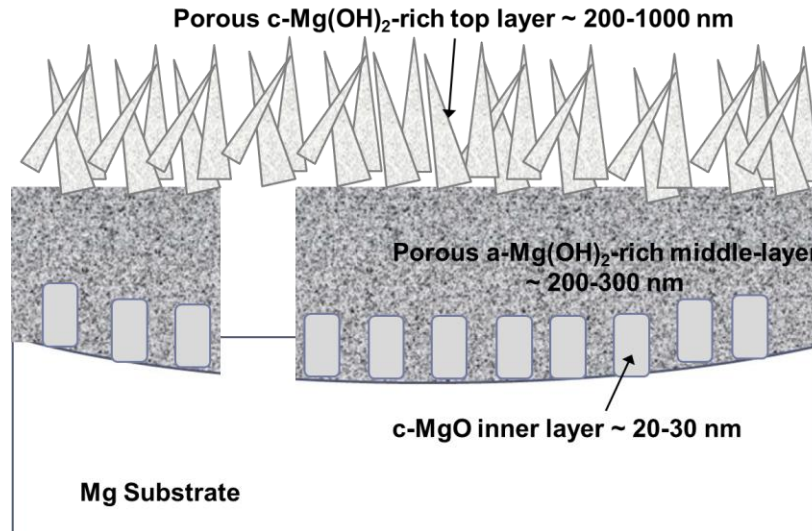


Figure 6.2: Schematic of the film formed inside a pit after anodic polarization at +0.1 V vs. E_b for 0.5 h after aging at E_{corr} in 0.01 M NaCl for 24 h.

Furthermore, EDS analysis of the film formed in 0.01 M NaCl solution at E_{corr} (Figure 5.25 and Figure 5.26) confirmed the presence of Cl. Cl^- presence within the films is an important observation based on the proposed Cl^- film destructive model, reported in the literature [21], [39], [40], [41], [51]. Yao et al. [21] recorded the binding energy ratio of Cl to Mg versus the film thickness formed on Mg melt spun ribbon exposed to 3 wt% NaCl at E_{corr} to investigate the contribution of Cl in the film. They reported that Cl concentration within the film reduced by two thirds from the outer layer to the inner layer after 1 min exposure, whereas it became uniform after 3 h [21]. This is consistent with observation of Cl everywhere across the film recorded in this study (Figure 5.44), which exhibited lower Cl concentrations adjacent to the inner layer. Yao et al. [21] attributed

this uniform Cl contribution to increased MgO hydration to Mg(OH)₂ in presence of NaCl, in which due to different molar volume of hydroxide compared with oxide causes the film to undergo more distortion; and therefore, accelerated Cl⁻ ingress within the film. Formation of a thinner MgO-rich inner layer and a porous Mg(OH)₂ outer layer in this study is consistent with Yao et al.'s hypothesis [21].

Cl⁻ was also reported to increase the solubility and thinning of Mg(OH)₂ enhancing the formation of porosity within the film [124]. Considering Cl⁻ incorporation in the film as hydroxy-chloride complex products, Williams et al. [124] calculated the modified solubility product (K_{sp}) of Mg(OH)₂, as shown in Equation 6.2. They reported that this will lead to an increase of the K_{sp} that Mg(OH)₂, which will accelerate hydroxide dissolution. Interestingly, the lower concentration 0.01 M NaCl solution used in this study, results into an increase of the K_{sp} of Mg(OH)₂ by nearly 200 times, according to Equation 6.2.

Equation 6.2 [51]

The negative effect of Cl⁻ on hydroxide solubility is correlated to Mg-Cl formation within the Mg(OH)₂ structure. Several hydroxy-chloride complex products such as MgCl₂.6H₂O and Mg₃(OH)₅Cl.4H₂O [88], 5(Mg(OH)₂).MgCl₂ [41], and Mg₆(OH)₁₀Cl₂.H₂O [39], [40] are reported to be formed in Mg film using different direct surface analysis techniques. The Mg(OH)₂ structure is such that Mg cation planes are located between alternating pairs of hydroxyl group (OH) planes, which creates a hexagonal close-packed unit cell [38]. Each hydroxyl group is bonded to three Mg cations in an interlaying distance via three fold axes, in which each OH is surrounded with three adjacent groups. Feitknecht et

al. [86], [87] postulated that Mg-Cl salts incorporate within the interlayer spacing of $\text{Mg}(\text{OH})_2$ and increase the interlayer spacing, which results in increased solubility of the hydroxide.

One concern is that both enhanced MgO hydration and $\text{Mg}(\text{OH})_2$ solubility in presence of Cl^- are used to rationalize the significant porosity of $\text{Mg}(\text{OH})_2$ -rich layer, which is thicker in the pitted region film. To elucidate this, attention should be drawn to the role of anodic polarization at the pitted region film compared to the un-pitted regions and films grown at E_{corr} . The thickness of $\text{Mg}(\text{OH})_2$ -rich layer on the un-pitted regions anodic film and the E_{corr} film are both thinner than that formed in H_2O . A significant porosity increase is observed in the presence of Cl^- accounting for the enhanced solubility of the $\text{Mg}(\text{OH})_2$. Moreover, increased porosity was observed within the MgO-rich layer formed on anodic pitted and un-pitted region films and E_{corr} film. This also accounts for enhanced MgO hydration in presence of Cl^- .

A thicker $\text{Mg}(\text{OH})_2$ -rich layer is only observed for pitted region anodic films where the top needle-like layer is formed. This could be correlated to enhanced dissolution of Mg^{2+} via the pitted region film as follows. The MgO-rich inner layer inside was found to be broken down at some locations adjacent to the film/substrate interface (Figure 5.35b). The presence of significant porosity within the middle and top layers accounts for the enhanced solubility of the $\text{Mg}(\text{OH})_2$ -rich layer due to formation of hydroxy-chloride complex products [2], [21], [39], [40], [41], [51], [86], [87], [88]. Also, accelerated hydration of MgO to $\text{Mg}(\text{OH})_2$ [21] is consistent with a thinner oxide inner layer with a significant increased porosity (Figure 5.32 and Figure 5.35). These

observations suggest an easier ingress of the Cl^- -containing electrolyte via the porous film, bringing Cl^- anions to the Mg substrate (Figure 5.44). Moreover, accelerated Mg dissolution at potentials above E_b generates a higher amounts of Mg^{2+} cations, which could potentially deplete OH^- at the Mg/film interface [39], [40]. When present at the Mg/film interface, the Cl^- anions can form soluble salts on a corroded surface with an increased surface area and locally decrease the pH [21], [39], [40], [41]. Therefore, the Mg dissolution is likely highly encouraged and the top layer $\text{Mg}(\text{OH})_2$ -rich needles will be precipitated on top of the damaged $\text{MgO}/\text{Mg}(\text{OH})_2$. The low value of local pH at these film free areas prevents the formation of the $\text{Mg}(\text{OH})_2$ -rich needles at the Mg/film interface, since the $\text{Mg}(\text{OH})_2$ saturation limit cannot be reached. Note that the DF-TEM image of the film formed inside a pit (Figure 5.9b) showed that the MgO nano-crystals are present within the $\text{Mg}(\text{OH})_2$ -rich inner-layer away from interface. This is consistent with a damaged MgO-rich inner layer and accelerated Mg dissolution via the bare metallic Mg substrate areas exposed to the penetrating electrolyte.

Additionally, an O/Mg atomic ratio of lower than 2 (~ 1.5) was observed in the depth profile of the films, formed in 0.01 M NaCl solutions above E_b . This could be correlated to the presence of MgO nano-crystals away from the Mg/film interface (Figure 5.9b and Figure 5.9c). However, Mg incorporation with Cl^- in the hydroxy-chloride products is likely to decrease the Mg/O ratio [21], [39], [40], [41]. For instance, $5(\text{Mg}(\text{OH})_2)\cdot\text{MgCl}_2$ and $\text{Mg}_3(\text{OH})_5\text{Cl}$ compounds have an O/Mg atomic ratio of 1.67. Also, the observation of Fe particles within the top layer of the film, formed inside a pit,

provides evidence in support of the micro-galvanic effect of nobler impurity particles on breakdown of Mg surface film [51].

The Mg E_{corr} transient, measured 0.01 M NaCl solutions (Figure 5.12), displayed similar behaviour to that recorded in pure H₂O (Figure 5.3). The E_{corr} increased rapidly for exposure times less than 2 h from negative values of -1.8 V_{SCE} up to a more noble potential of about -1.57 V_{SCE} and then stabilized at a slightly lower potential (~ -1.59 V). The rapid increase of E_{corr} at short immersion time coincides with a rapid dissolution of Mg, whereas the relatively steady E_{corr} coincides with the presence of a relatively thick surface film.

Swiatowska et al. [42] compared the E_{corr} transient of mechanically dry ground Mg specimen exposed to 0.01 M NaCl with the dissolution rate of Mg in the electrolyte using an inductively coupled plasma optical emission spectrometer (ICP-OES) paired with the potentiostat. They reported the rapid increase of the E_{corr} during the initial exposure time coincides with a faster generation of Mg cations through the electrolyte. Also, the cation release rate is consistent with the small changes of the steady E_{corr} at longer immersion time.

The above film structure results suggest that EIS Nyquist spectrum for the E_{corr} film formed in 0.01 M NaCl will exhibit two time constants similar to that proposed for the H₂O film (see Section 6.1). This includes a high frequency loop representing $\text{CPE}_{\text{film}}/\text{R}_{\text{por}}$ and a lower frequency loop to describe $\text{CPE}_{\text{dl}}/\text{R}_{\text{ct}}$. The E_{corr} film formed in 0.01 M NaCl exhibits similar diffuse bilayer structure as the H₂O film, albeit with more porosity in both layers. Therefore, the $\text{CPE}_{\text{film}}/\text{R}_{\text{por}}$ is considered to account for the film

capacitance and the solution impedance within the pores. Similar to the H₂O film, the CPE_{dl}/R_{ct} time constant accounts for the C_{dl} of the penetrating electrolyte across the Mg/film interface and Mg charge transfer corrosion reaction, respectively. However, due to the severity of the film damage within the pitted region anodic film, formed in 0.01 M NaCl, the CPE_{film}/R_{por} time constant is expected to be negligible; and therefore, it will not be suggested to be present in the EIS Nyquist spectrum of the anodically polarized sample.

6.3. Influence of pH

Based on the direct imaging results of STEM–EDS examination, the film formed on Mg after exposure to the 1 M NaOH test solution for 48 h is found to consist mainly of a relatively thin (50-150 nm) continuous crystalline MgO layer that has been hydrated; more at the surface and less within the bulk. This layer is also decorated with what appears to be a random distribution of significantly thicker (about 500 nm) and Mg(OH)₂ nodules, which reside on a more-porous region of the partially-hydrated MgO layer. Figure 6.3 presents a schematic of the proposed nature of the film.

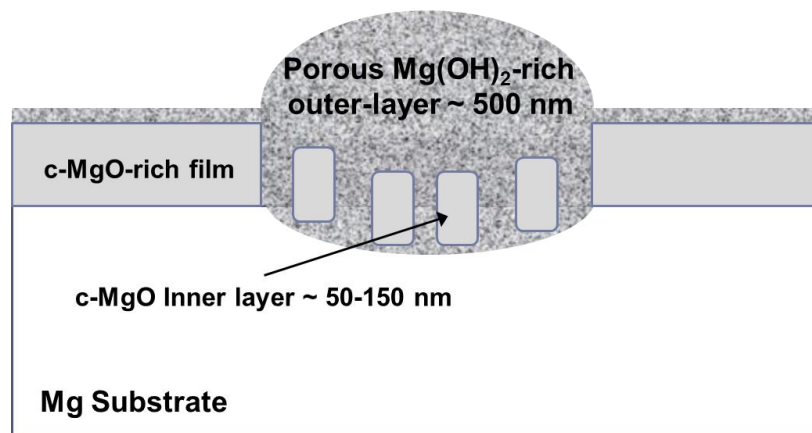


Figure 6.3: Schematic diagram showing the nature of the film on Mg formed after exposure in 1 M NaOH composed of a crystalline MgO-rich film and amorphous Mg(OH)₂-rich nodules on top of porous crystalline MgO film sections.

The experimentally measured O/Mg atomic ratio within a nodule exhibited value of 1.8, 1.8 and 2.1 (Figure 5.24). Based on the O/Mg atomic ratio of about 2, it is assumed here that the nodule is Mg(OH)₂. However, the DF-TEM image in Figure 5.21 reveals that the nodule contains crystalline MgO as a minor component. Therefore, it is reasonable to expect that the O/Mg atomic ratio within the nodule to be somewhat lower than the theoretical value of 2, which would be expected if Mg(OH)₂ was the only component. The absence of a crystalline diffraction ring pattern for Mg(OH)₂ implies that the compound is amorphous in structure.

The DF-TEM image in Figure 5.21 also reveals that the thin continuous layer is mainly crystalline MgO. This finding appears not to be well supported by the O/Mg atomic ratio profiles presented in Figure 5.24. In both profiles, the O/Mg atomic ratio increases from 0 to 1.8 over a distance that corresponds to the thickness of the continuous layer (50–150 nm). An O/Mg atomic ratio greater than 1 can be explained by the co-presence of Mg(OH)₂, particularly toward the surface of the film. In this case, Mg(OH)₂

can be formed from the hydration of MgO, both in humid air and in H₂O [21], [23], [31]. An O/Mg atomic ratio less than 1 can be explained by the co-presence of the Mg substrate, particularly toward the film/substrate interface. As Figure 5.51 shows, the film/substrate interface is roughened to a significant extent. Therefore, it is argued that 30 nm × 30 nm EDS spectrum squares selected to plot the O/Mg atomic ratio profile, are not small enough to eliminate the Mg substrate signal from the total Mg signal within the row of squares adjacent to the roughened film/substrate interface.

There are two major differences between the nature of the film that forms after exposure to 1 M NaOH and that formed after exposure to pure H₂O. One involves the extent of the porosity observed in the thin partially-hydrated MgO layer, which appears to be lower after exposure to NaOH than after exposure to pure H₂O. As mentioned previously, the extent of porosity in the MgO layer after exposure to 1 M NaOH tends to be higher in the portion that resides underneath a Mg(OH)₂ nodule. However, qualitatively speaking, this increased extent still appears to be lower than that observed after exposure to pure H₂O. The other involves the extent of coverage of the thicker, outer Mg(OH)₂ layer, which forms a partial layer (nodules) when formed in 1 M NaOH and complete when formed in pure H₂O.

The large E_{corr} drop observed in 1 M NaOH (Figure 5.45) and 1 M NaOH + 0.01 M Na₂SO₄ (Figure 5.46) behaviour suggests that irregular cycles of film breakdown and subsequent repair has occurred. If this is true, then the extreme minimum potential observed during the drop should correspond to a physical situation in which a stress-rupture has occurred. Given that this localized surface film stress-rupture event is

believed to be physically and chemically similar to the global stress-rupture of the film formed in pure H₂O under steady-state conditions, it follows that there should be some agreement between the E_{corr} exhibited by Mg in both cases. This appears so, since the minimum potential observed during the drops is about $-1.62 V_{\text{SCE}}$ and that observed during the steady-state corrosion in pure H₂O is about $-1.54 V_{\text{SCE}}$ (Figure 5.3).

Potential drops of this form, shown in Figure 5.45, have been previously reported for Mg alloy AZ31 in 0.5 M KOH [125]. It was argued that the phenomenon in this case could be explained by a repetitive process of dissolution/repassivation or film rupture/dissolution/repassivation, with the latter believed to be more plausible. It was proposed that the dissolution process most likely starts by rupture of the outer hydrated layer of the film as a result of the low Pilling-Bedworth ratio (PBR) of MgO/Mg compared to that of Mg(OH)₂/Mg. It should be noted that, comparing the electrochemical behaviour of AZ31 and pure Mg in strongly alkaline solutions suggest that a bulk Al content of 3 wt.% is not sufficient to alter the electrochemical behaviour of Mg despite the presence of Al₂O₃ within the surface film [125].

The above film structure model for Mg film formed in 1 M NaOH film suggests that its EIS Nyquist spectrum will include three time constants. A high frequency time constant that accounts for $CPE_{\text{film}}/R_{\text{por}}$ and a lower frequency loop describing $CPE_{\text{dl}}/R_{\text{ct}}$. As stated earlier, $CPE_{\text{film}}/R_{\text{por}}$ describes the dielectric behaviour of the film and the solution resistance within film pores, whereas $CPE_{\text{dl}}/R_{\text{ct}}$ accounts for the double layer capacitance of the electrolyte and Mg charge transfer corrosion reaction across the Mg/film interface, respectively. Due to the increased compactness of the film compared

to the H₂O and 0.01 NaCl films, a Warburg time constant (W), is also expected to be present at lowest frequency that accounts for the mass transport of Mg²⁺ within the film. More evidence of the mass transport mechanism was observed as the i_L , in the potentiodynamic polarization measurement recorded in 1 M NaOH solution.

7. FILM STRUCTURE VALIDATION BY EIS

7.1. Pure H₂O

Figure 7.1 presents the impedance spectra measured for Mg in pure H₂O after 48 h aging. The experimental results are depicted as red diamonds on the Nyquist graph in Figure 7.1a, and on the Bode plots are superimposed as the red diamonds (Figure 7.1b) showing the real/imaginary impedance values variation with frequency. Note that the positive y-axis plane spectrum corresponds to real impedance, whereas the negative y-axis plane spectrum corresponds to imaginary impedance values.

It appears that the Nyquist spectrum of Mg in pure H₂O is composed of two capacitive semi-circles. This can be identified as a second shoulder formed at Z' values of nearly 16,000 k Ω . However, two capacitive loops are likely overlapped and the high frequency capacitive loop has dominated parts of the medium frequency semi-circle. Furthermore, the Kramer-Kronig transforms of the experimental spectra are superimposed on the data in Figure 7.1b. The solid blue line corresponds to the real impedance transformed values, whereas the brown solid line represents the imaginary impedance transformed values. The transformed results obey Kramer-Kronig relations over the entire range of frequency. This verifies stability, linearity and causality of the studied system.

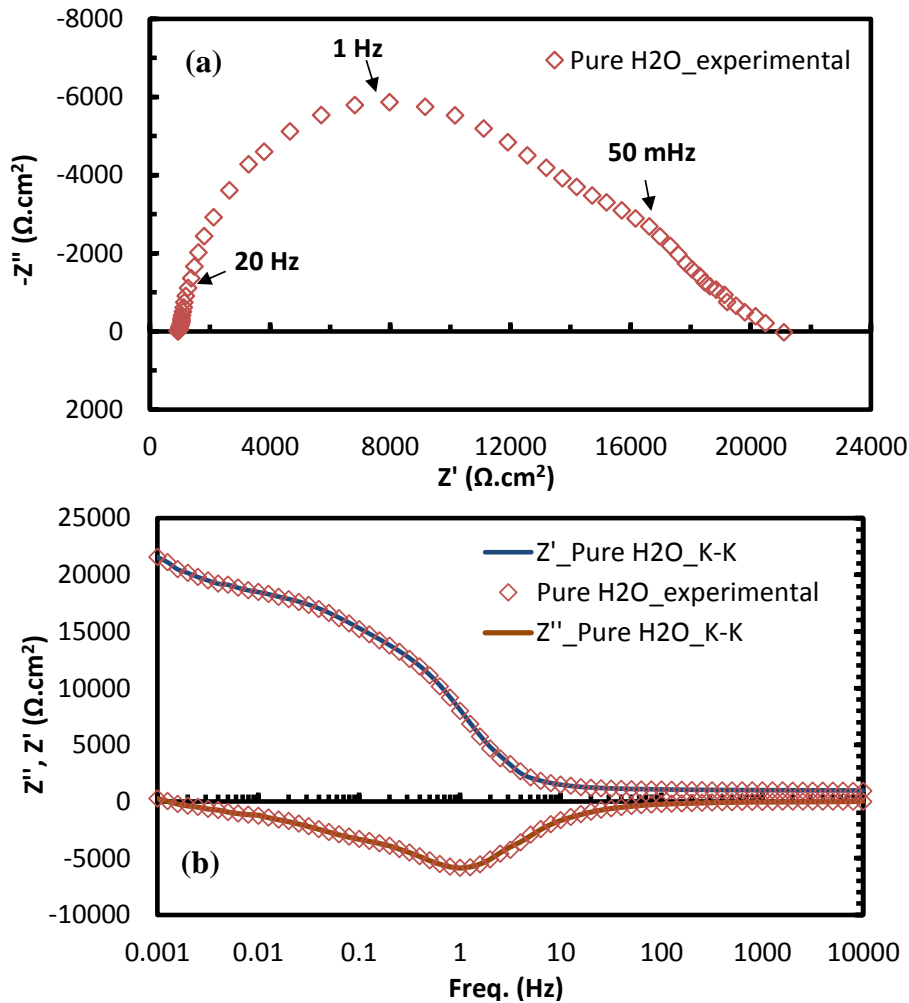


Figure 7.1: (a) Experimental Nyquist spectrum measured for Mg after 48 h aging in H₂O (b) Comparison of Kramer-Kronig transform with real and imaginary results.

The recorded EIS spectrum in H₂O corroborates the presence of both high frequency $CPE_{\text{film}}/R_{\text{por}}$ and low frequency $CPE_{\text{dl}}/R_{\text{ct}}$ time constants, as suggested by the film structure model (see Section 6.1). The SEM and STEM-EDS studies showed that the film formed exposed in pure H₂O consists of a diffuse bilayer structure. This diffuse bilayer film includes an outer less porous layer of Mg(OH)₂-rich and a thinner more porous MgO-rich inner layer. Therefore, this porous film is hypothesised to exhibit a film capacitance and a resistance element for the electrolyte within the pores. This concept has

been previously used for porous Al anodized film, in which a thin Al_2O_3 barrier film is buried under a thicker porous hydrated- Al_2O_3 outer layer [126], [127], [128], [129], [130]. The $\text{CPE}_{\text{film}}/\text{R}_{\text{por}}$ loop is consistent with the first capacitive loop, which is detected as the high frequency capacitive arc in the pure H_2O Nyquist spectrum (Figure 7.1a). Accordingly, once the electrolyte reaches the Mg substrate through the porous film, it forms an ionic double layer capacitance across the electrode interface and facilitates the redox electrochemical reactions at the interface [11], [12], [13]. Hence, the double layer is expected to generate a capacitor impedance element and the redox reactions occurring at the Mg/film interface imply a charge transfer resistance. This $\text{CPE}_{\text{dl}}/\text{R}_{\text{ct}}$ parallel impedance results in a second capacitive loop, which is acquired as the low frequency capacitance. The low frequency loci of the $\text{CPE}_{\text{dl}}/\text{R}_{\text{ct}}$ loop occurs because they are physically attributed to the Mg/film interface, which exhibits the lowest frequency compared to film and bulk solution impedance elements. Unlike the Al oxide case, too much porosity in the MgO-rich layer rules out its inhibitive role here.

Based on the direct imaging results of STEM-EDS examination, it was found that the film formed on mechanically polished in laboratory air Mg after subsequent exposure in H_2O at E_{corr} for 48 h consists of a diffuse bi-layer structure. The observed porosity within the inner MgO-rich layer reveals that this inner film has undergone a breakdown to a reasonable extent. This breakdown is likely chemical in nature resulting from the hydration of the native MgO layer. The energetically favorable hydration of MgO to $\text{Mg}(\text{OH})_2$ [58], [78], [79], [80], [81], [118], [120], [121], [122] exerts a considerable volume expansion, which likely plays a significant role in creating the observed porosity.

This porosity may explain the discrepancy between the thickness of the MgO-rich inner layer formed after very short exposure times (up to 120 s) [21], [22], [31], [32], [116] and after very long times (after 48 h) [24]. As discussed by Yao et al. [21], this porosity enhances the egress of Mg cations, which are produced from the anodic dissolution of the Mg alloy, to the interface between the film and H₂O. Overcoming the solubility limit of hydroxide in this region initiates the precipitation of Mg(OH)₂ on the surface. Thus, the Mg(OH)₂ outer layer continues to grow at the expense of the Mg alloy substrate. Complete hydration of the air-formed MgO layer is not expected based on reported hydration of MgO powders in aqueous solution, in which MgO rapidly converts to Mg(OH)₂ [120]. The platelet morphology of the relatively thick outer Mg(OH)₂-rich layer is consistent with the dissolution–precipitation formation mechanism [33].

This two-step surface film evolution process (hydration followed by dissolution–precipitation) is consistent with the observed E_{corr} behavior (Figure 5.3). Rather than attributing the entire initial slow increase followed by a plateau to the rapid growth of a Mg(OH)₂ film, as done by others [2], [3], [15], perhaps the initial slow increase stage could be attributed to the hydration reaction of the native MgO layer; and the plateau stage could be attributed to the rapidly growing Mg(OH)₂ film. If true, then controlling the hydration kinetics may provide a promising corrosion control pathway. The hydration of crystalline MgO thin films has been studied to a limited extent [58], [80], [81], and the process has been found to be influenced by various properties such as crystallinity, grain size, roughness, and density.

7.2. 0.01 M NaCl vs. H₂O

The EIS spectra recorded in 0.01 M NaCl after 24 h aging are shown in Figure 7.2. The Nyquist curve of a Mg sample measured at E_{corr} is shown in Figure 7.2a, and the Kramer-Kronig transforms of Z' and Z'' are superimposed on experimental results in Figure 7.2b (to verify the stability, linearity, and causality of the system). Furthermore, the Nyquist plot of a Mg specimen measured at +0.1 V vs. E_b (-1.0 V_{SCE}) is presented in Figure 7.3a, and the K-K transforms confirming the stability of system in this condition are shown in Figure 7.3b.

The Nyquist spectrum measured at E_{corr} contains a high frequency and a medium frequency capacitive loop, as well as a low frequency inductive loop. The presence of two high and low frequency time constants is consistent with the proposed EIS Nyquist spectrum for aged Mg film in 0.01 M NaCl at E_{corr} , in the film structure model section (see Section 6.16.2). In contrast, the anodically polarized spectrum, recorded above E_b , primarily exhibits only one capacitive loop. It appears that the medium frequency capacitive loop measured at E_{corr} dominates the high frequency capacitance recorded at +0.1 V vs. E_b (-1.0 V_{SCE}). This is also in agreement with the suggested EIS Nyquist spectrum for anodically polarized Mg film in 0.01 M NaCl above E_b , based on the film structure model section (see Section 6.2).

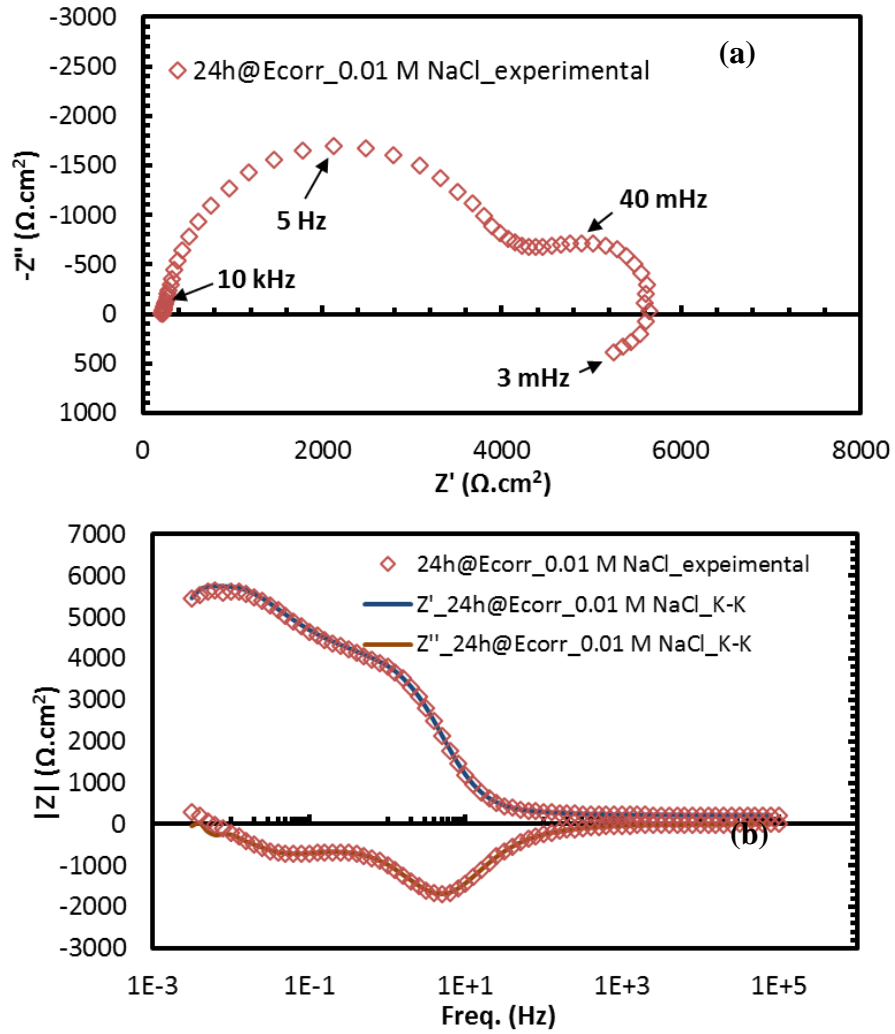


Figure 7.2: Experimental Nyquist spectra for Mg (a) after 24 h aging in 0.01 M NaCl and, (b) comparison of Kramer-Kronig transform with real and imaginary results.

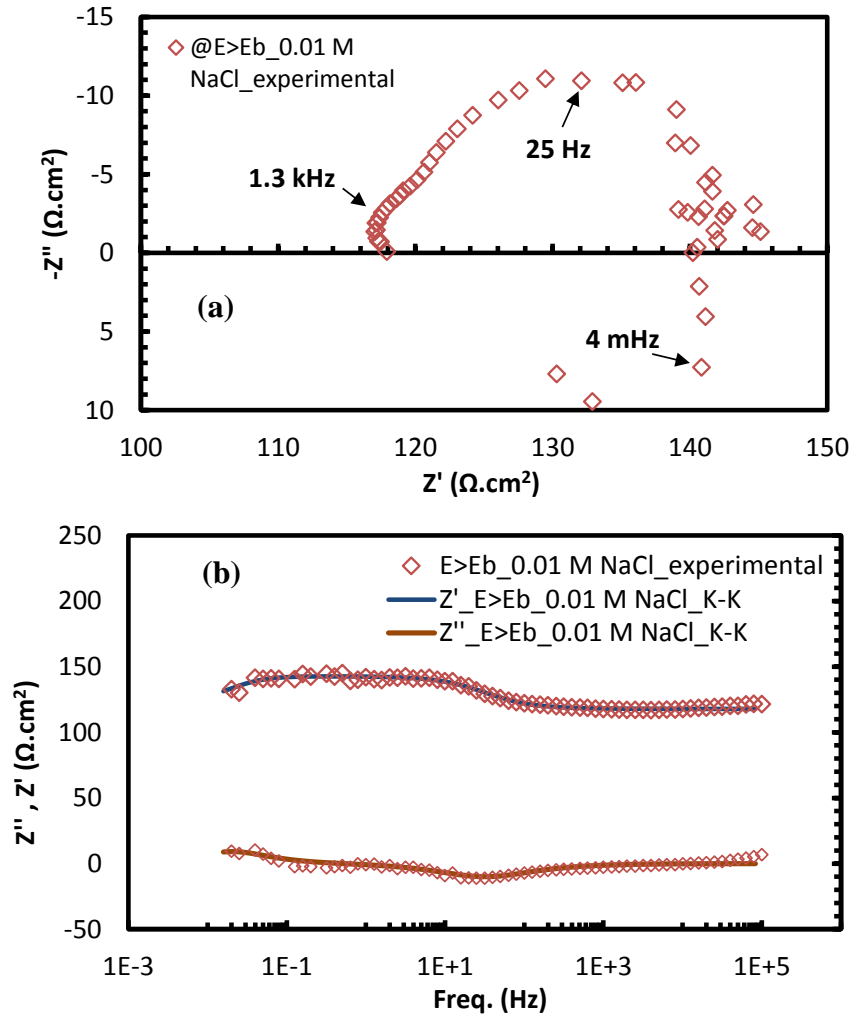


Figure 7.3: Experimental Nyquist spectra for Mg (a) after 24 h aging in 0.01 M NaCl and 0.5 h potentiostatic exposure at +0.1 vs E_b , and (b) comparison of Kramer-Kronig transform with real and imaginary results.

In order to perform a better comparison between the 0.01 M NaCl and H_2O EIS behaviour, their Nyquist spectra are superimposed on a Nyquist curve, as shown in Figure 7.4. The capacitive loop obtained for the anodically polarized sample is substantially decreased in size compared to the loops recorded at E_{corr} . Moreover, the total Nyquist spectrum, measured at +0.1 V vs. E_b ($-1.0 \text{ V}_{\text{SCE}}$), exhibits significantly lower impedance

magnitudes with respect to the E_{corr} spectrum. However, compared to H_2O , both the E_{corr} and anodically polarized Nyquist spectra exhibit lower impedance magnitudes. This suggests that the Mg film formed in H_2O have higher R_{ct} and R_{por} and lower C_{dl} and C_{film} values versus 0.01 M NaCl films. Note that R_{ct} represents the resistance of the system against anodic dissolutions of Mg at the substrate interface with the solution. Higher values of R_{ct} and R_{por} along with a decreased C_{dl} and/or C_{film} , coincides with an improvement in the protection of the film [48], [50], [131]. Based on the Stern-Geary equation [132], R_{ct} is proportional to the reciprocal value of the i_{corr} ; hence, the higher R_{ct} , the lower the i_{corr} is at the interface. Moreover, the dielectric capacitance correlation with the inverse value of the film thickness [133] (Equation 7.1) suggests that a decreased C_{dl} and/or C_{film} capacitance is either due to a thicker compact film or a repaired porous film.

–

Equation 7.1

Another major difference between the 0.01 M NaCl spectra and H_2O is the occurrence of an inductive loop at low frequencies in the chloride solutions. This impedance loop is an inductive element, Z_L , which has already been reported in other corrosion case studies such as Fe in H_2SO_4 [134], [135], [136], [137], Zn in Na_2SO_4 [138], Al in Cl^- containing solutions [139], [140], [141], and Al in KOH test solutions [142]. Physically, an inductor is an electrical component that acts to oppose any change in current by storing the energy in a magnetic field. When an AC voltage is applied to an inductor, it changes the current. Therefore, the inductor magnetic field will induce a counter current against the electron flow to delay the motion or oppose the cause of change [143]. Consequently, inductor is usually interpreted as a relaxation phenomenon

that occurs at the substrate/electrolyte interface and creates its impedance at low frequencies.

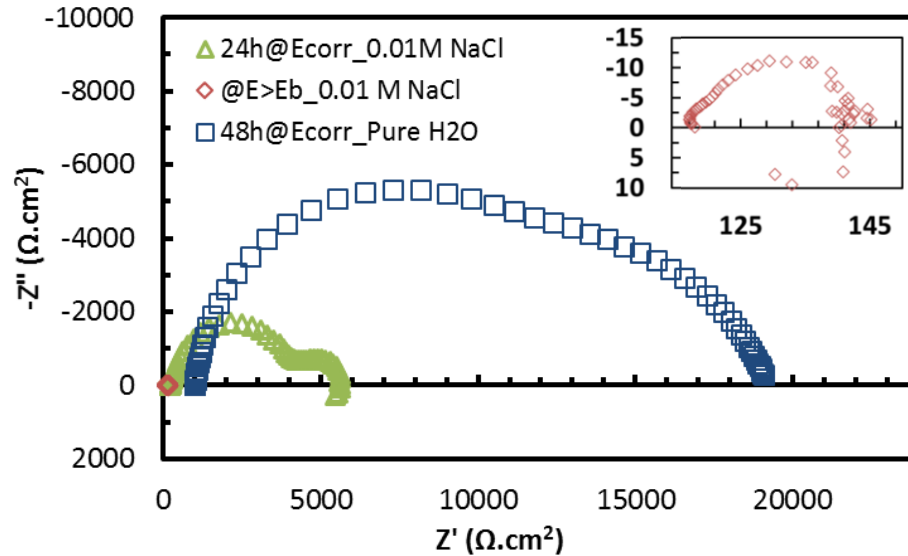


Figure 7.4: Comparison of Nyquist spectra recorded in 0.01 M NaCl at E_{corr} after 24 h and 0.5 h at $+0.1$ vs E_b after 24 h aging versus pure H_2O .

The film formed in 0.01 NaCl after 24 h aging at E_{corr} was found to exhibit a diffuse bilayer structure similar to pure H_2O film based on the SEM and STEM-EDS results. However, the total porosity of the film was observed to have increased (Table 6.1). Therefore, the Nyquist spectrum measured at E_{corr} in 0.01 NaCl solution (Figure 7.2a) was expected to consist of a high frequency $\text{CPE}_{\text{film}}/R_{\text{por}}$ and a low frequency $\text{CPE}_{\text{dl}}/R_{\text{ct}}$ capacitive loop. However, this Nyquist spectrum showed an inductive loop at the low frequencies. Inductor is not a physically based conclusive element using the direct observation results, and is only considered as a chemical mechanistic parameter. Furthermore, qualitatively speaking, the lower value of R_{por} in the 0.01 NaCl Nyquist

curve (Figure 7.4) is consistent with the increased porosity compared to the pure H₂O film.

SEM and STEM-EDS studies showed that the anodic film formed on Mg polarized 0.5 h above E_b in 0.01 NaCl after 24 h aging at E_{corr} also contains a diffuse bilayer structure (Table 6.1). However, for the anodically polarized sample, the degree of porosity inside both Mg(OH)₂-rich middle-layer and MgO-rich inner-layer was observed to increase relative to the films formed at E_{corr} in pure H₂O and 0.01 M NaCl. This increase in porosity was more significant with the film formed inside the pit, in which macro pores were observed in the inner-layer film (Figure 5.35b). This substantial increased porosity, particularly inside of a pit, facilitates the faradic current flow through the observed physical short-cut paths (macro-sized pore filled with penetrating electrolyte) within the film. Therefore, the CPE_{film} and R_{por} values are expected to be negligible. Subsequently, the CPE_{film}/R_{por} frequency response is trivial and was not proposed by the anodic film structure model. Therefore, the Nyquist spectrum recorded for the sample held above E_b (Figure 7.3a) exhibits only one capacitive loop followed by an inductive loop in the low frequencies.

The EIS behaviour in 0.01 M NaCl was observed to consist of a low frequency inductive loop. As mentioned earlier, the inductor is usually interpreted as a relaxation phenomenon that occurs at the substrate/electrolyte interface and creates its impedance at low frequencies. Examples of this include: (i) multi-step dissolution/passivation of Fe in H₂SO₄ via (FeOH)_{ads} and (FeOH)⁺ species [136], [137], or (Fe(OH)²⁻)_{ads} [135], (ii) point defect model passivation of Al along with Cl⁻ attack to the passive film formed in Cl⁻

containing solutions [140], (iii) relaxation of the dielectric polarization of Al oxide film [139], (iv) or relaxation of the surface charge at the Al/film interface in Cl^- solutions [141].

Mechanisms proposed in the literature for the Mg inductive loops in $\text{Cl}^-/\text{SO}_4^{2-}$ containing solutions are multi-step dissolution of Mg via formation of an intermediate adsorbed Mg univalent cation [43], Mg^+ . This was hypothesised to induce the negative difference H_2 evolution through a subsequent chemical reaction between Mg^+ and H_2O at film free areas. Additionally, Song et al. [48] modified this model by considering coupled Mg_{ads}^+ intermediate species formation with variation in the surface film density/porosity due to a non-steady state dissolution of the film. Pebere et al. [45] also proposed a mechanism involving relaxation coverage of MgOH_{ads} intermediate species at the Mg/film interface. None of the above hypotheses regarding Mg anodic dissolution via consecutive electrochemical steps are verified with an analysis method to confirm the involved adsorbed species. Therefore, the nature of Mg low frequency inductive loops and their dependence on Mg anodic reaction is unresolved.

Erné and Vanmaekelbergh [144], [145] proposed a model to describe the origin of the inductive loops during the anodic dissolution of metals and semiconductors based on the transfer of ions through the interfacial double layer. This ion transfer was shown to drastically deform the double layer structure, and is therefore proposed to be the rate determining step for the total anodic dissolution reaction. This dissolution rate dependence was confirmed with a linear proportionality between the anodic current density and the characteristic frequency of the inductive loop.

Cl^- is reported to incorporate in film formed via formation of soluble hydroxy-chloride complex products [21], [39], [40], [41], [42], [51], [88]. The inductive behaviour is attributed to the anodic process and was reported to be independent of the cathodic current [45], [146]. The above observations postulate that the inductance could be a result of intermediate Mg-Cl products formed during the anodic dissolution of Mg in Cl⁻ solutions. A proposed mechanism was made for this hypothesis by Robinson et al. [39] considering the formation-dissolution of Mg-Cl soluble products at the film free areas of the Mg/electrolyte interface that results in an accelerated generation of Mg^{2+} cations. The presence of Cl in the Mg film formed in 0.01 NaCl proposes the formation of Mg-Cl compounds, however more accurate chemical surface analysis such as XPS is required in order to confirm this. Moreover, the inner MgO-rich layer was found to exhibit significant porosity, particularly within the pitted region film showing film free areas. These observations are consistent with the Robinson et al. [39] hypothesis regarding the formation-dissolution of Mg-Cl soluble products at the film free areas.

The film formed on Mg both adjacent to and inside a pit exhibited a diffuse bi-layer structure similar to pure H₂O film. However, the extent of the porosity and the size of pores within the outer Mg(OH)₂-rich layer were increased, particularly inside the pit. The MgO nano-crystals were found to be present in the outer Mg(OH)₂-rich layer and Cl incorporated within the whole film. Therefore, a similar mechanism to that proposed for the pure H₂O surface film, is postulated here for Mg film formation in 0.01 M NaCl, albeit accelerated due to the presence of Cl⁻.

The air-formed MgO film is expected to undergo a chemical hydration upon exposure to 0.01 M NaCl as is proposed for the film formed in H₂O. Since the starting pH of the 0.01 M NaCl was measured to be lower compared to pure H₂O and 1 M NaOH (Table 4.3), the extent of this chemical hydration is likely greater, as shown in the literature [21], [33], [78]. This likely exerts more stress-rupture damage to the barrier MgO-rich layer due to the hydration volume expansion. Additionally, Cl incorporation within the Mg(OH)₂ crystallographic structure increases the hydroxide solubility by forming hydroxy-chloride compounds [21], [41], [42], [51], [86], [87], [88]. Therefore, the outer Mg(OH)₂-rich layer exhibits greater degree of porosity along with a larger pore size. This enhances the ingress of Cl⁻ through the film after prolonged aging time [21], [41]. The presence of Cl⁻ at the substrate/electrolyte interface with a larger film free surface area intensifies the anodic dissolution of Mg [39], [40], as confirmed by the R_{ct} drop in 0.01 M NaCl versus pure H₂O. Furthermore, the presence of Fe-enriched impurity particles in the top layer of the pitting area, implies the micro-galvanic role of more noble elements in the pitting initiation and radial growth in Mg corrosion films [51].

7.3. 1 M NaOH vs. H₂O

Figure 7.5 shows the impedance spectrum of Mg recorded in 1 M NaOH after aging for 48 h. The Nyquist spectrum is specified with red diamonds in Figure 7.5a. It appears that high frequency loci of the curve consists of a capacitive loop, as well as a linear correlation between Z' versus -Z'' at lower frequencies with a slope of nearly 45°. Therefore, the low frequency behaviour is consistent with a Warburg impedance function and is likely representing a Warburg diffusion element. Note that the onset point of the

Nyquist curve recorded in 1 M NaOH is nearly zero compared to that of the H₂O and 0.01 M NaCl solutions. This point represents the conductivity of the test solution, and is consistent with high conductivity of 1 M NaOH, as shown in Table 4.2. The Bode plot of the real/imaginary experimental impedance magnitudes is also presented in Figure 7.5b. Since the Kramer-Kronig transforms is consistent with experimental results for the entire frequency, the system is stable, linear, and causal.

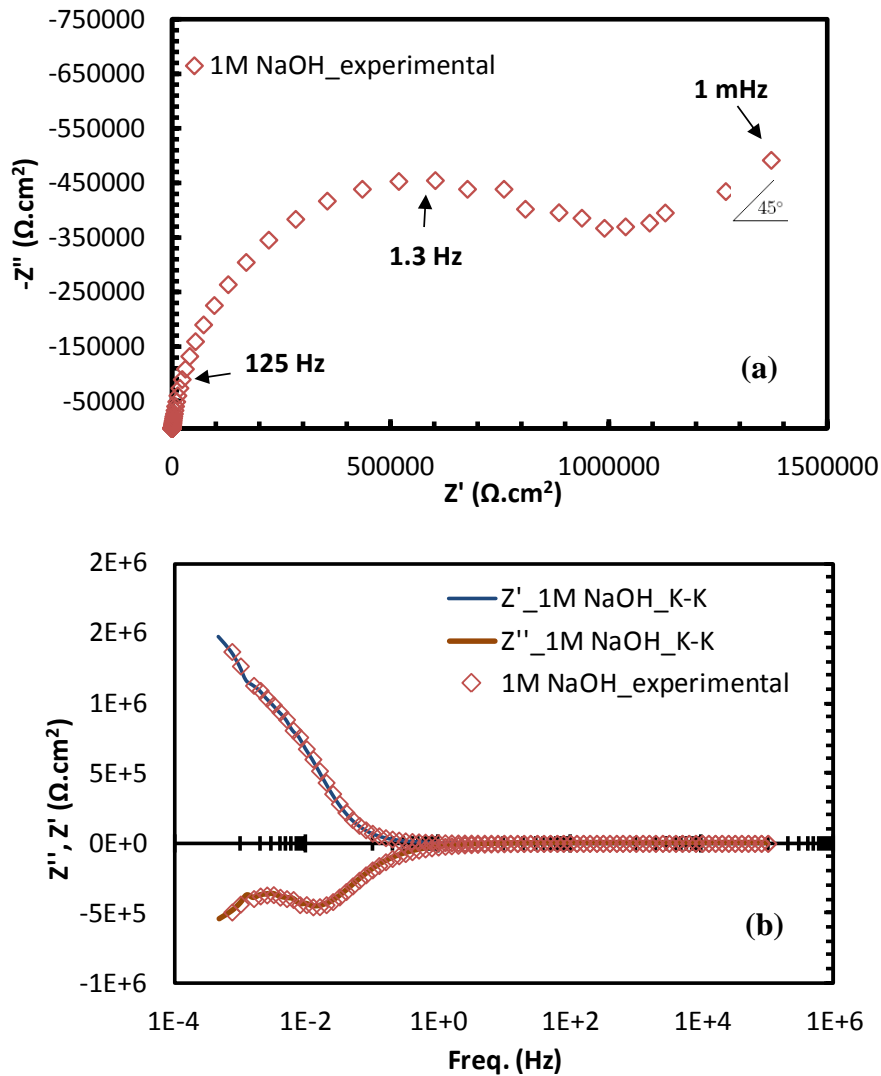


Figure 7.5: (a) Experimental Nyquist spectrum measured for Mg after 48 h aging in 1 M NaOH (b) Comparison of Kramer-Kronig transform with real and imaginary results.

The film formed in 1 M NaOH after 48 h aging at E_{corr} was found to exhibit a thin, compact MgO-rich single layer film decorated with random diffuse Mg(OH)₂-rich nodules. The Mg(OH)₂-rich nodules were observed to be less porous than those formed at E_{corr} in pure H₂O and 0.01 M NaCl. The R_{por} and R_{ct} values are therefore expected to be significantly increased. This can be observed as a considerable increase in the Nyquist spectrum size of the 1 M NaOH compared with respect to H₂O spectrum, as shown in Figure 7.6. Not that although the recorded Nyquist spectrum in 1 M NaOH (Figure 7.5a) indicates only one capacitive loop, the phase angle (ϕ) Bode diagram (Figure 7.7) confirms that this high frequency capacitive loop is composed of two distinct time constants, This is displayed by two dashed peak superimposed on the broadened high frequency capacitive time constant. They overlapped and appear as a single loop. The presence of two high and low frequency time constants is consistent with the proposed EIS Nyquist spectrum for aged Mg film in 1 M NaOH at E_{corr} , in the film structure model section (see Section 6.3).

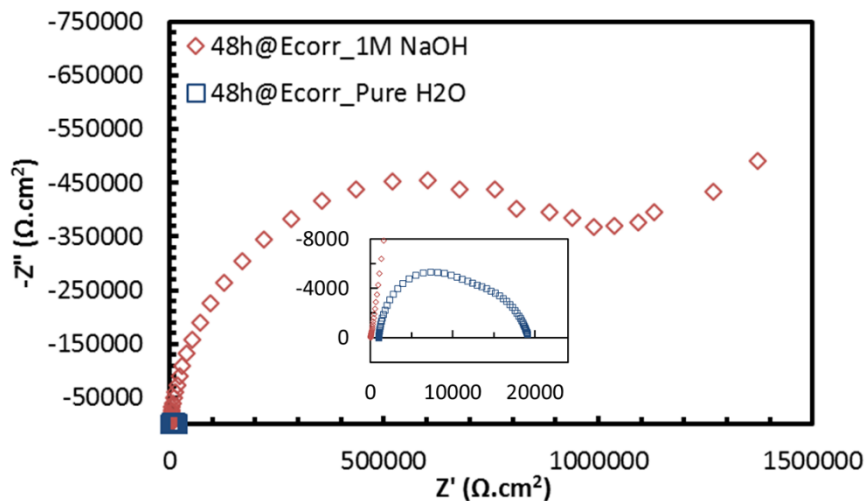


Figure 7.6: Comparison of Nyquist spectra recorded in 1 M NaOH versus pure H₂O after aging for 48 h at E_{corr} .

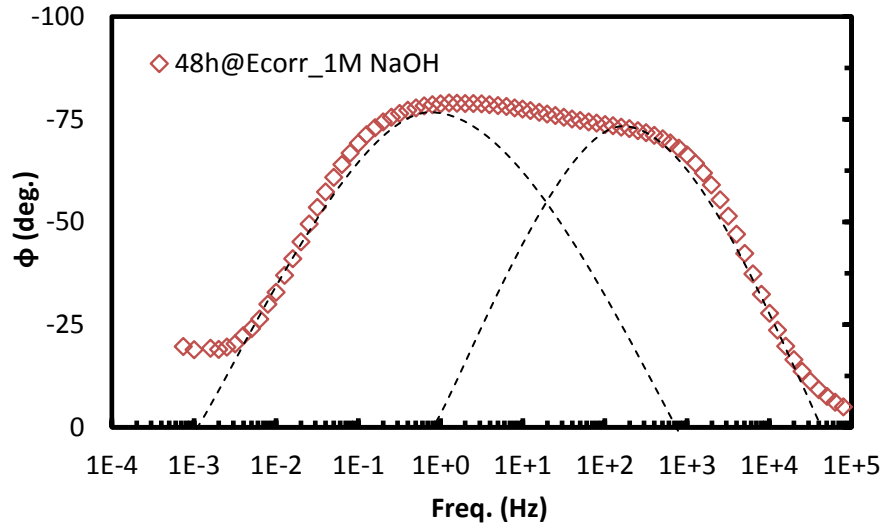


Figure 7.7: Phase angle – frequency Bode diagram recorded for Mg after 48 h aging in 1 M NaOH.

Another major difference between the Nyquist spectra recorded in 1 M NaOH and H₂O solutions is the presence of a Warburg impedance at low frequencies in the 1 M NaOH Nyquist curve. The anodic polarization curves recorded in 1 M NaOH and 1 M NaOH + 0.01 Na₂SO₄ test solutions after 24 h aging at E_{corr} were found to exhibit only an anodic limiting current density, i_L (Figure 5.13). The i_{corr} appeared to be nearly two order of magnitudes lower than that observed in near neutral solutions. This i_{corr} is likely mass transfer controlled based on the anodic polarization behaviour showing i_L . The presence of such low anodic i_L coupled with the formation of a relatively thinner and denser, less hydrated film with respect to near-neutral condition implies mass transfer controlled Mg dissolution through the film. This mass transfer within the film appears as the Warburg element at low frequencies (Figure 7.5a). Therefore, the presence of Warburg time

constant is consistent both with the compactness of the film and the i_L behaviour of the recorded polarization curves.

Qualitatively speaking, comparison of the impedance magnitudes of the Nyquist spectra measured for all test solutions (Figure 7.4 and Figure 7.6), indicates that the R_{por} in 1 M NaOH is significantly greater than H₂O and 0.01 M NaCl. Furthermore, the C_{film} formed in 1 M NaOH is lower compared to that formed in pure H₂O and 0.01 M NaCl. Similarly, the order of R_{ct} value is 1 M NaOH > pure H₂O > 0.01 M NaCl > 0.01 M NaCl (@E>E_b) and the order of C_{dl} exhibited an order of 0.01 M NaCl > pure H₂O > 1 M NaOH. The qualitative comparison of R_{ct} , R_{por} , C_{dl} , and C_{film} magnitudes in all environments agrees with the direct imaging observations that the film is more compact and protective in the 1 M NaOH electrolyte with a thicker and more stable MgO-rich barrier layer, whereas the extent of porosity increases in pure H₂O and 0.01 M NaCl accordingly. Moreover, the MgO-rich barrier layer was ascertained to be more damaged and thinner in pure H₂O and 0.01 M NaCl. Note that the larger size and extent of porosity is consistent with the destructive effect of Cl⁻. It is considered that this significant porosity facilitated the ingress of electrolyte via the film pores, and therefore R_{ct} was lowered, particularly in 0.01 M NaCl, which showed the maximum film damage at E>E_b.

The extent of the porosity observed in the thin partially-hydrated MgO layer appeared to be lower after exposure to 1 M NaOH than after exposure to pure H₂O. Moreover, the extent of coverage of the thicker outer Mg(OH)₂ layer was partial (nodules) when formed in 1 M NaOH and complete when formed in pure H₂O. Therefore,

it seems reasonable to suspect that a similar mechanism to that used to form the film in H₂O may be responsible for the formation of the Mg(OH)₂-rich nodules.

These differences can be explained by the corrosion mechanism proposed for the complete formation of a Mg(OH)₂-rich outer layer in pure H₂O. This involves a chemical breakdown (hydration) of the air-formed MgO film as a necessary precursor step [21]. A critical factor is the stress-rupture of the air-formed MgO film due to the increased molar volume of Mg(OH)₂ hydration product. The resultant porosity, coupled with the formation of a porous Mg(OH)₂ hydration product, allows the egress of Mg cations produced by the anodic dissolution of the bare substrate in direct contact with the electrolyte. Exceeding the solubility limit of Mg(OH)₂ in this region initiates the precipitation of a thick Mg(OH)₂-rich corrosion product on the inner layer. Lower porosity within the partially-hydrated MgO layer is expected in a more alkaline solution considering the reported slower hydration kinetics of bulk MgO in alkaline solutions [33], [78]. It is reasonable to expect that the slower hydration kinetics exhibited in more alkaline solutions would restrict hydration to the more favorable nucleation sites. Initiation of the hydration of the air-formed MgO thin films at higher energy defect sites, such as crystal interfaces (grain boundaries), among other factors has been reported by others previously [58], [80], [81]. The major evidence found in support of a hydration induced localized breakdown of the MgO-rich layer is the significant porosity that is observed underneath the nodules (Figure 5.51).

The chemical hydration film breakdown theory is consistent with the anodic dissolution current primarily flowing through the bare metal that is exposed directly to the

electrolyte within a hydration-induced, stress-ruptured region of the native MgO layer. Two factors are believed contribute to the reduced anodic kinetics exhibited by Mg when exposed to a strongly alkaline electrolyte, as demonstrated in Figure 5.10. One involves the formation of a denser outer $\text{Mg}(\text{OH})_2$ corrosion product precipitate in a strongly alkaline electrolyte, which would more effectively inhibit the egress of Mg cations from the bare substrate to the extreme surface of the outer $\text{Mg}(\text{OH})_2$ layer. This follows from reported observations of dense $\text{Mg}(\text{OH})_2$ precipitates being formed at high applied cathode potentials (strong local alkalization) during electrosynthesis [82], [83]. The other involves the surface area-normalized anodic dissolution current, which would be significantly reduced if only discrete locations existed where the air-formed MgO-rich film has hydrated to the extent that a stress-rupture has occurred rather than a continuous layer.

Diffusion controlled Mg dissolution through the surface film, is also considered in the proposed model. This hypothesis is consistent with the observation of an anodic limiting current density for the entire anodic potentiodynamic polarization test, as well as the Warburg impedance time constant recorded at very low frequencies of the EIS measurement.

8. CONCLUSIONS

The role of the film in aqueous corrosion of Mg was investigated by studying the composition and structure of the surface film coupled with electrochemical analysis of the corrosion kinetics. The composition and structure of the film formed on Mg exposed at the E_{corr} in pure H_2O at room temperature for 48 h was investigated using a FIB cross section and STEM-EDS. The results showed that the film was a bi-layer structure, consisting of a relatively thin (50-90 nm), more-porous, nano-crystalline, MgO rich inner layer and a much thicker (~700 nm), less-porous, $\text{Mg}(\text{OH})_2$ rich outer layer. The porous nature of the nano-crystalline MgO inner layer results from volume expansion associated with the hydration to $\text{Mg}(\text{OH})_2$.

The bi-layer surface film is likely a direct consequence from the combined exposure employed; initially to laboratory air, with ambient humidity during mechanical polishing and finally to pure H_2O during immersion. Initially, an air-formed nano-crystalline MgO film forms and the outer surface of which is covered by an extremely thin $\text{Mg}(\text{OH})_2$ layer, formed by the reaction of MgO with the H_2O vapour in the air. On exposure to pure H_2O , localized hydration of the inner MgO layer results in the formation of a porous nano-crystalline MgO rich inner layer. Anodic dissolution of the Mg substrate then occurs at the MgO-free surface regions, which ultimately leads to the precipitation of an $\text{Mg}(\text{OH})_2$ corrosion product.

The film formed on pure Mg after 24 h aging in 0.01 M NaCl solution for at E_{corr} was found to consist of a diffuse bilayer structure. This bi-layer structure was composed of a relatively thin and porous (50-100 nm) nano-crystalline MgO-rich inner layer and a

much thicker (~600 nm) and more porous Mg(OH)₂-rich outer layer. In addition, when Mg was polarized for 0.5 h at 0.1 V above E_b after 24 h aging in 0.01 M NaCl solution, both the outer layer Mg(OH)₂ rich layer (~450 nm) and MgO rich inner layer (~30 nm) appeared to be thinned. In contrast, the film inside a pit exhibited a thinner Mg(OH)₂ rich outer layer (~200-300 nm) buried under a top Mg(OH)₂ rich needle shape layer. Although the MgO-rich inner layer was found to have the same thickness as the MgO-rich inner-layer of the polarized condition (~30 nm), it appeared to be more damaged, in which larger surface areas of (about ~ 150 nm) the Mg substrate were film free.

The film formed by exposure to Cl⁻ solution was found to be significantly more porous compared to pure H₂O and 1 M NaOH corrosion films. This was attributed to the incorporation of Cl⁻ within the surface film by the formation of soluble hydroxy-chloride complex products. EDS analyses detected Cl within the entire film thickness in both E_{corr} immersion and anodically polarized conditions, however without significant enrichment in any one region. Moreover, presence of a higher extent of porosity along with macro pores confirmed an easier ingress of the Cl⁻-containing electrolyte via the film, which accelerates the anodic dissolution of Mg. The presence of Fe-enriched impurity particles in the top layer of the pitted region film is also consistent with the hypothesis of micro-galvanic effect of more noble particles in the pitting initiation and radial growth of breakdown in Mg corrosion film.

STEM-EDS analysis revealed that the film formed on Mg exposed to 1 M NaOH at the E_{corr} is comprised mainly of a relatively thin continuous crystalline MgO layer that has been hydrated to a variable degree; more so at the surface and less so within the bulk.

This layer is also decorated with a random distribution of significantly thicker $\text{Mg}(\text{OH})_2$ nodules, which reside on a more-porous region of the partially-hydrated MgO layer. The hydration of the native MgO surface film at discrete favorable sites leads to the development of internal mechanical stress due to the significant difference in the molar volume for MgO compared to the $\text{Mg}(\text{OH})_2$ hydration product. This leads to the stress rupture of the film and the subsequent formation of a $\text{Mg}(\text{OH})_2$ self-healing corrosion product nodule on the site of the stress-rupture. This process is repeated on an irregular basis and is characterized by significant potential drops as a function of exposure time.

Overall, the EIS results showed that the Mg corrosion resistance was lower in both aggressive $\text{Cl}^-/\text{SO}_4^{2-}$ and pure H_2O test solutions, whereas the corrosion resistance was highest in 1 M NaOH environment. However, the significant drops of the charge transfer resistance in 0.01 M NaCl test solution at $E > E_b$ indicated Mg exhibits considerably higher corrosion rates after pitting is initiated. Note that the charge transfer was slightly greater in pure H_2O under E_{corr} exposure compared to 0.01 M NaCl, which verifies relatively better corrosion resistance in a less aggressive electrolyte compared to environments including destructive ions such as Cl^- and SO_4^{2-} . This is consistent with observation of higher extent of porosity in the film formed by exposure to 0.01 M NaCl.

8.1. Future Research Opportunities

Although this study resulted into a combined improvement regarding the current knowledge of mechanistic corrosion behaviour and the structure and composition of films formed on Mg by exposure to different aqueous environments, further investigations are

required to consolidate the findings and improve the corrosion resistance of Mg and Mg alloys in the applicable media.

Throughout this study, it was found that hydration of the naturally formed oxide film on the surface of Mg in ambient atmospheres, is a precursor for corrosion of the substrate by exposure to aqueous solutions. Therefore, it is apparent that inhibition of this chemical hydration reaction could be a crucial step towards improving the corrosion resistance of Mg by creating a stable MgO layer to the exposed corrosive environment. Similar attention could be drawn to study the stable Mg(OH)₂-rich film formed on top of chemically hydrated MgO-rich inner layer within nodules.

Several hypothesis have been proposed regarding the mechanistic analysis of the low frequency inductive loops observed during the anodic dissolution of Mg in aggressive environments compromised of destructive anions such as Cl⁻ and SO₄²⁻. However, this phenomenon is yet to be resolved to identify the plausible adsorbed surface species that are suggested to control Mg anodic dissolution. A comprehensive knowledge of Mg anodic dissolution reactions in such media will be beneficial in order to seek the appropriate prevention methods to improve the corrosion resistance.

Micro-galvanic corrosion of Mg with enriched nobler impurity particles such as Fe is suggested as a precursor to Mg pitting initiation and radial growth in aggressive aqueous solutions. Focused research to rationalize this observation is required to elucidate the mechanism of the pitting initiation.

Mg is reported to exhibit dissimilar corrosion resistance on different crystallographic orientations in aqueous solutions. Understanding the differences between

the composition and structure of these films formed on distinct crystallographic planes requires further investigation. Therefore, a combined STEM-EDS study with mechanistic analysis of the surface films formed on different Mg single crystals is another appealing research topic to understand Mg corrosion resistance. This could reduce the corrosion rate and/or produce Mg(OH)₂ corrosion films with improved protection for polycrystalline Mg.

8. REFERENCES

- [1] H. E. Friedrich and B. L. Mordike, *Magnesium Technology Metallurgy, Design Data, Applications*. New York: Springer, 2006.
- [2] G. L. Makar and J. Kruger, "Corrosion of magnesium," *International Materials Reviews*, vol. 38, no. 3, pp. 138 – 153, 1993.
- [3] G. Song and A. Atrens, "Understanding Magnesium Corrosion—A Framework for Improved Alloy Performance," *Advanced Engineering Materials*, vol. 5, no. 12, pp. 837–858, Dec. 2003.
- [4] E. Ghali, W. Dietzel, and K. U. Kainer, "General and Localized Corrosion of Magnesium Alloys: A Critical Review," *Journal of Materials Engineering and Performance*, vol. 13, no. 1, pp. 7–23, Feb. 2004.
- [5] S. J. Splinter, N. S. McIntyre, and T. Do, "Influence of low level iron impurities on the initial interaction of water vapour with polycrystalline magnesium surfaces," *Surface Science*, vol. 317, pp. 194–202, 1994.
- [6] S. J. Splinter, "Influence of Ar⁺ ion bombardment on the initial interaction of water vapour with polycrystalline magnesium surfaces," *Surface Science*, vol. 302, pp. 93–108, 1994.
- [7] J. H. Nordlien, K. Nianciou, S. Ono, and N. Masuko, "Morphology and Structure of Oxide Films Formed on MgAl Alloys by Exposure to Air and Water," *Journal of the Electrochemical Society*, vol. 143, no. 8, pp. 2564–2572, 1996.
- [8] J. H. Nordlien and K. Nisancioglu, "Morphology and Structure of Water-Formed Oxides on Ternary MgAl Alloys," *Journal of the Electrochemical Society*, vol. 144, no. 2, pp. 461–466, 1997.
- [9] S. Feliu Jr, M. C. Merino, R. Arrabal, A. E. Coy, and E. Matykina, "XPS study of the effect of aluminium on the atmospheric corrosion of the AZ31 magnesium alloy," *Surface and Interface Analysis*, vol. 41, no. 3, pp. 143–150, Mar. 2009.
- [10] S. Feliu, a. Pardo, M. C. Merino, A. E. Coy, F. Viejo, and R. Arrabal, "Correlation between the surface chemistry and the atmospheric corrosion of AZ31, AZ80 and AZ91D magnesium alloys," *Applied Surface Science*, vol. 255, no. 7, pp. 4102–4108, Jan. 2009.

- [11] M. G. Fontana, *Corrosion Engineering*. McGraw-Hill Book Company, 1985, p. 556.
- [12] E. E. Stansbury and R. M. Condra, *Fundamentals of Electrochemical Corrosion*. ASM International, 2000.
- [13] D. A. Jones, *Principles and Prevention of Corrosion*. Macmillan Pub Co, 1991, p. 568.
- [14] G. L. Song and A. Atrens, "Corrosion Mechanisms of Magnesium Alloys," *Advanced Engineering Materials*, vol. 1, no. 1, pp. 11–33, 1999.
- [15] E. Ghali, W. Dietzel, and K. U. Kainer, "Testing of General and Localized Corrosion of Magnesium Alloys: A Critical Review," *Journal of Materials Engineering and Performance*, vol. 13, no. 5, pp. 517–529, Oct. 2004.
- [16] m, J.-E. Svensson, and L.-G. Johansson, "The Influence of Carbon Dioxide on the Atmospheric Corrosion of Some Magnesium Alloys in the Presence of NaCl," *Journal of The Electrochemical Society*, vol. 149, no. 4, p. B103, 2002.
- [17] N. LeBozec, M. Jönsson, and D. Thierry, "Atmospheric Corrosion of Magnesium Alloys: Influence of Temperature, Relative Humidity, and Chloride Deposition," *Corrosion*, vol. 60, no. 4, pp. 356–361, Apr. 2004.
- [18] J. C. Fuggle, L. M. Watson, D. J. Fabian, and S. Affrossman, "X-ray photoelectron studies of the reaction of clean metals (Mg, Al, Cr, Mn) with oxygen and water vapour," *Surface Science*, vol. 49, no. 1, pp. 61–76, Apr. 1975.
- [19] S. J. Splinter, N. S. McIntyre, W. N. Lennard, K. Griffiths, and G. Palumbo, "An AES and XPS study of the initial oxidation of polycrystalline magnesium with water vapour at room temperature," *Surface Science*, vol. 292, no. 1–2, pp. 130–144, Jul. 1993.
- [20] K. Asami and S. Ono, "Quantitative X-Ray Photoelectron Spectroscopy Characterization of Magnesium Oxidized in Air," *Journal of The Electrochemical Society*, vol. 147, no. 4, p. 1408, Apr. 2000.
- [21] H. B. Yao, Y. Li, and A. T. S. Wee, "An XPS investigation of the oxidation/corrosion of melt-spun Mg," *Applied Surface Science*, vol. 158, pp. 112–119, 2000.
- [22] C. Fotea, J. Callaway, and M. R. Alexander, "Characterisation of the surface chemistry of magnesium exposed to the ambient atmosphere," *Surface and Interface Analysis*, vol. 38, no. 10, pp. 1363–1371, Oct. 2006.

- [23] M. Liu, S. Zanna, H. Ardelean, I. Frateur, P. Schmutz, G. Song, A. Atrens, and P. Marcus, "A first quantitative XPS study of the surface films formed, by exposure to water, on Mg and on the Mg–Al intermetallics: Al_3Mg_2 and $\text{Mg}_{17}\text{Al}_{12}$," *Corrosion Science*, vol. 51, no. 5, pp. 1115–1127, May 2009.
- [24] J. H. Nordlien, S. Ono, N. Masuko, and K. Nisancioglu, "A TEM investigation of naturally formed oxide films on pure magnesium," *Corrosion Science*, vol. 39, no. 8, pp. 1397–1414, Aug. 1997.
- [25] V. Fournier, P. Marcus, and I. Olefjord, "Oxidation of magnesium," *Surface and Interface Analysis*, vol. 34, no. 1, pp. 494–497, Aug. 2002.
- [26] W. A. Fernando, "Review of Corrosion and Corrosion Control of Magnesium Alloys and Composites," *Journal of Materials Engineering*, vol. 11, no. 4, pp. 299–313, 1989.
- [27] G. Song, "Recent Progress in Corrosion and Protection of Magnesium Alloys," *Advanced Engineering Materials*, vol. 7, no. 7, pp. 563–586, Jul. 2005.
- [28] G. Song and A. Atrens, "Recent Insights into the Mechanism of Magnesium Corrosion and Research Suggestions," *Advanced Engineering Materials*, vol. 9, no. 3, pp. 177–183, Mar. 2007.
- [29] R. Zeng, J. Zhang, W. Huang, W. Dietzel, K. U. Kainer, C. Blawert, and W. Ke, "Review of studies on corrosion of magnesium alloys," *Transactions of Nonferrous Metals Society of China*, vol. 16, pp. s763–s771, Jun. 2006.
- [30] Pourbaix, *Atlas of Electrochemical Equilibria in Aqueous Solutions*. Natl Assn of Corrosion, 1974, p. 644.
- [31] M. Santamaria, F. Di Quarto, S. Zanna, and P. Marcus, "Initial surface film on magnesium metal: A characterization by X-ray photoelectron spectroscopy (XPS) and photocurrent spectroscopy (PCS)," *Electrochimica Acta*, vol. 53, no. 3, pp. 1314–1324, Dec. 2007.
- [32] A. Seyeux, M. Liu, P. Schmutz, G. Song, A. Atrens, and P. Marcus, "ToF-SIMS depth profile of the surface film on pure magnesium formed by immersion in pure water and the identification of magnesium hydride," *Corrosion Science*, vol. 51, no. 9, pp. 1883–1886, Sep. 2009.
- [33] D. A. Vermilyea and C. F. Kirk, "Studies of Inhibition of Magnesium Corrosion," *Journal of The Electrochemical Society*, vol. 116, no. 11, p. 1487, 1969.

- [34] E. Gulbrandsen, J. Taftø, and A. Olsen, "The passive behaviour of Mg in alkaline fluoride solutions. Electrochemical and electron microscopical investigations," *Corrosion Science*, vol. 34, no. 9, pp. 1423–1440, Sep. 1993.
- [35] W. A. Badawy, N. H. Hilal, M. El-Rabiee, and H. Nady, "Electrochemical behavior of Mg and some Mg alloys in aqueous solutions of different pH," *Electrochimica Acta*, vol. 55, no. 6, pp. 1880–1887, Feb. 2010.
- [36] P. F. King, "Magnesium as a Passive Metal," *Journal of The Electrochemical Society*, vol. 110, no. 11, p. 1113, Nov. 1963.
- [37] Z. Cai, D. Lu, W. Li, Y. Liang, and H. Zhou, "Study on anodic oxidation of magnesium in 6M KOH solution by alternative current impedance," *International Journal of Hydrogen Energy*, vol. 34, no. 1, pp. 467–472, Jan. 2009.
- [38] L. Desgranges, G. Calvarin, and G. Chevrier, "Interlayer interactions in $M(OH)_2$: a neutron diffraction study of $Mg(OH)_2$," *Acta Crystallographica Section B Structural Science*, vol. 52, no. 1, pp. 82–86, Feb. 1996.
- [39] J. L. Robinson and P. F. King, "Electrochemical Behavior of the Magnesium Anode," *Journal of The Electrochemical Society*, vol. 108, no. 1, p. 36, Jan. 1961.
- [40] H. A. Robinson, "No Title," *Trans. Electrochem. Soc.*, vol. 96, p. 499, 1946.
- [41] R. L. Brossard and D. L. Piron, "Le comportement électrochimique du magnésium en milieux légèrement alcalins," *Canadian Journal of Chemistry*, vol. 58, no. 1, pp. 30–38, Jan. 1980.
- [42] J. Światowska, P. Volovitch, and K. Ogle, "The anodic dissolution of Mg in NaCl and Na_2SO_4 electrolytes by atomic emission spectroelectrochemistry," *Corrosion Science*, vol. 52, no. 7, pp. 2372–2378, Jul. 2010.
- [43] _____, B. Tribollet, and V. Vivier, "An Impedance Investigation of the Mechanism of Pure Magnesium Corrosion in Sodium Sulfate Solutions," *Journal of The Electrochemical Society*, vol. 154, no. 2, p. C108, 2007.
- [44] G. Baril and N. Pébère, "The corrosion of pure magnesium in aerated and deaerated sodium sulphate solutions," *Corrosion Science*, vol. 43, no. 3, pp. 471–484, Mar. 2001.
- [45] N. Pebere, "investigation Of Magnesium Corrosion In Aerated Sodium Sulfate Solution By Electrochemical Impedance Spectroscopy," *Electrochimica Acta*, vol. 35, no. 2, pp. 555–561, 1990.

- [46] G. Song, A. Atrens, D. S. T. John, and J. Nairn, "The Anodic Dissolution Of Magnesium And Sulphate Solutions In Chloride," *Corrosion Science*, vol. 39, no. 1, pp. 1981–2004, 1997.
- [47] L. Song, "The electrochemical corrosion of pure Mg in 1 N NaCl," *Corrosion Science*, vol. 39, no. 5, pp. 855–875, 1997.
- [48] G.-L. Song and Z. Xu, "Crystal orientation and electrochemical corrosion of polycrystalline Mg," *Corrosion Science*, vol. 63, pp. 100–112, Oct. 2012.
- [49] G. L. Makar and J. Kruger, "Corrosion Studies of Rapidly Solidified Magnesium Alloys," *Journal of the Electrochemical Society*, vol. 137, no. 2, pp. 414–421, 1990.
- [50] S. Feliu, C. Maffiotte, A. Samaniego, J. C. Galván, and V. Barranco, "Effect of naturally formed oxide films and other variables in the early stages of Mg-alloy corrosion in NaCl solution," *Electrochimica Acta*, vol. 56, no. 12, pp. 4554–4565, Apr. 2011.
- [51] G. Williams and H. Neil McMurray, "Localized Corrosion of Magnesium in Chloride-Containing Electrolyte Studied by a Scanning Vibrating Electrode Technique," *Journal of The Electrochemical Society*, vol. 155, no. 7, p. C340, 2008.
- [52] M. Kurth, P. C. J. Graat, H. D. Carstanjen, and E. J. Mittemeijer, "The initial oxidation of magnesium: an in situ study with XPS, HERDA and ellipsometry," *Surface and Interface Analysis*, vol. 38, pp. 931–940, 2006.
- [53] M. Kurth, P. C. J. Graat, and E. J. Mittemeijer, "The oxidation kinetics of magnesium at low temperatures and low oxygen partial pressures," *Thin Solid Films*, vol. 500, no. 1–2, pp. 61–69, Apr. 2006.
- [54] E. Panda, L. P. H. Jeurgens, and E. J. Mittemeijer, "The initial oxidation of Al–Mg alloys: Depth-resolved quantitative analysis by angle-resolved x-ray photoelectron spectroscopy and real-time in situ ellipsometry," *Journal of Applied Physics*, vol. 106, no. 11, p. 114913, Dec. 2009.
- [55] N. Cabrera and N. F. Mott, "Theory of the oxidation of metals," *Reports on Progress in Physics*, vol. 12, no. 1, pp. 163–184, Jan. 1949.
- [56] R. Lindström, L.-G. Johansson, G. E. Thompson, P. Skeldon, and J.-E. Svensson, "Corrosion of magnesium in humid air," *Corrosion Science*, vol. 46, no. 5, pp. 1141–1158, May 2004.

- [57] J. H. Lee, J. H. Eun, S. G. Kim, S. Y. Park, M. J. Lee, and H. J. Kim, "Hydration behavior of MgO single crystals and thin films," *Journal of Materials Research*, vol. 18, no. 12, pp. 2895–2903, Dec. 2003.
- [58] J. H. Lee, J. H. Eun, S. Y. Park, S. G. Kim, and H. J. Kim, "Hydration of r.f. magnetron sputtered MgO thin films for a protective layer in AC plasma display panel," *Thin Solid Films*, vol. 435, no. 1–2, pp. 95–101, Jul. 2003.
- [59] M. J. Stirniman, C. Huang, R. S. Smith, S. A. Joyce, and B. D. Kay, "The adsorption and desorption of water on single crystal MgO (100): The role of surface defects," *J. Chem. Phys.*, vol. 105, no. 3, pp. 1295–1298, 1996.
- [60] J. A. Schultz, M. H. Mintz, T. R. Schuler, and J. W. Rabalais, "TOF spectra of direct recoils," *Surface Science*, vol. 146, no. 2–3, pp. 438–456, Nov. 1984.
- [61] X. D. Peng and M. A. Barteau, "Characterization of oxide layers on Mg(0001) and comparison of H₂O adsorption on surface and bulk oxides," *Surface Science*, vol. 233, no. 3, pp. 283–292, Jul. 1990.
- [62] H. P. Godard and etc., *Corrosion of Light Metals*. John Wiley & Sons Inc, 1967, p. 372.
- [63] G. Song, A. Atrens, and X. Wu, "Corrosion behaviour of az10\ az490 and az80 in sodium chloride," *Corrosion Science*, vol. 40, no. 10, pp. 658–680, 1998.
- [64] G. G. Perrault, "The Potential-ph Diagram Of The Magnesium-water System," *Electroanalytical Chemistry and Interracial Electrochemistry*, vol. 51, pp. 107–119, 1974.
- [65] G. G. Perrault, "Potentiostatic Study Of The Magnesium Electrode," *Electroanalytical Chemistry and Interracial Electrochemistry*, vol. 27, pp. 47–58, 1970.
- [66] E. Gulbrandsen, "Anodic behaviour of Mg in HCO₃–3CO₂–3 buffer solutions. Quasi steady measurements.pdf." Elsevier Ltd, pp. 1403–1412, 1992.
- [67] J. Chen, J. Dong, J. Wang, E. Han, and W. Ke, "Effect of magnesium hydride on the corrosion behavior of an AZ91 magnesium alloy in sodium chloride solution," *Corrosion Science*, vol. 50, no. 12, pp. 3610–3614, Dec. 2008.
- [68] J. Chen, J. Wang, E. Han, J. Dong, and W. Ke, "States and transport of hydrogen in the corrosion process of an AZ91 magnesium alloy in aqueous solution," *Corrosion Science*, vol. 50, no. 5, pp. 1292–1305, May 2008.

- [69] A. Y. Simaranov, T. I. Sokolova, A. I. Marshakov, And Y. N. Mikhailovskii, "corrosion-electrochemical Behavior Of Magnesium In Acidic Media, Containing Oxidants ," *Protection of metals*, vol. 27, no. 3, pp. 329–334.
- [70] H. Inoue, K. Sugahara, A. Yamamoto, and H. Tsubakino, "Corrosion rate of magnesium and its alloys in buffered chloride solutions," *Corrosion Science*, vol. 44, pp. 603–610, 2002.
- [71] G. G. Perrault, *Encyclopaedia of electrochemistry of the elements, Vol. VIII*. Marcel Dekker, 1978, pp. 263–319.
- [72] R. Tunold, H. Holtan, M. B. Hagg Berge, and A. Lasson, "No Title," *Corrosion Science*, vol. 17, p. 353, 1977.
- [73] G. L. Makar, J. Kruger, and A. Joshi, "No Title," in *Proceedings Annual Meeting of the Minerals, Metals and Materials Society Advances in Magnesium Alloys and Composites*, 1988, pp. 105–121.
- [74] S. Bender, J. Goellner, A. Heyn, and S. Schmigalla, "A new theory for the negative difference effect in magnesium corrosion," *Materials and Corrosion*, p. n/a–n/a, Aug. 2011.
- [75] P. Volovitch, M. Serdechnova, and K. Ogle, "Aqueous Corrosion of Mg-Al Binary Alloys: Roles of Al and Mg," Jun. 2012.
- [76] P. . Bradford, B. Case, G. Dearnaley, J. . Turner, and I. . Woolsey, "Ion beam analysis of corrosion films on a high magnesium alloy (Mgno Al 80)," *Corrosion Science*, vol. 16, no. 10, pp. 747–766, Jan. 1976.
- [77] D. A. Vermilyea, "The Dissolution of MgO and Mg(OH)₂ in Aqueous Solutions," *Journal of The Electrochemical Society*, vol. 116, no. 9, p. 1179, Sep. 1969.
- [78] O. Fruhwirth, G. W. Herzog, I. Hollerer, and A. Rachetti, "Dissolution and hydration kinetics of MgO," *Surface Technology*, vol. 24, no. 3, pp. 301–317, Mar. 1985.
- [79] J. A. Mejias, A. J. Berry, K. Refson, and D. G. Fraser, "The kinetics and mechanism of MgO dissolution," *Chemical Physics Letters*, vol. 314, no. 5–6, pp. 558–563, Dec. 1999.
- [80] M. O. Aboelfotoh, K. C. Park, and W. A. Pliskin, "Infrared and high-energy electron diffraction analyses of electron-beam-evaporated MgO films," *Journal of Applied Physics*, vol. 48, no. 7, p. 2910, Jul. 1977.

- [81] J. H. Lee, J. H. Eun, S. G. Kim, S. Y. Park, M. J. Lee, and H. J. Kim, "Hydration behavior of MgO single crystals and thin films," *Journal of Materials Research*, vol. 18, no. 12, pp. 2895–2903, Jan. 2003.
- [82] C.-F. Li, W.-H. Ho, and S.-K. Yen, "Effects of Applied Voltage on Morphology and Crystal Orientation of Mg(OH)₂ Coating on Pt by Electrochemical Synthesis," *Journal of The Electrochemical Society*, vol. 156, no. 2, p. E29, Feb. 2009.
- [83] Y. Lv, Z. Zhang, Y. Lai, J. Li, and Y. Liu, "Formation mechanism for planes (011) and (001) oriented Mg(OH)₂ films electrodeposited on SnO₂ coating glass," *CrystEngComm*, vol. 13, no. 11, p. 3848, 2011.
- [84] S. Kim and M. Okido, "The Electrochemical Properties and Mechanism of Formation of Anodic Oxide Films on Mg-Al Alloys," vol. 24, no. 8, pp. 975–980, 2003.
- [85] Y. Mizutani, S. J. Kim, R. Ichino, and M. Okido, "Anodizing of Mg alloys in alkaline solutions," *Surface and Coatings Technology*, vol. 169–170, no. null, pp. 143–146, Jun. 2003.
- [86] W. Feitknecht and M. Gerber, "No Title," *Helv. Chim. Acta*, vol. 26, no. 131, p. 555, 1946.
- [87] W. Feitknecht and F. Held, "No Title," *ibid.*, vol. 27, p. 1480, 1944.
- [88] J. Brun, C.H.; Pagetti, J.; Talbot, "Study of the corrosion of magnesium in aqueous 3 wt.% sodium chloride solution at room temperature," *Memoires Scientifiques de la Revue de Metallurgie*, vol. 73, no. 10, pp. 659–668, 1976.
- [89] F. El-Taib Heakal, a. M. Fekry, and M. Z. Fatayerji, "Influence of halides on the dissolution and passivation behavior of AZ91D magnesium alloy in aqueous solutions," *Electrochimica Acta*, vol. 54, no. 5, pp. 1545–1557, Feb. 2009.
- [90] R. Ambat, N. N. Aung, and W. Zhou, "Studies on the influence of chloride ion and pH on the corrosion and electrochemical behaviour of AZ91D magnesium alloy," *Journal of Applied Electrochemistry*, vol. 30, pp. 865–874, 2000.
- [91] Y. Song, D. Shan, R. Chen, and E.-H. Han, "Corrosion characterization of Mg–8Li alloy in NaCl solution," *Corrosion Science*, vol. 51, no. 5, pp. 1087–1094, May 2009.

- [92] M. E. Stroumanis, B. K. Bhatia, and M. E. Straumanis, "Disintegration of Magnesium While Dissolving Anodically in Neutral and Acidic Solutions," *Journal of the Electrochemical Society*, vol. 110, no. 5, pp. 357–360, May 1963.
- [93] M. E. Orazem and B. Tribollet, *Electrochemical Impedance Spectroscopy*. Hoboken: John Wiley & Sons, Inc, 2008.
- [94] W. Plieth, *Electrochemistry for Materials Science*. Elsevier Ltd, 2008.
- [95] W. J. Lorenz and F. MANSEELD, "Determination OF Crrosion Rates by Electrochemical DC and AC Methods," *Corrosion Science*, vol. 21, no. 9, pp. 647–672, 1981.
- [96] N. Birks, G. H. Meier, and F. S. Pettit, *INTRODUCTION TO THE HIGH-TEMPERATURE OXIDATION OF METALS*, 2nd ed. Cambridge University Press, 2006.
- [97] C. Cao, "on The Impedance Plane Displays For Irreversible Electrode Reactions Based On The Stability Conditions Of The Steady-state-ii. Two State Variables Besides Electrode Potential," *Electrochimica Acta*, Vol. 35, No. 5, Pp. 837–844, 1990.
- [98] C. Cao, "on The Impedance Plane Displays For Irreversible Electrode Reactions Based On The Stability Conditions Of The Steady-state-i. State Variable Besides Electrode Potential," *Electrochimica Acta*, vol. 35, no. 5, pp. 831–836, 1990.
- [99] *Standard Practice for Microetching Metals and Alloys*, E407–07e1 ed. Philadelphia, PA: The American Society for Testing and Materials: Annual Book of ASTM Standards, 2012.
- [100] G. Vander Voort, "Metallography of Magnesium and its Alloys," *Buehler Tech-Notes*, vol. 4, no. 2.
- [101] *Standard Test Methods for Determining Average Grain Size*, E112–10th ed. Philadelphia, PA: The American Society for Testing and Materials: Annual Book of ASTM Standards, 2012.
- [102] E. McCafferty, "Validation of corrosion rates measured by the Tafel extrapolation method," *Corrosion Science*, vol. 47, no. 12, pp. 3202–3215, Dec. 2005.
- [103] B. A. Boukamp, "Practical application of the Kramers-Kronig transformation on impedance measurements in solid state electrochemistry," *Solid State Ionics*, vol. 62, no. ii, pp. 131–141, 1993.

- [104] D. D. Macdonald, "review Of Mechanistic Analysis By Electrochemical Impedance Spectroscopy," *Electrochimica Acta*, vol. 35, no. 10, pp. 1509–1525, 1990.
- [105] S. . Cashion, N. . Ricketts, and P. . Hayes, "The mechanism of protection of molten magnesium by cover gas mixtures containing sulphur hexafluoride," *Journal of Light Metals*, vol. 2, no. 1, pp. 43–47, Feb. 2002.
- [106] A. Mirak, C. J. Davidson, and J. A. Taylor, "Characterisation of fresh surface oxidation films formed on pure molten magnesium in different atmospheres," *Corrosion Science*, vol. 52, no. 6, pp. 1992–2000, Jun. 2010.
- [107] S. XIONG and X. WANG, "Protection behavior of fluorine-containing cover gases on molten magnesium alloys," *Transactions of Nonferrous Metals Society of China*, vol. 20, no. 7, pp. 1228–1234, Jul. 2010.
- [108] T. E. K Aarstad, G Tranell, G Pettersen, "Various techniques to study the surface of magnesium protected by SF₆," *Magnesium Technology*, pp. 5–10, 2003.
- [109] S. F. Jr., J. C. Galván, A. Pardo, M. C. Merino, and R. Arrabal, "Native Air-Formed Oxide Film and its Effect on Magnesium Alloys," *The Open Corrosion Journal*, 2010. .
- [110] D. B. Williams and C. B. Carter, *Transmission Electron Microscopy: A Textbook for Materials Science*. Springer, 2009, pp. 371–388.
- [111] V. G. Tsirelson, A. S. Avilov, Y. A. Abramov, E. L. Belokoneva, R. Kitaneh, and D. Feil, "X-ray and Electron Diffraction Study of MgO," *Acta Crystallographica Section B Structural Science*, vol. 54, no. 1, pp. 8–17, Feb. 1998.
- [112] J. W. Edington, *Practical Electron Microscopy in Materials Science*. Techbooks, 1991, p. 356.
- [113] P. W. Hawkes and J. C. H. Spence, *Introduction Science of Microscopy*. New York: Springer Science + Business Media Inc., 2007.
- [114] H. E. S. and E. Tatge, "No Title," *Natl. Bureau Stand.*, vol. 539, p. 1, 1953.
- [115] A. Pavese, M. Catti, G. Ferraris, and S. Hull, "P-V equation of state of portlandite, Ca(OH)₂, from powder neutron diffraction data," *Physics and Chemistry of Minerals*, vol. 24, no. 2, pp. 85–89, Feb. 1997.

- [116] M. Liu, D. Qiu, M.-C. Zhao, G. Song, and A. Atrens, "The effect of crystallographic orientation on the active corrosion of pure magnesium," *Scripta Materialia*, vol. 58, no. 5, pp. 421–424, Mar. 2008.
- [117] C. W. B. M. S.A. Flodström, "Initial oxidation of the Mg(0001) surface, an electron spectroscopy study," *Surface Science*, vol. 118, no. 3, pp. 513–522, 1982.
- [118] P. A. Thiry, "Incipient oxidation of Magnesium a HREELS and Photoemission study," *Physical Review B*, vol. 39, no. 6, p. 3620, 1989.
- [119] J. M. G. H. Namba, J. Darville, "A model for the oxidation of Mg (0001) based upon LEED, AES, ELS and work function measurements," *Surface Science*, vol. 108, pp. 446–482, 1981.
- [120] V. S. Birchal, S. D. F. Rocha, M. B. Mansur, and V. S. T. Ciminelli, "A simplified mechanistic analysis of the hydration of magnesia," *The Canadian Journal of Chemical Engineering*, vol. 79, no. 4, pp. 507–511, Aug. 2001.
- [121] S. A. Holt, C. F. Jones, G. S. Watson, A. Crossley, C. Johnston, C. J. Sofield, and S. Myhra, "Surface modification of MgO substrates from aqueous exposure: an atomic force microscopy study," *Thin Solid Films*, vol. 292, no. 1–2, pp. 96–102, Jan. 1997.
- [122] Y. Kuroda, E. Yasugi, H. Aoi, K. Miura, and T. Morimoto, "Interaction of water with the surface of magnesium oxide," *Journal of the Chemical Society, Faraday Transactions 1*, vol. 84, no. 7, p. 2421, 1988.
- [123] A. J. Bard and M. V. Mirkin, *Scanning Electrochemical Microscope*. Marcel Dekker, Inc., 2001.
- [124] G. Williams, H. N. McMurray, and R. Grace, "Inhibition of magnesium localised corrosion in chloride containing electrolyte," *Electrochimica Acta*, vol. 55, no. 27, pp. 7824–7833, Nov. 2010.
- [125] K. M. Ismail and S. Virtanen, "Electrochemical Behavior of Magnesium Alloy AZ31 in 0.5 M KOH Solution," *Electrochemical and Solid-State Letters*, vol. 10, no. 3, p. C9, 2007.
- [126] J. Hitzig, K. JUTTNER, and W. J. Lorenz, "AC-impedance measurements on porous aluminium oxide films," *Corrosion Science*, vol. 24, no. 1, pp. 945–952, 1984.

- [127] J. Hitzig, K. Ji, and W. J. Lorenz, "AC-Impedance Measurements on Corroded Porous Aluminum Oxide Films," *Journal of The Electrochemical Society*, vol. 133, no. 5, pp. 887–890, 1986.
- [128] T. P. Hoar and G. C. Wood, "THE SEALING OF POROUS ANODIC OXIDE FILMS ON ALUMINIUM," *Electrochimica Acta*, vol. 7, pp. 333–353, 1962.
- [129] J.-P. Dasquet, D. Caillard, E. Conforto, J.-P. Bonino, and R. Bes, "Investigation of the anodic oxide layer on 1050 and 2024T3 aluminium alloys by electron microscopy and electrochemical impedance spectroscopy," *Thin Solid Films*, vol. 371, no. 1–2, pp. 183–190, Aug. 2000.
- [130] V. Moutarlier, M. P. Gigandet, B. Normand, and J. Pagetti, "EIS characterisation of anodic films formed on 2024 aluminium alloy, in sulphuric acid containing molybdate or permanganate species," *Corrosion Science*, vol. 47, no. 4, pp. 937–951, Apr. 2005.
- [131] S. Feliu, C. Maffiotte, J. C. Galván, and V. Barranco, "Atmospheric corrosion of magnesium alloys AZ31 and AZ61 under continuous condensation conditions," *Corrosion Science*, vol. 53, no. 5, pp. 1865–1872, May 2011.
- [132] M. Stern and A. L. Geaby, "Electrochemical Polarization," *Journal of The Electrochemical Society*, vol. 104, no. 1, p. 56, Jan. 1957.
- [133] F. T. Ulaby, *Fundamentals of Applied Electromagnetics (5th Edition)*. Prentice Hall, 2006, p. 448.
- [134] I. Epelboin, C. Gadielli, and M. Keddam, "A MODEL OF THE ANODIC BEHAVIOUR IN SULPHURIC ACID MEDIUM OF IRON," *Electrochimica Acta*, vol. 20, pp. 913–916, 1974.
- [135] B. BECHET, L. EPELBOIN, and M. Keddam, "New Data From Impedance Measurements Concerning The Anodic Dissolution Of Iron In Acidic Sulphuric Media" *Journal of electroanalytical Chemistry*, vol. 76, pp. 129–134, 1977.
- [136] I. Epelboin and M. Keddam, "Faradaic Impedances: Diffusion Impedance and Reaction Impedance," *Journal of the Electrochemical Society*, vol. 117, pp. 1052–1056, 1971.
- [137] I. Epelboin, M. Ksouri, and R. Wiart, "Intermediaires Adsorbes et Electrocrystallisation," *Journal of Applied Physics*, vol. 65, pp. 373–389, 1975.

- [138] L. M. Baugh, "Corrosion and polarization characteristics of zinc in neutral—acid media — I. Pure zinc in solutions of various sodium salts," *Electrochimica Acta*, vol. 24, no. 6, pp. 657–667, Jun. 1979.
- [139] M. J. Dignam and P. J. Ryan, "High field kinetic processes in anodic oxide films on aluminium. II. Current transients for constant field conditions," *Canadian Journal of Chemistry*, vol. 46, no. 4, pp. 549–556, Feb. 1968.
- [140] J. B. Bessone, D. R. SALINAS, and W. J. Lorenzt, "An EIS Study Of Aluminium Barrier-type Films Formed In Different Media Oxide," *Electrochimica Acta*, vol. 37, no. 12, pp. 2283–2290, 1992.
- [141] H. J. De Wit, C. Wijenberg, and C. Crevecoeur, "Impedance Measurements during Anodization of Aluminum," *Journal of The Electrochemical Society*, vol. 126, no. 5, p. 779, 1979.
- [142] D. D. Macdonald, S. Real, S. I. Smedley, M. Urquidi-macdonald, S. R. I. International, and M. Park, "Evaluation of Alloy Anodes for Aluminum-Air Batteries IV. Electrochemical Impedance Analysis of Pure Aluminum in 4M KOH at 25C," *Journal of The Electrochemical Society*, vol. 135, no. 10, pp. 2410–2414, 1988.
- [143] G. Stanford, *Transformation Calculus and Electrical Transients*. Prentice Hall, 1955.
- [144] D. Vanmaekelbergh, "Coupled Partial Ion-Transfer Steps in the Anodic Dissolution of Metals," *Journal of The Electrochemical Society*, vol. 146, no. 7, p. 2488, 1999.
- [145] B. H. Ern  and D. Vanmaekelberg, "The Low-Frequency Impedance of Anodically Dissolving Semiconductor and Metal Electrodes," *Journal of The Electrochemical Society*, vol. 144, no. 10, pp. 3385–3392, 1997.
- [146] M. Taheri and J. R. Kish, "Effectiveness of a Galvanostatic Cathodic Polarization Pre-Treatment on Improving the Corrosion Resistance of Mg to Aqueous Saline Solutions," in *ICMAA2012*, 2012.
- [147] M. Taheri, R. C. Phillips, J. R. Kish, and G. a. Botton, "Analysis of the surface film formed on Mg by exposure to water using a FIB cross-section and STEM-EDS," *Corrosion Science*, vol. 59, pp. 222–228, Jun. 2012.